Millimeter-Wave Communications: Physical Channel Models, Design Considerations, Antenna Constructions and Link-Budget

Ibrahim A. Hemadeh, *Member, IEEE,* Katla Satyanarayana, *Student Member, IEEE,* Mohammed El-Hajjar, *Senior Member, IEEE,* and Lajos Hanzo, *Fellow, IEEE*

Abstract—The millimeter wave (mmWave) frequency band spanning from 30 GHz to 300 GHz constitutes a substantial portion of the unused frequency spectrum, which is an important resource for future wireless communication systems in order to fulfill the escalating capacity demand. Given the improvements in integrated components and enhanced power efficiency at high frequencies, wireless systems can operate in the mmWave frequency band. In this paper, we present a survey of the mmWave propagation characteristics, channel modeling and design guidelines, such as system and antenna design considerations for mmWave, including the link budget of the network, which are essential for mmWave communication systems. We commence by introducing the main channel propagation characteristics of mmWaves followed by channel modeling and design guidelines. Then, we report on the main measurement and modeling campaigns conducted in order to understand the mmWave band's properties and present the associated channel models. We survey the different channel models focusing on the channel models available for the 28 GHz, 38 GHz, 60 GHz and 73 GHz frequency bands. Finally, we present the mmWave channel model and its challenges in the context of mmWave communication systems design.

Index Terms—Millimeter-wave, mmWave, radio frequency, 5G, wideband channel, MIMO, channel estimation, channel model, spatial channel model, power delay profile, ultra-wideband, propagation, wireless propagation, multipath fading, human blockage, diffraction, multipath, parameter estimation, 2D channel, 3D channel, space-time shift keying, Spatial Modulation, PSK, QAM.

NOMENCLATURE

3GPP	3rd Generation Partnership Project
ABF	Analog Beamforming
ADC	Analog-to-Digital Converter
AE	Antenna Element
AoA	Angle-of-Arrival
AoD	Angle-of-Departure
AF	Array Factor
AWGN	Additive White Gaussian Noise
BB	Baseband
BER	Bit Error Rate

BF	Beamforming
BLAST	Bell-Labs Layered Space-Time
CMOS	Complementary Metal–Oxide–Semiconductor
D2D	Device-to-Device
DAC	Digital-to-Analog Converter
DBF	Digital Beamforming
DEE	Distance Extension Exponent
ETSI	European Telecommunications Standards Institute
FSL	Free-Space Loss
GSFIM	Generalized Space-Frequency Index Modulation
HetNet	Heterogeneous Network
ISG	Industry Specification Group
LMDS	Local Multipoint Distribution Service
LMG	Layered Multi-Group
LNA	Low Noise Amplifiers
LOS	Line-of-Sight
MBER	Minimum Bit Error Ratio
METIS	Mobile and wireless communications Enablers for the Twenty-twenty Information Society
MF	Multi-Functional
MIMO	Multiple-Input Multiple-Output
MiWEBA	Millimetre-Wave Evolution for Back-haul and Access
MMB	Mobile Broadband
mmWave	Millimeter Wave
MPC	Multipath Component
MU	Multi-User
NLOS	Non-Line-of-Sight
O2i	Outdoor-to-Indoor
OFDM	Orthogonal Frequency-Division Multiplexing
PA	Power Amplifier
PDF	Probability Density Function
PDP	Power Delay Profile
PL	Path-Loss
PLE	Path-Loss Exponent
PTP	Point-to-Point
QAM	Quadrature Amplitude Modulation
QoS	Quality of Service
RT	Ray-Tracing
Rx	Receiver
SCM	Spatial Channel Model

SNR	Signal-to-Noise Ratio
SV	Saleh-Valenzuela
TG3c	The Task Group 3c
TGad	The Task Group ad
ToA	Time-of-Arrival
TSV	Triple-Saleh-Valenzuela
Tx	Transmitter
UMa	Urban Macro
UMi	Urban Micro
UWB	Ultra-Wideband
V2V	Vehicular-to-Vehicular
WLAN	Wireless Local Area Network
WPAN	Wireless Personal Area Network
XPD	Cross-Polarization Discrimination

I. INTRODUCTION

In this paper, we provide a review of the propagation characteristics of mmWave signals and a comprehensive survey of the mmWave channel models found in the literature. Recent studies show that the next decade will encounter a 1000-fold increase in capacity demand [1], [2] and the microwave band where most wireless technologies operate cannot support this capacity demand. Various data traffic reports forecast an impending capacity crisis, for example in [3] it is reported that the global mobile data traffic has grown 4,000-fold over the past decade and nearly 400-million fold over the past 15 years. CISCO added in [3] that the monthly global mobile data traffic in 2021 is expected to grow to 30.6 ExaBytes, which is more than five times the monthly traffic in 2016 and eight times that of 2015. Additionally, Ericsson in [4] reported that by the end of the year 2020 more than nine billion mobile subscriptions and 7.7 billion mobile broadband subscriptions will be using the existing 2G, 3G and 4G mobile technologies. This capacity demand triggered both academic [5]–[8] and industrial [9]–[12] efforts to find new methods of overcoming it.

Figure 1 shows the three main methods used for enhancing the system capacity, where shrinking the cell-area and applying advanced signal processing techniques can further enhance the spectral efficiency, however not by orders of magnitudes [13]. Another potential solution is to allocate new frequency spectrum [7], [14], [15], such as that in the millimeter-wave (mmWave) frequency band. Furthermore, as shown in Figure 1, combining the three techniques would enormously increase the capacity [16], given that the technology at the new frequency band is available and can be practically implemented. Given the huge available bandwidths at the mmWave band, reduced cell sizes and enhanced signal processing techniques, the capacity demand for the next decade or so can indeed be fulfilled.

A. Introducing The mmWave Band

The frequency band between 30 GHz and 300 GHz is termed as the mmWave spectrum, since it has the wavelengths range spanning from 1mm to 10mm [17]. Anecdotally speaking for a moment, in Figure 2, we present a stylized road-map illustration of the whole mmWave technology by relying on roundabouts, their entrances and exits, avenues and highways. Each roundabout represents a collaborative environment, where each of its entrances' names signifies their influence on the roundabout, while each of the exits' names symbolizes a single contribution of the roundabout. For example, the "Scenario Selection" roundabout in Figure 2 has four entrances, which resemble the types of scenarios considered for mmWave channel modeling, such as the indoor and outdoor avenues. Furthermore, the size of a roundabout denotes its importance, which is determined by the number of entrances and exits, and hence the "mmWave Technology" roundabout is the biggest. The main roundabout is the "mmWave Technology" roundabout, where its main contributors are the channel modeling, hardware advancements, signal processing and standardization, which are shown as wide highways rather than ordinary avenues. The advertisement signs shown around the "mmWave Technology" roundabout resemble the advantages of the mmWave technology, while the only city shown represents one of the main research foci at mmWaves, namely the "Next Generation Communications Systems". Furthermore, we explicitly detail in Figure 2 the "Channel Modeling" roundabout, its entrances and exits, which is the main contribution of this survey, where each of the roundabout's entrance constitutes a notable aspect of the modeling efforts, such as the "Channel Measurements", "Frequency Selection", "Modeling Method", "Scenario Selection", "Characteristics" and "Environment" roundabouts associated with the "Channel Modeling" roundabout. The mmWave spectrum has already been employed for many applications, such as for example radio astronomy [18], radars [19], military [20], [21], satellite communications [22], [23] and point-to-point (PTP) communication applications [6], [24]–[26], but not for commercial wireless networks. Recently, however it has been used for short range communications [9], [11], [14], [27], mobile broadband networks [6], [15] and PTP networks [28]–[30].

B. Enabling Technologies for mmWaves

According to Moore's law, the number of transistors per chip doubles every two years [1], which results in a factor 32 times reduction each decade for baseband digital algorithms processing [31]. Similarly, the Analogue-to-Digital Converter (ADC) power consumption was reduced by an order of magnitude over the last decade [32]. Fortunately, the consumption factor[1] formulated by Murdock and Rappaport in [33] of mmWave systems describing the ratio of data rate to power consumption increases as the bandwidth increases, which means that the power efficiency of on-chip components, such as Power Amplifiers (PA), Low Noise Amplifiers (LNA), ADCs, Digital-to-Analogue Converters (DACs) and mixers increases as we move to the large-bandwidth mmWave frequency bands. Furthermore, the recent advances in low-cost and low-power Complementary Metal–Oxide–Semiconductor

---

[1] The consumption factor is denoted by the achievable data rate per power consumed for a communication link.
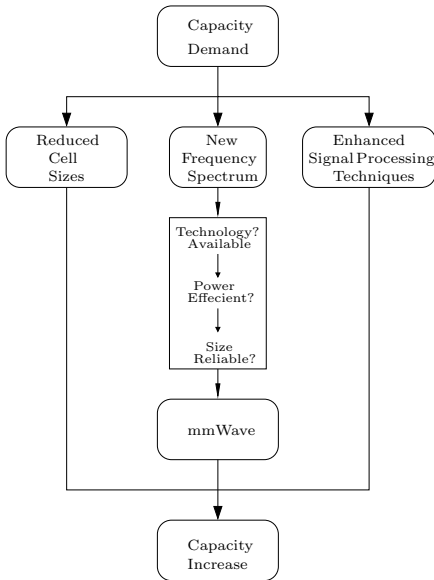
Figure 1. The three main techniques to boost system capacity, reduced cell size, enhanced signal processing techniques and finding new frequency bandwidths, can be combined in order to provide enormous capacity increase.

(CMOS) designed for high-frequency communications [34]–[36], in addition to the short mmWaves wavelengths that implies smaller effective antennas apertures, all paved the way toward scaling wireless systems up in frequency to the mmWave band both for indoor [9], [14], [27] and outdoor communication systems [6], [15], [37]–[39], as part of the hardware advances shown in Figure 2.

Several studies mmWave reported multi-Gbps communication links, such as [10], [11], [25], [38], [40]–[43]. However, wireless communications at mmWaves is restricted by the propagation characteristics, which are inherently different from those of the band below 5 GHz, where most of today's wireless systems communicate over the benign channel having the most favored propagation characteristics counter. The path-loss and shadowing effects, as well as various attenuation losses of the mmWave channel become more hostile as the frequency increases. However, most of these disadvantages associated with the increased carrier frequency can be mitigated by sophisticated processing techniques, such as high-gain directional antenna arrays associated with narrow beams, such as beamforming (BF) techniques [7], [44]–[46], in addition to diverse other classic Multiple-Input Multiple-Output (MIMO) solutions [47]–[49]. However, the channel should be first innately understood and modeled for the sake of developing such techniques. Hence, as shown in Figure 2, the channel modeling is a major contributor to the mmWave technology.

In the past three decades, various measurement campaigns have been launched for the sake of acquiring an in-depth knowledge of the spatial and temporal characteristics of Figure 2 of the mmWave frequency bands in order to develop new techniques and methods to operate over them; namely those in the 30 GHz band [50], 40 GHz band [51], 50 GHz band [52], 60 GHz band [28], [29], [53]–[55], 93 GHz band [56] and more recently in the 28 GHz band [57]–[61], 38 GHz band

[39], [62], [63] and 72 GHz band [64]. The main research emphasis was characterizing the mmWave channel in the sub-100 GHz domain of mmWaves, while the band above 100 GHz has not gained so much attention until recently. However, Cheng *et al.* have lately reported [65] on an extensive measurement campaign both in the 110-170 GHz band and in the 300 GHz bands as well as in the 30 GHz band. Due to the lack of measurements at the above 100 GHz frequency band, we show an "under construction" sign at the "> 100 GHz" entrance to the 'Frequency Selection roundabout' of Figure 2. Owing to the massive effort invested in these campaigns, the research community has developed various channel models, each fitting a specific communication scenario. For instance, most of the early modeling efforts were carried in the 60 GHz band due to its wide unlicensed spectral resources for indoor wireless systems, such as in [66]–[70]. However, the lack of measurements and the understanding of other mmWave bands restricted the number of available channel models until lately, where the interest in the 60 GHz band flourished with a view to invoke it for the emerging 5G system [71], [72], for short range networks [54] and for broadband mobile networks [73], [74] as well as in the 28 GHz, 38 GHz and 72 GHz bands for the same applications [6], [12], [15], [75].

Initially, a narrowband statistical channel model was proposed in [7] for mobile networks, which could be invoked for the 28 GHz band, 38 GHz band as well as for the 73 GHz frequency band. However, after obtaining sufficient measurements, many wideband channel models have been proposed for these bands [55], [76]–[80] as it will be shown later in this treatise.

With the shorter wavelengths of higher frequencies comes the ability of stacking more antennas at both the transmitter and the receiver within a smaller area than those operating in the sub-5 GHz frequency band, hence facilitating the employment of different MIMO techniques, such as multiplexing, diversity and beamforming arrangements [81], [82], but with specific design considerations. For instance, BF is considered to be a key enabling technique for communications in the mmWave band [6], [15], [83], for the sake of combating the associated high path-loss [43]. BF is generally achieved by directing the transmitted signal towards the receiver, while suppressing it in the direction of the unintended receivers, which can be applied using digital, analogue, or combined digital and analogue beamforming techniques [84]. Digital beamforming (DBF) relies on pre-processing the transmitted signal in the digital domain and then post-processing the received signal at the receiver [85]. However, digital beamforming is impractical at high frequencies, since each antenna would require its own analogue RF front-end chain, which adds extra cost, whilst resulting in a bulkier transceiver and higher power consumption [13], [43]. However, Abbas *et al.* has recently proposed in [86] a fully digital receiver by relying on a variable-resolution ADC. On the other hand, analogue beamforming (ABF) is applied with the aid of a pair of a digitally controlled phase shifter and power amplifier dedicated for each Antenna Element (AE) at both transceiver ends, and it is considered to be costly-effective at high frequencies. Hence, analogue beamforming would best fit mmWave communica-
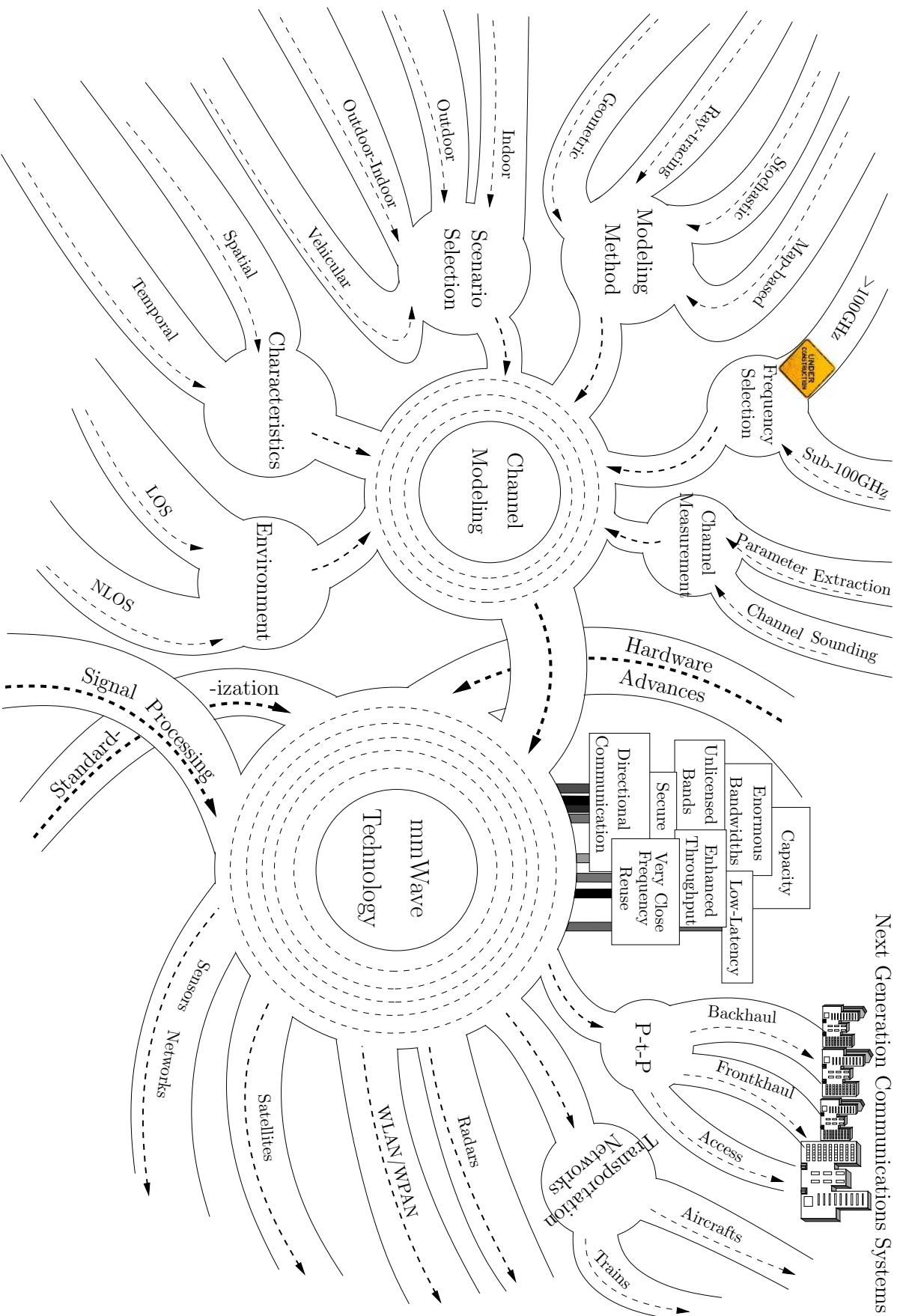
Figure 2. A road-map illustration of the mmWave technology. Each roundabout represents a collaborative environment, where each of its entrances' names signifies their influence on the roundabout, while each of the exits' names symbolizes a single contribution of the roundabout. Furthermore, the size of a roundabout denotes its importance, which is determined by the number of entrances and exits. The main roundabout is the "mmWave Technology" roundabout, where its main contributors are the channel modeling, hardware advancements, signal processing and standardization, which are shown as wide highways rather than ordinary avenues. The main focus of this treatise is on the channel modeling part, manifested by the "Channel Modeling" roundabout, its entrances and exits. The advertisement signs shown around the "mmWave Technology" roundabout resemble the advantages of the mmWave technology, while the only city shown expresses one of the main research focus at mmWaves, namely the "Next Generation Communications Systems".

tions [87]–[89]. However, the advantage of ABF comes at the cost of handling only a single input data stream, which limits the signal processing and multiplexing capability of the system [43], [83], thus mmWave wireless systems can be further enhanced by relying on hybrid analogue-digital techniques, as proposed in [8], [13], [48], [90], [91]. Hybrid techniques empower digitally processing multiple data streams before being transmitted by the antenna arrays employed [49], [92]. With aid of antenna arrays, beamforming gains that are required to compensate the propagation losses are derived and steered in the desired direction by an array of phase shifters.

C. Outline

The aim of this survey paper can be summarized as follows:

- Introduce the main propagation characteristics of mmWaves;
- Survey both the main propagation characteristics of mmWaves and the available channel models in the literature;
- Design guidelines including link budget analysis of the network;

The rest of this paper is organized as follows. First we present the propagation characteristics of the mmWave channel in Section II. Then, we provide a comprehensive survey of the major channel modeling efforts available in the literature in Section III. Next, we present both the steps towards building the channel model as well as our design guidelines for mmWaves transceivers in Section IV. Finally, we conclude in Section V. The skeleton structure of the paper is shown in Figure 3.

Notations: Bold upper case letters represent matrices; $\lfloor . \rfloor$ denotes the flooring of a real number to the nearest smallest following integer, while $\lfloor . \rceil$ denotes the rounding operation of a real number to the nearest integer; $mod(.)$ indicates the modulus operation; $\binom{n}{r}$ denotes the combinations without repetition of n objects taken r at a time; $()^T$ represents the transpose operation and $(.)^H$ represents the Hermitian transpose operation; $\mathbb{C}^{a \times b}$ indicates a matrix of complex numbers of the size $a \times b$; $\|.\|$ denotes the Frobenius norm and $|.|$ indicates the modulus of a complex number; The $\circledast$ operator denotes the circular convolution operation.

II. MILLIMETER-WAVE PROPAGATION CHARACTERISTICS

The availability of wide unlicensed, semi-licensed and licensed bandwidth in the mmWave frequency band spurred a great interest in academia [7], [8], [46], [93], in the industry [10], [37], [38], [71] and in the standardization bodies [10], [11], [14], [27] as part of the quest for substantial capacity gains. However, the propagation characteristics of mmWave frequencies are different from the classical sub-3GHz band, hence requiring further efforts for modeling the mmWave channel [46], [67]. The channel characteristics of indoor, outdoor, cellular, fronthaul and backhaul systems have to be carefully be modeled in order to develop future mmWave communication systems associated with one of the "Scenario
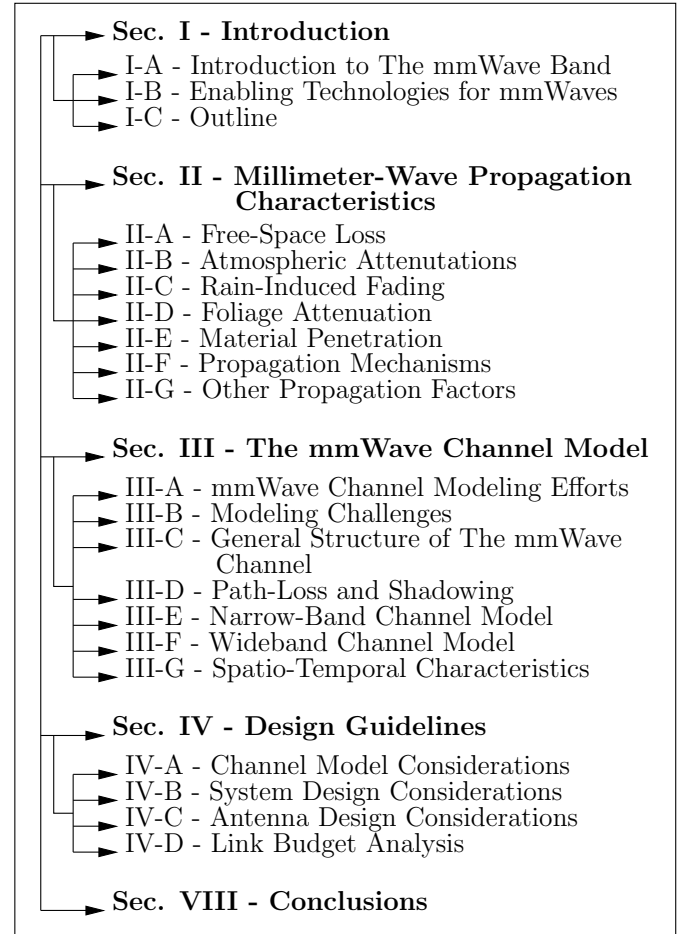
Figure 3. Skeleton structure of this treatise.

Selection" roundabout of Figure 2. Extensive measurement campaigns were carried out to understand the physical characteristics of the mmWave band. Table I shows the major measurements campaigns carried out in the last three decades in the different mmWave frequency bands, such as the 28 GHz, 30 GHz , 40 GHz, 50 GHz, 60 GHz, 70 GHz, 80 GHz and 90 GHz GHz bands. These measurements mainly covers the path-loss, the spatial and angular characteristics, temporal characteristics, rays-propagation mechanisms, material penetration and the effects of rain, snow and other attenuation losses. These campaigns typically opt for arbitrary indoor or outdoor locations, with sufficiently separated transmitter (Tx) and receiver (Rx) locations of an order of magnitude higher distance than the wavelength λ for estimating the channel parameters. These measurements are essential for modeling the mmWave channel at each of its frequency bands.

Furthermore, the radio wave propagation characteristics differs from one frequency band to another. Compared to signals at lower frequencies, mmWaves are more vulnerable both to atmospheric effects and to human shadowing and cannot propagate well through most materials [15], [94]. Thus, these effects cannot be neglected in the modeling process. This section reviews the major propagation characteristics of mmWaves shown in Figure 4, including the free path-
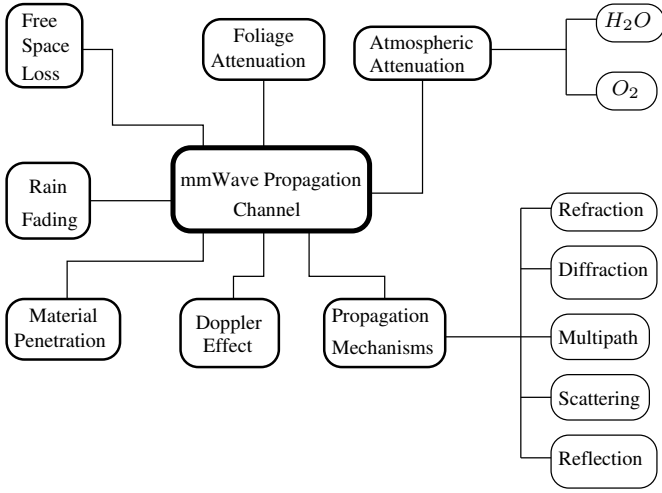
Figure 4. mmWave propagation characteristics.

loss, the hydrometeor events' attenuations, and propagation mechanisms.

Figure 5. Received power at mmWave frequencies, when P_t=10 dBm and the antenna gain is 10 dBi.

A. Free-Space Loss

The free-space loss (FSL) shown in Figure 4 is defined by the loss in the transmitted signals strength in free space. The FSL between two communicating isotropic antennas[2] separated by a distance d in kilometers (km) and operating at a frequency f in GHz is given by [129]:

$$FSL_{[dB]} = 92.4 + 20\log f_{[GHz]} + 20\log d_{[km]}. \quad (1)$$

According to (1), the FSL is proportional to both the separation distance and the carrier frequency. This translates into a high FSL as the carrier frequency enters the mmWave frequency band, when compared to the sub-3 GHz band. The received power over the sub-100 GHz mmWave band at three different distances is illustrated in Figure 5. Furthermore, the FSL obtained at the 28 GHz, 40 GHz, 60 GHz, 100 GHz, 200 GHz and 300 GHz frequencies is depicted in Figure 6, where it shows that an additional loss of 24 dB, 27 dB and 32 dB added in the 28 GHz, 38 GHz and 73 GHz bands compared to the 1.8 GHz GSM band at any given separation distance [6], [7], [38]. Moreover, in indoor communication systems the FSL at 60 GHz is, respectively. 28 dB and 22 dB higher than the 2.4 GHz and 5 GHz bands currently utilized for indoor WiFi networks.

Let us now consider an isotropic transmit antenna and isotropic receive antenna as shown in Figure 7 (a). The power received by the power P_r received by the receiver given a transmit power P_t at a distance d is given by [131]:

$$\frac{P_r}{P_t} = \frac{\text{Area of receive antenna}}{\text{Area of sphere}} = \frac{A_d}{4\pi d^2}, \quad (2)$$

[2]Isotropic antennas are idealised antennas with uniform radiation patterns in all directions.
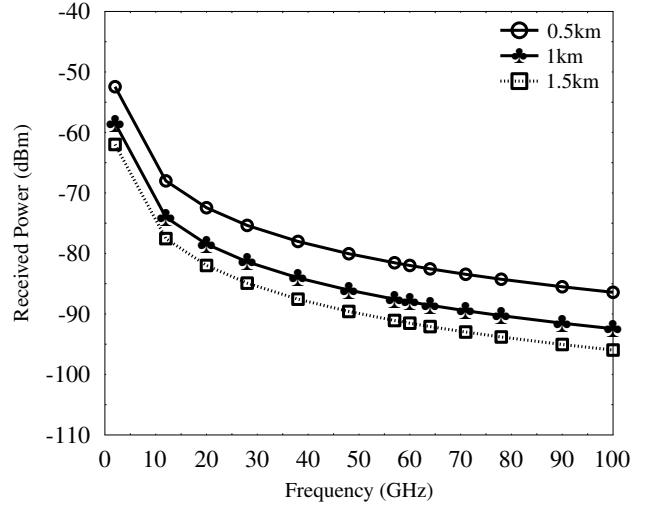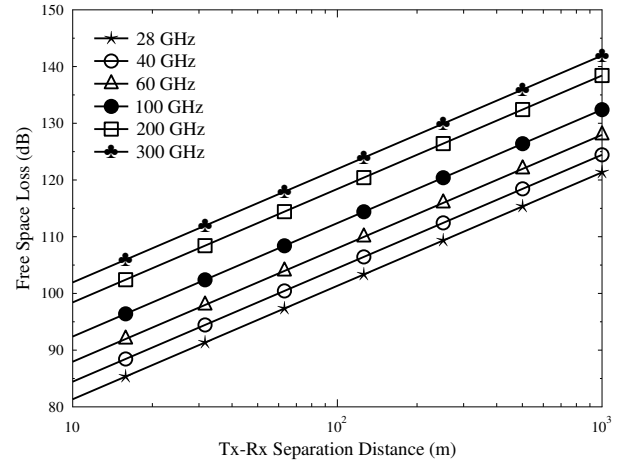

Figure 6. Free space loss at mmWave frequencies [130]

where A_d is the aperture area or effective area of an antenna, oriented perpendicular to the direction of an incoming radio wave, which would intercept the same amount of power (from that wave) as is available at the terminals of the antenna. For an antenna having a gain G, the aperture area is given by [132]:

$$A_d = G\frac{\lambda^2}{4\pi}, \quad (3)$$

where λ is the wavelength.

Antennas with a higher aperture area have a higher gain and they can receive the arriving signal more efficiently and it also radiates the signal in the desired directions with a higher efficiency [132]. It can be seen from (3) that the aperture of an

Paper(s)	Year	f	Description
[50], [53], [95]–[97] [57]–[61] [55], [77], [78], [98], [99] [100]–[104] [72], [76], [79], [80], [105], [106]	1988-2017	28 GHz	Path loss, angular and delay spreads, AoA, AoD, shadowing for Line-of-Sight (LOS) and Non-LOS (NLOS) scenarios, foliage and diffraction wideband measurements.
[50]	1988	30 GHz	Propagation mechanisms including reflection, LOS, NLOS and penetration losses measurements.
[107], [108]	2004-2005	35 GHz	Two-way ground reflection and foliage attenuation measurements.
[28], [62], [63], [109] [29], [39], [98], [110]	2000-2015	38 GHz	Outdoor RF propagation measurements, e.g. Path loss, multipath, delay spread, AoA and propagation mechanisms (diffraction, scattering, reflection).
[51], [111], [112]	2008	40 GHz	Material penetration losses, propagation mechanisms. [111] in particular reports wideband measurements for the 37.2 GHz and 20 GHz bands.
[113]	2000	41.5 GHz	Wideband measurements with 2 GHz bandwidth.
[52]	1992	50 GHz	Path loss and penetration measurements at 50 GHz.
[28], [29], [50], [53], [114] [115]–[118] [119]–[122] [44], [123]–[125] [126]	1988-2011	60 GHz	Indoor and outdoor measurements of various channel characteristics, such as time dispersion, angular spreads, AoA, AoD, penetration losses, propagation mechanisms, path loss, shadowing and attenuation.
[64], [77], [104] [78], [99], [103], [127]	2013-2017	73 GHz	Sounding and penetration loss for indoor scenarios.
[128]	2010	71-76 GHz	Outdoor hydrometeors attenuation measurements.
[56]	2009	93 GHz	Hydrometeors attenuation measurements at 38 GHz, 58 GHz and 93 GHz for links between high altitude platforms and Earth base-station.
[65]	2017	30 GHz	Path loss measurements at the 26.5 GHz to 40 GHz,110
		140 GHz	GHz to 170 GHz, and 300 GHz to 316 GHz bands are
		300 GHz	carried in an indoor scenario and LOS environment.

Table I

MAJOR MEASUREMENT CAMPAIGNS IN DIFFERENT MMWAVE FREQUENCY BANDS, WHERE IT IS SEEN THAT THE MAIN CONTRIBUTIONS ARE IN THE SUB-100 GHZ BAND, AS SHOWN BY THE "FREQUENCY SELECTION" ROUNDABOUT ENTRANCES OF FIGURE 2.

antenna depends on the wavelength, where higher frequencies have smaller antenna aperture area (for a given gain).

Substituting $G = 1$ for an isotropic antenna into (3), and applying it in (2), we get,

$$\frac{P_r}{P_t} = \left(\frac{\lambda}{4\pi d}\right)^2, \tag{4}$$

which is known as Friis' law of free space propagation loss [131]. Then, let us consider a directional transmit antenna with a gain G_t and aperture (effective) area A_{eff}^t as shown in Figure 7(b), then the power P_r received at a distance d by a receive antenna with (effective) aperture area A_{eff}^r is given by:

$$\frac{P_r}{P_t} = G_t \frac{A_{\text{eff}}^r}{4\pi d^2}, \tag{5}$$

where $G_t = \frac{4\pi A_{\text{eff}}^t}{\lambda^2}$. Therefore, we have

$$\frac{P_r}{P_t} = \frac{A_{\text{eff}}^t A_{\text{eff}}^r}{\lambda^2} \frac{1}{d^2}. \tag{6}$$

It is evident from (6) that for a fixed aperture area, the propagation loss decreases upon increasing in frequency. For example, let us consider a pair of transmit antennas with the same aperture areas and assume that one of the antennas employs a 80 GHz beam for transmission, while the other antenna transmits on a 2.4 GHz beam at the same transmit power. Then the ratio of the powers $P_r^{80\text{GHz}}$ and $P_r^{2.4\text{GHz}}$ received at a given distance using (6) is given by:

$$\frac{P_r^{80\text{GHz}}}{P_r^{2.4\text{GHz}}} = \frac{\lambda^{2.4\text{GHz}}}{\lambda^{80\text{GHz}}}. \tag{7}$$

Then, by substituting their respective wavelengths of $\lambda^{2.4\text{GHz}} = 0.125$ [m] and $\lambda^{80\text{GHz}} = 0.00375$ [m], $P_r^{80\text{GHz}}$ would provide 30 dB more gain compared to that of 2.4 GHz for the same transmit power and aperture area. Hence, transmission at higher frequencies would in fact provide higher gains, than at lower frequencies for a given antenna aperture area. However, the radiation pattern at higher frequencies becomes narrower.

B. Atmospheric Attenuation

Another propagation limiting factor of mmWaves is the atmospheric attenuation caused by gas molecules in the Earth's atmosphere [130], which is also known as gaseous attenuation [24]. The atmospheric attenuation is caused by the
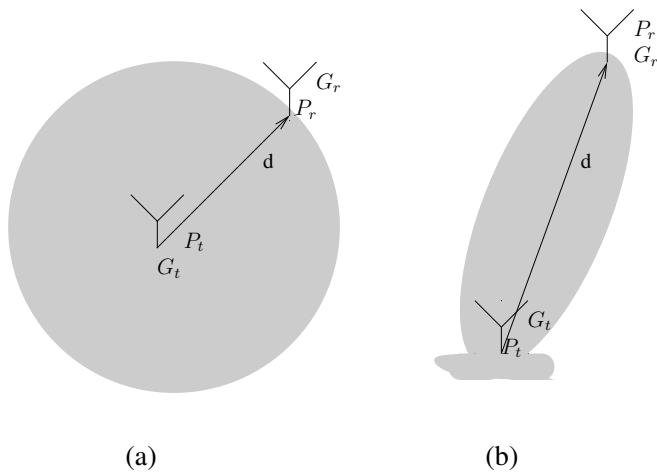
Figure 7. (a) Omnidirectional transmission (b) directional transmission, where G_t, G_r are transmit and receive antenna gains, and P_t, P_r are transmitted and received powers, respectively.

Figure 8. Specific attenuation curves of O_2, H_2O and rain at sea level. The term ρ refers to the density of H_2O in $grams$ per $meter^3$ [75], [130].

vibrating nature of air molecules when exposed to radio waves. Molecules absorb a certain portion of the radio wave's energy and vibrate with a strength proportional to the carrier frequency [24]. The two major absorbing gases at mmWave frequencies are the oxygen (O_2) gas and the water vapor (H_2O) gas [12], [15], [75], [82]. The intensity of gaseous absorption depends on several factors, such as the temperature, pressure, altitude and most importantly the operating carrier frequency [93] [133]. Figure 8 shows the specific attenuation per km of O_2 and H_2O at sea level, where the density ρ of water vapor H_2O in grams per m^3 considered here is 7.5 gm^{-3} at 1 atm ($atmosphere$) pressure following the ITU-R calculations in [133]. The Sea level at zero-meter altitude is considered as the worst case scenario for atmospheric attenuation, since at zero-altitude the air density reaches its maximum, while at higher altitudes the air density decreases, which culminates a reduced attenuation.

In Figure 8, the O_2 absorption curve maximas are observed at the 60 GHz and 119 GHz frequencies, at a record of 15 dB/km and 1.4 dB/km loss, respectively. However, by operating at short distances the oxygen absorption loss can be further reduced. For example, by reducing the cell range from 1 km to 100 m, the O_2 absorption at 60 GHz and 119 GHz drops to only 1.5 dB and 0.14 dB, respectively.

Furthermore, it is depicted in Figure 8 that H_2O molecules can resonate at 23 GHz, 183 GHz and 323 GHz, which are associated with a loss of 0.18 dB/km, 28.35 dB/km and 38.6 dB/km, respectively. Now, by combining both of the gaseous attenuation curves of Figure 8 into a single curve, the resultant curve subsuming both gaseous losses appears to have a minor effect, since the O_2 and H_2O bands of resonance do not match. Hence, atmospheric attenuation imposes an insignificant impact on mmWave signals, especially when transmitting over short distances.
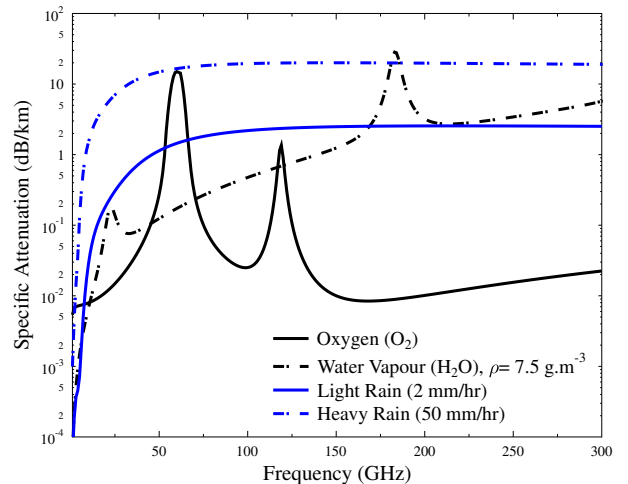
C. Rain-Induced Fading

The precipitation attenuation caused by the interaction between the propagating waves and the rain droplets at mmWaves cannot be neglected [12], [128], [130]. To expound a little further, the wavelengths of mmWave signals ranges between $1\,mm$ and $10\,mm$, while the size of a raindrop is typically in the order of few millimeters. Hence, due to their comparable sizes, which is illustrated in Figure 9, mmWave signals are more vulnerable to blockage by raindrops than signals with longer wavelengths. Note here that the teardrop illustration of raindrops shown in Figure 9 is intentionally used for illustrative purposes only, where in practice raindrops features a spheroidal shape [134]. This is clearly observed in Figure 8, where the specific rain attenuation γ_{Rain} at a given rain rate R in mm/hr increases exponentially up to the critical frequency, both for light rain and for heavy rain. Beyond this frequency the attenuation starts to decay slightly at a rate of milli-dBs per km. The figure is plotted according to the following relationship [134]:

$$\gamma_{Rain_{[dB/Km]}} = kR^{\alpha}, \qquad (8)$$

where k and α are functions of the operating frequency f in the range of $1\,GHz \leq f \leq 1000\,GHz$ and of other parameters, such as the temperature, polarization direction (e.g. horizontal and vertical), altitude and other factors. The rain-rate map is modeled by ITU-R [135] according to a given longitude and latitude positions. Both light and heavy rain attenuation losses are illustrated in Figure 8 at $2\,mm/hr$ and $50\,mm/hr$ rain rates. The attenuation curves of rain rates ranging between $2\,mm/hr$ and $50\,mm/hr$, such as the $10\,mm/hr$ and $25\,mm/hr$ rates, exist between the light and heavy rain curves in Figure 8. Moreover, the rain attenuation in the tropical region is studied in [136], where Mandeep et $al.$ proposed a modified ITU-R rain-attenuation model based on the curve fitting method for characterizing extremely heavy

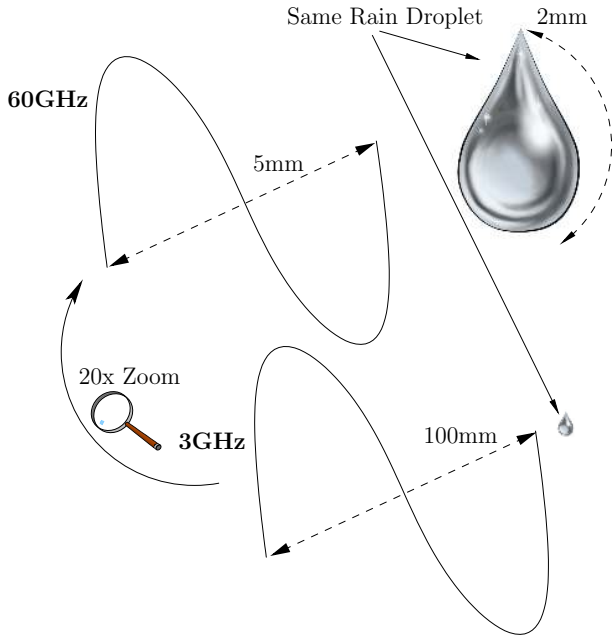tropical rain, which was underestimated in the ITU-R model [137].

Figure 9. An illustration of a 60 GHz and a 3 GHz signal's wavelengths compared to a 2mm-sized rain droplet. Note here that the teardrop representation of the raindrop is used for illustrative reasons only and does not represent the raindrop's actual spheroidal form.

Light and heavy rain-rates impose a maximum of $2.55\,dB/Km$ and $20\,dB/Km$, respectively, at the upper frequency bands of mmWaves. Considering short-range communications, these values can be further reduced, where a maximum of 2 dB attenuation loss is expected for heavy rain at a distance of 100 m. A monsoon down-pour was considered by Khan and Pi in [12] with a rate of $150\,mm/hr$, which has a maximum attenuation of $42\,dB/Km$ at frequencies over 60 GHz [15], [130]. In the lower bands of the mmWave spectrum, such as the 28 GHz and 38 GHz frequency bands considered in [6], [82], lower attenuations are observed with up to $7\,dB/Km$ for heavy rain, which drops to 1.4 dB at 200m.
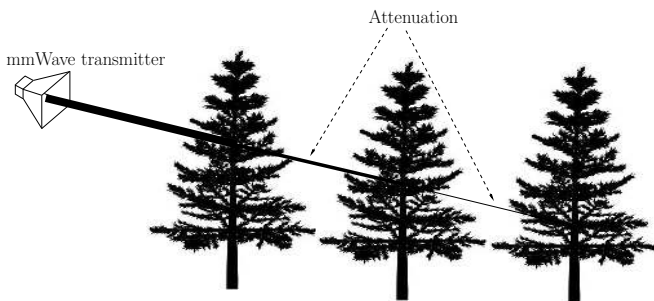

Figure 10. An illustration of foliage attenuation imposed by the presence of multiple trees, where the thickness of the lines shown illustrates the signal power.

D. Foliage Attenuation

Observe in Figure 4 that the foliage attenuation is an important attenuating factor at mmWaves. Vegetation presence between the transmitter and receiver adds extra attenuation to the signal and it may severely affect the Quality of Service (QoS) of a wireless communication system [99]. The severity of foliage attenuation depends on the depth of the vegetation component itself. For example, a single tree has a smaller effect than multiple trees, as illustrated in Figure 10. Moreover, a forest attenuates radio waves more severely than multiple trees. The general formula of foliage attenuation proposed in [138] is expressed as:

$$\gamma_{Foliage[dB]} = \alpha f^{\beta} D_f^c (\theta + E)^{\epsilon}, \qquad (9)$$

where f (MHz) and D_f (meters) are the carrier frequency and foliage depth and the regression parameters α, β, c, θ, E and ϵ are empirical parameters that depend on the model used, such as the Weissberger model [139], the ITU-R model [138] or the other models discussed in [140]. For example, the Weissberger model suggests that for distances less than 14 m, the last part of (9) is not considered, hence we have $(\theta + E)^{\epsilon} = 1$ and the values of α, β as well as c would be 0.45, 0.284 and 1, respectively. However, for distances less than 400 meters, they would be 1.33, 0.284 and 0.588. These values differ from one scenario to another and depend on the specific type of vegetation studied. In this survey we follow the ITU-R model used in [12], [15], [130], [140] expressed in (10). In this case, we have $(\theta + E)^{\epsilon} = 1$ and α, β as well as c are 0.5, 0.3 and 0.6, for distances less than 400m. The foliage attenuation can be represented using the following equation [12]:

$$\gamma_{Foliage[dB]} = 0.2 f^{0.3} D_f^{0.6}. \qquad (10)$$

In Figure 11, the attenuation of different foliage depths is plotted according to (10). For instance, at 28 GHz, 60 GHz and 90 GHz carrier frequencies, the foliage attenuation can be as high as 17 dB, 22dB and 25 dB, which is significantly higher than the 8.8 dB loss at 3 GHz. In a woodland, where several trees are more likely to perturb the LOS between the transmitter and receiver, $(\theta + E)^{\epsilon}$ is no longer equal to 1. However, the authors of [138] argue that in a a pine woodland of Austria, where the measurements where carried out, equation (9) would be equal to $0.25 f^{0.39} D_f^{0.25} \theta^{0.05}$. In this case, the effect of a 10m slant pine woodland, represented by the dashed line shown in Figure 11, is an order of magnitude higher than a 5 m deep foliage. A deep foliage, of say >10m, may attenuate the signal by a few dozens of dBs, even in the lower bands of the mmWave spectrum. On the other hand, this limitation can be reduced by using alternative techniques, such as cooperative communications [141], where multiple transmitters cooperate to deliver data to a receiver blocked with excessive foliage or by using relay stations in the canopy of huge or multiple trees.

More recently, the foliage attenuation measurements recorded for the wideband mmWave channel in the 73 GHz frequency band were presented by Rappaport and Deng in [99], demonstrating that employing a pair of highly directional antennas at the transmitter and receiver, the foliage attenu-
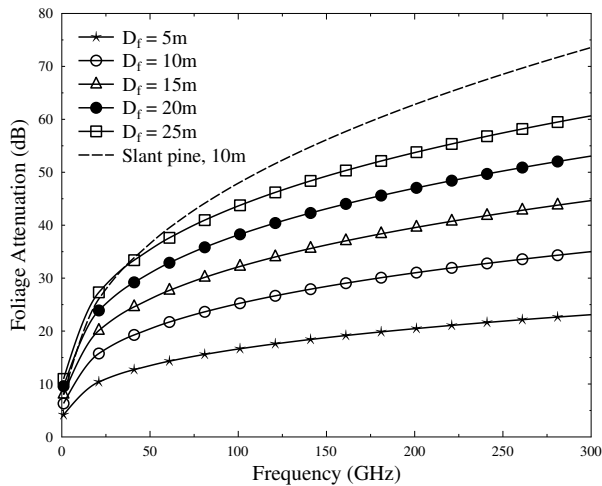
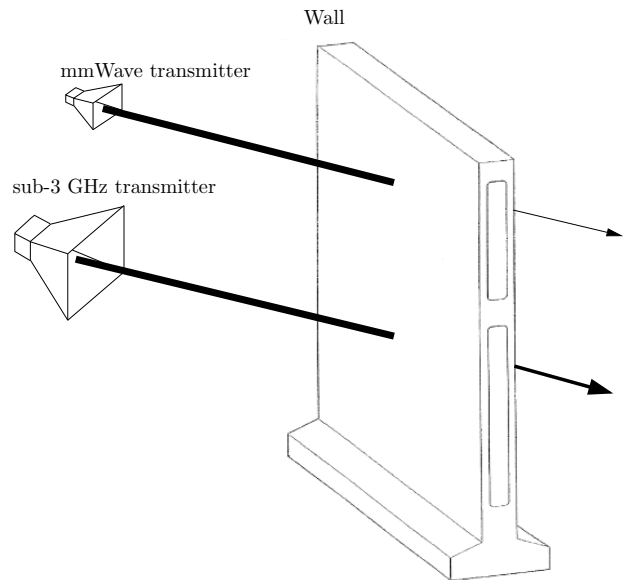Figure 11. Foliage Attenuation vs Frequency f [12], [130].

Figure 12. An illustration of a mmWave transmitter and a sub-3 GHz transmitter, where the thickness of the lines shown illustrates the signal power.

ation reaches 0.4 dB/m for both co-polarization and cross-polarization configurations.

E. Material Penetration

The mmWave frequencies cannot propagate well through obstacles, such as for example room furniture, doors, walls and other paraphernalia severely attenuate mmWaves signals [15], [63], [142]. Several penetration losses of different materials in excess of FSL given by Equation (1) in dB/cm at 2.5 GHz, 28 GHz, 40 GHz, 45 GHz, 60 GHz and 73 GHz frequency bands are shown in Table II. In an indoor office environment, a 1.9 cm thick office whiteboard attenuates a 60 GHz signal by 9.6 dB, which is 9.1 dB more than that of signals below 3 GHz [15], as for example illustrated in Figure 12. The coverage of indoor systems operating at the sub-3 GHz would encompass more rooms than a system operating at the 60 GHz band, which is generally restricted to a single room [122]. However, the indoor measurement campaign reported by Nie *et al.* in [64] at the 72 GHz frequency band shows that the penetration losses of the 72 GHz band are slightly higher than those of the sub-5 GHz used for WiFi, which advocates it as a strong nominee for the future multi-Gbps indoor communications. On the contrary, high penetration losses occur in in outdoor communication systems operating at the 28 GHz band, as for example reported by Zhao *et al.* in [58], where the 28 GHz signal is attenuated by as high as 24.4 dB and 45.1 dB when when penetrating through two walls and four doors, respectively [58].

The high penetration loss of signals arriving from outdoors in indoor environments limits the range of the covered area and emphasizes the need for Heterogeneous Networks (HetNet)[3] [144] in providing coverage for the obstructed environments

[6], [57], [109]. Explicitly, HetNets would allow a wireless system to communicate with a user suffering from an obstructed mmWave link through a different wireless technology, such as the existing legacy wireless systems operating in lower frequency bands [82].

F. Propagation Mechanisms

The propagation mechanisms shown in Figure 4 consist of the ray's specular reflection, diffuse scattering and diffraction, as depicted in Figure 13. These mechanisms have shown a substantial impact on mmWaves [45], [51], [145]. Due to the short wavelengths of mmWave signals, ranging between $1\,mm$ and $10\,mm$, their propagation mechanisms are drastically different from those the sub-3 GHz, and hence have to be carefully studied and modeled to understand the mmWave channel. Small structural features that are comparable in size to the millimeter wavelengths, endure a rich diffused scattering, where each reflected ray has a different reflection direction leading to a scattered power reception and to a poorer smooth surface specular reflection [51], [130], as shown in Figure 13. Another prevalent consensus concerning mmWave signals is that they are more prone to the diffraction mechanism than to its reflection counterparts of Figure 13. This can be explained by their mm-long wavelengths, which constrains them to diffract rather than to reflect or to scatter over large structures and objects with smooth surfaces, which nonetheless can be blocked by smaller objects as compared to their sub-3 GHz frequency counterparts. This is due to the mmWaves' narrower first Fresnel zone that is directly proportional to the wavelength [43], [82]. Hence, objects as small as few tens of centimeters appear to be large in size compared to the signal's wavelength, which leads to lesser ray diffraction and higher shadowing effects. However, in some indoor scenarios, mmWave communication can rely on the diffracted rays especially in an NLOS environment, as for example suggested by

---

[3]Heterogeneous Networks is a term relying on the coordination of different cell types in communication networks

Material	2.5 GHz [122]	28 GHz [58]		40 GHz [51]		45 GHz [143]		60 GHz [122]	73 GHz [127]	
		MTC	WWH	V-V	H-H	V-V	H-H		V-V	V-H
Clear Glass	20	3	2.76	2.5/0.4	7.75	-	-	11.3	7.1	18.3
Tinted Glass	-	-	18.84	-	-	-	-	-		
Mesh Glass	24.1	-		-	-	-	-	39.1		
Brick	-	-	0.15	-	-	-	-	-	-	
Drywall	2.1	-	0.17	-	-	-	-	2.4	0.8	0.8
Whiteboard	0.3	-	-	-	-	-	-	5.0	3.5	2.7
Plasterboard	-	-	-	1.93	1.8	-	-	-	-	
Closet Door	-	-	-	-	-	-	-	-	4.6	2.3
Steel Door	-	-	-	-	-	-	-	-	9.9	9.2
Glass Door	-	-	-	-	-	-	-	-	5.1	23.4
Brick Wall	-	-	-	19.5	17.7	-	-	-	-	-
Chipwood	-	-	-	5.37	4.93	-	-	-	-	-
Wood	-	-	-	5	3.71	4.19	2.42	-	-	-
Concrete	-	-	-	17.8	17.4	4.64	4.38	-	-	-
Mortar	-	-	-	15.9	15.9	-	-	-	-	-

Table II
PENETRATION LOSSES OF DIFFERENT MATERIALS IN EXCESS OF FSL IN dB/cm AT 2.5 GHz, 28 GHz, 40 GHz, 45 GHz, 60 GHz AND 73 GHz FREQUENCY BANDS. THE METROTECH CENTER (MTC), WARREN WEAVER HALL (WWH) REFERS TO TWO DIFFERENT MEASUREMENT LOCATIONS, WHILE V AND H DENOTES THE VERTICAL AND HORIZONTAL ANTENNA POLARIZATION CONFIGURATION.
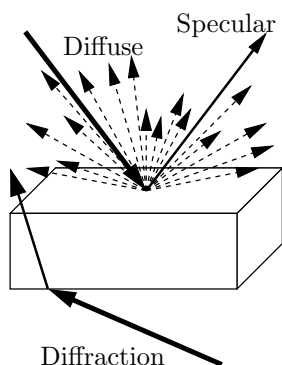

Figure 13. An illustration of different propagation mechanisms, namely specular reflection, diffuse scattering and diffraction. The rectangular reflecting/diffracting surface used is for visualization purposes only and does not intend to characterize a real scenario.

Geng *et al.* in [125], where two diffracted waves were detected at 60 GHz. By contrast, communications in outdoor scenarios cannot readily rely on diffracted paths, they rather rely on the reflected paths [146].

Furthermore, in mmWave communications, communication nodes narrow-beam directional transmit and receive antennas are employed for overcoming the high FSL. In case of beamforming-aided directional communications, the propagation mechanisms of Figure 13 may cultivate a multipath propagation channel characterized by both the LOS component as well as the reflected and diffracted components, which would aggregate a limited number of Multipath Components (MPCs) of those that fall within the transmit and receive antennas' beam-ranges. This would potentially reduce the inter-multipath components interference, but would also result in capturing a limited the number of MPCs [15], [46].

Several measurement campaigns and studies were carried out to discover the mmWave propagation mechanisms at different bands [45], [51], [58], [60], [63], [95], [115], [119], [125], [142], [146]. In a NLOS scenario, the link between the Tx and Rx is obtained by relying on both the reflected and the scattered MPCs, and would undergo an outage when they are both totally blocked [46], [59]. Furthermore, the reflected MPCs suffer from a high attenuation, regardless of how small a cell size [147]. Zhao *et al.* reported in [58] that at 28 GHz, the outdoor materials appear to be more reflective than their indoor counterparts.. Thus, strong links can be established in outdoor systems at 28 GHz by relying on reflected paths.Similarly, in an indoor scenario operating at the 60 GHz frequency band, Xu *et al.* reported in [142] that the received signal primarily constitutes both the LOS component as well as the single-bounce reflected waves and the twin-bounce reflected waves [125], where the associated terminology refers to the number of reflections that have occurred during the signal's propagation from the transmitter to the receiver. For example, an 8 dB loss compared to the received LOS component was recorded by Xu *et al.* in [142] after a single-bounce reflection from a blackboard, whereas a 15 dB loss was recoreded by Geng *et al.* in [125]. The rule of thumb here is that acquiring more reflected paths typically imposes higher power attenuation. Hence, a link is set up in an indoor and an outdoor scenarios by relying both on the LOS or NLOS nature of the system considered as well as on

the medium's materials' reflective characteristics.

G. Other Propagation Factors

mmWave frequencies are also sensitive to other factors, such as Doppler spread and human blockage [37], [75], [94], [102], [130], [148]. The Doppler spread results in frequency dispersion is caused by the mobility of the communicating nodes and its stiffness is proportional to both the frequency and to the speed of mobility. Hence, the Doppler spread at mmWaves is significantly higher than at frequencies below 3 GHz, when considering omni-directional and rich scattering environments [37], [82]. For example, the Doppler spread at 30 GHz and 60 GHz is 10 and 20 times higher than at 3 GHz [37], and it can reach 16 KHz at a speed of 80 km at 60 GHz. However, this value can be significantly reduced by invoking directional antennas that reduce the incoming MPCs angular spread [82].

Furthermore, human presence between the transmitter and the receiver severely attenuates the received signal [102], [148], [149], which may become as high as 25-30 dB for a single person [94]. Hence, it may reduce the network throughput by 10%, given a human density of one person per $10\,m^2$ [75]. Furthermore, it was reported by Wu *et al.* in [102] that up to 42% of the signal power incident on the human skin is reflected at 60 GHz. However, Collonge *et al.* reported in [148] that the severity of human shadowing is not influenced directly by the number of blocking persons, but rather by the Tx and Rx antenna configurations, such as patch and horn antennas [148]. This was in fact substantiated by MacCartney *et al.* in their double diffraction human blockage model proposed in [150], where their results showed that in addition to the human blockage effect, the severe shadowing is conjointly subsidized with the antenna brand employed. Furthermore, MacCartney *et al.* stressed that using electronically steerable and high-gain directional antennas, the human shadowing is reduced. Furthermore, an additional diffraction and/or reflection gain of 1-2 dB is provided by the diffracted and/or reflected MPCs around the shadowed area, as shown in Figure 14.

III. THE MILLIMETER WAVE CHANNEL MODEL

Prior to understanding the radio propagation characteristics in any frequency band, it is essential to develop its corresponding channel model. At mmWaves, accurate modeling is a crucial prerequisite of designing an efficient communications system operating at this frequency band for developing new techniques that can adapt to its propagation characteristics, as illustrated in Figure 2. This section describes the channel model used for representing the narrow-band and Ultra-Wideband (UWB) mmWave channel.

Channel models are generally classified into two categories, which are shown in Figure 15, known as physical models and analytical models [151]. A physical channel model is constructed based on the electromagnetic (EM) characteristics of the signal propagating between the transmit and receive antenna arrays, whilst an analytical channel model is described based on the mathematical analysis of the channel.
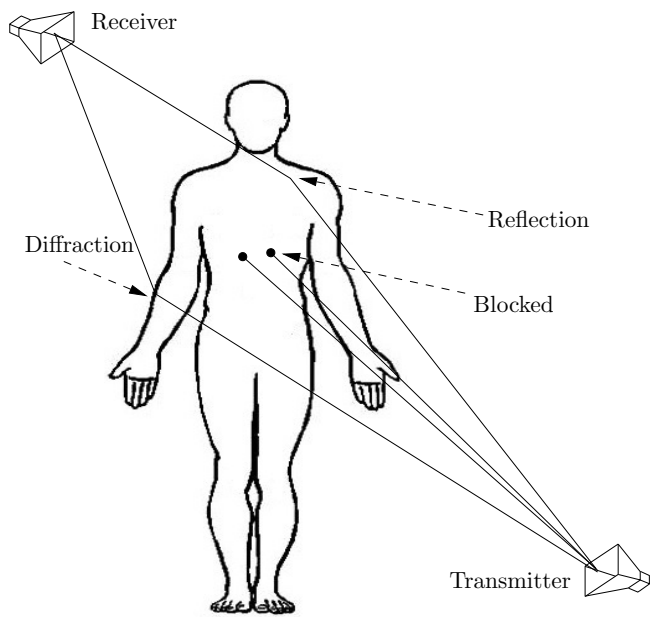

Figure 14. Human blockage of the communication between a transmitter and a receiver.

Here, we only consider the physical channel models, since they can efficiently reflect the measured channel parameters and are also popular for MIMO channel modeling [152]. By contrast, analytical models, such as the correlation-based Kronecker [153], [154] and Weichselberger [155] channel models as well as the propagation-based finite scatterer [156], maximum entropy [157] and virtual channel representation [158] models, characterize the communication channel mathematically and can be derived from physical models. These models are best used for algorithm development and system analysis.

As shown in Figure 15, the physical channel models are further divided into two groups: deterministic and stochastic physical models [151]. Deterministic models explicitly characterize the real effect of the environment on the system, but at the cost of a higher computational complexity. Ray-Tracing (RT) techniques [159]–[161] are best suited for characterizing deterministic models, such as mmWave channel models [103], [160], [162], [163]. RT is generally implemented using a stand-alone software package to simulate a desired channel scenario, where all environmental features are known and stored in the system. Another advantage of deterministic models, especially of ray tracing models, is the when no measurements are available for a specific scenario, these deterministic models can be readily utilized for predicting the characteristics of the new environment. This eliminates the huge cost of measurement campaigns [99], [159], [163], [164]. At mmWave frequencies, several studies involved the ray tracing model for predicting the propagation behaviour of the channel in diverse scenarios, as in [103], [142], [151], [160], [164]–[166]. Additionally, several treatise used the ray tracing model to extract and analyze the physical characteristics of the channel, as in [76], [99], [142], [162], [165], [167].

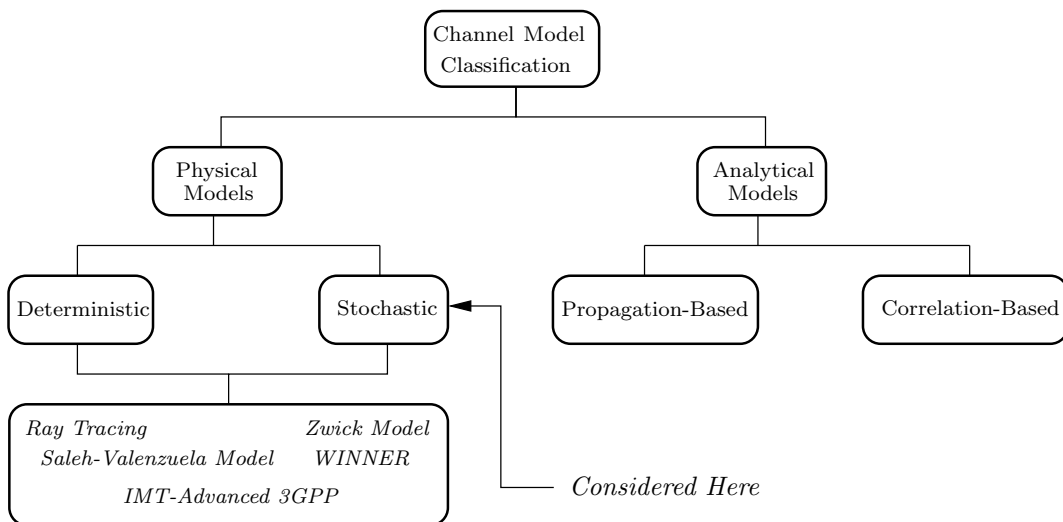In contrast to deterministic models, stochastic models pro-

Figure 15. Channel classification according to [151] showing that the stochastic channel models is considered in this review, as characterized by the "Modeling Method" roundabout of Figure 2.

duce the channel's impulse response describing the spatio-temporal characteristics of the channel's MPCs as a probabilistic model based on extensive measurements taken in different scenarios and environments. Generally, the probability density functions (PDFs) of channel parameters are used for characterizing both the large-scale and small-scale fading components [151], [168]–[170]. Some examples of stochastic models include the Saleh-Valenzuela (SV) model and its extended versions (e.g. Triple-SV (TSV) model) [67], [171], [172], the 3rd Generation Partnership Project (3GPP) Spatial Channel Model (SCM) [170] and Zwick model [173], where the more parameters the channel model includes for characterizing more channel attributes, the better its accuracy becomes [174]. Stochastic channel models are considered to be simple models that require less time and lower computational complexity, hence they are best used for system design and simulation.

Existing channel models can be adopted for mmWave channels by modifying the key parameters extracted from measurement campaigns, which depend both on the carrier frequency and on the surrounding environment, such as indoor, outdoor, urban or rural scenarios [7], [66], [72], [76], [77], [80], [103], [175], [176]. Several contributions relied on statistical models [8], [46], [67], [76], [82], [103], [177], [178], while other studies were based either on analytical models or on ray tracing techniques under idealized simplifying assumptions [8], [38], [46], [75], [179]. Both of these models may deliver inaccurate results [7]. Since the RT relying on unrealistic parameters does not reflect the channel's behavior accurately and the analytical models are only fit for theoretical evaluations, the resultant simulation results are also likely to be unrealistic.

Lately, several frequency bands of Table I, have been extensively characterized, especially the bands of high interest, such as the 28 GHz, 38 GHz, 60 GHz and 73 GHz frequency bands [6], [75]–[79], [99], [102], [103], [180]. The 60 GHz band and the 70 GHz as well as 80/90 GHz frequency bands

[15], [82] have also attracted much attention. Based on these measurements, channel models have been produced for several mmWave bands in [6], [7], [14], [27], [69], [76], [77], [98], [103], [120], [125], [167]. We commence by presenting the early stages of mmWave narrow-band channel characterization studies an then we proceed to specifying the recent advancements on the wideband mmWave channel models.

A. mmWave Channel Modeling Efforts

While designing the next generation mobile technology referred to as the 5G [6], [43], [71], [103], [110], [181]–[183], several research contributions have proposed channel models for carrier frequencies ranging from 2 GHz up to 100 GHz. In Table III, we list several projects that have proposed appropriate channel models for the different frequency bands, such as 28 GHz, 38 GHz, 45 GHz, 60 GHz and 72 GHz as well as for indoor, outdoor, backhaul scenarios including LOS and NLOS environments and diverse technologies, such as mobile networks, personal networks, etc. Furthermore, we included a timeline representation of these projects in Figure 16. In the following we will briefly describe these projects and their findings.

- *The Task Group 3c (TG3c) TG3c*: After the very first propagation study of the 60 GHz channel at BELL Labs in the early 1980's [198], the interest in modeling the channel was rekindled after considering shifting the Wireless Personal Area Network (WPAN) from the sub-3 GHz towards the 60 GHz band [67], [199]. Hence, huge modeling efforts have been dedicated to mmWaves during the standardization process of the 60 GHz WPAN IEEE 802.15.3c standard [14], where standardization is one of the crucial prerequisites for bringing the mmWave technology to life, as shown in Figure 2. The mmWave WPAN standard adopted the TG3c channel model, which is based on the SV model with its parameters extracted

Technology	Frequency	Year	Channel Model	Description
WPAN	60 GHz	2007	TG3c [14]	Proposed a mmWave channel model for the 60 GHz IEEE 802.15.3c, where 9 scenarios with both NLOS and LOS environments are identified as CM1, CM2, CM3, CM4, CM5, CM6, CM7, CM8 and CM9.
WLAN	60 GHz	2010	TGad [27], [184]	Statistical channel model of the indoor WLAN 60 GHz channel. The effect of beamforming and antenna polarization was considered.
WLAN	60 GHz	2014	Cluster double directional model [69]	Measurement based double directional channel model for indoor scenario at the 60 GHz band.
Indoor	60 GHz, 70 GHz	2015	Statistical channel model [185]	Proposed channel model based on spatio-temporal indoors measurements carried at the 60 GHz and 70 GHz.
Indoor	45 GHz	2015	Hybrid channel model [186]	Hybrid 45 GHz channel model for indoor conference room. The proposed model is based on both measurements and ray-tracing.
5G	up to 100 GHz	2012	METIS [149]	mmWave channel model for mobile systems referred to as the 5G PPP. It is based on the WINNER II [187] and WINNER+ [188] channel models.
5G	60 GHz	2014	MiWEBA [189]	Proposed a 3D channel model for mmWave, which supports beamforming at the transmitter and beam-combining at the receiver and applies the effect of antenna polarization.
5G	30 GHz	2014	QuaDRiGa	Originally based on the WINNER II model, the QuaDRiGa model supports 3D channel representation at mmWaves and it features a spatially-correlated channel model.
5G	28 GHz, 38 GHz and 72 GHz	Since 2011	5GCM	Extensive research effort on mmWave channel model at mainly the 28 GHz, 38 GHz and 72 GHz frequency bands. Started from proposing a narrow band channel model [7] to multiple wideband channel model proposals [99], [180], [77], [78], [98] [59], [72], [76], [79], [80], [105], [106], [190]
5G	up to 100 GHz	2017	3GPP	The 3GPP TR 38.900 channel model is an extension of the 3D 3GPP TR 36.873 channel model, which is restricted to the sub-6 GHz band. This model supports the elevation angular characteristics of the channel as well as its azimuthal characteristics. It also supports frequency bands up to 100 GHz over several scenarios, such as UMa, UMi, D2D, indoor, etc.

Table III

mmWave channel modeling projects contributing to the "Standardization" entrance of Figure 2.

from measurements conducted in the 57-64 GHz band. The channel model considered 9 different scenarios that describe different short-range networks denoted as Channel-Model-x (CMx), such as CM1 and CM2 for residential rooms, CM3 and CM4 for office set-ups, CM5 and CM6 for small libraries and CM7 and CM8 for small office desktop scenarios associated with LOS/NLOS environments in addition to CM9 used for kiosks supporting portable devices, as detailed in Table IV.

- *TASK GROUP ad (TGad)*: Later the indoor short range channel model was extended to Wireless Local Area Networks (WLAN) using the IEEE 802.11ad standard [27]. The TGad model is a modified version of the TG3c model, where the beneficial impact of both beamforming and polarization were explicitly considered. In the TGad channel model, the channel parameters were extracted from measurements carried out in indoor 60 GHz scenarios, which was further generalized to multiple scenarios, including conference rooms, cubicle and living room scenarios using the RT technique [184].
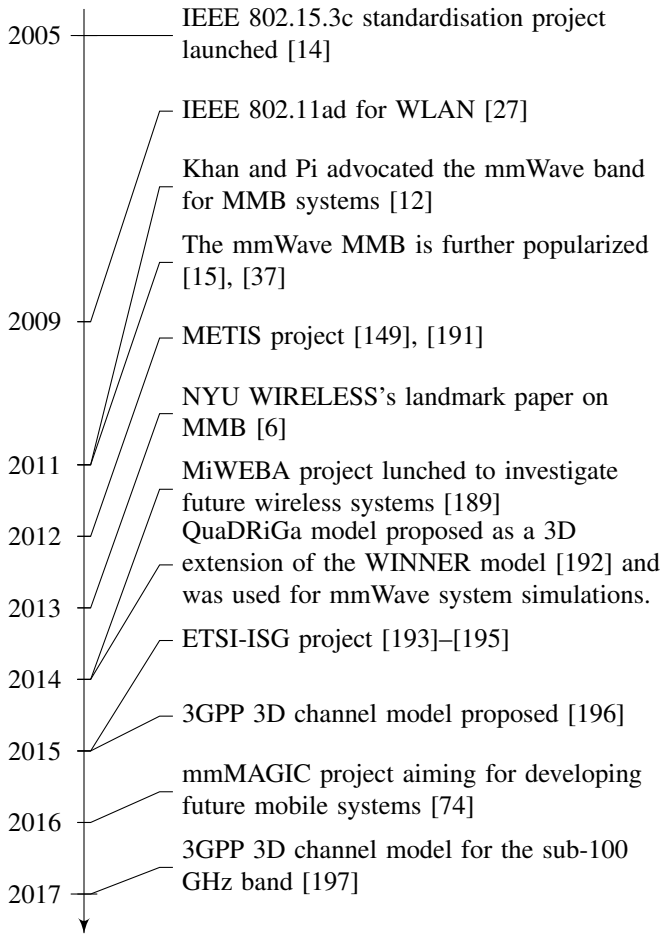
2005	IEEE 802.15.3c standardisation project launched [14]
2009	IEEE 802.11ad for WLAN [27]
	Khan and Pi advocated the mmWave band for MMB systems [12]
	The mmWave MMB is further popularized [15], [37]
	METIS project [149], [191]
2011	NYU WIRELESS's landmark paper on MMB [6]
2012	MiWEBA project lunched to investigate future wireless systems [189]
2013	QuaDRiGa model proposed as a 3D extension of the WINNER model [192] and was used for mmWave system simulations.
2014	ETSI-ISG project [193]–[195]
2015	3GPP 3D channel model proposed [196]
2016	mmMAGIC project aiming for developing future mobile systems [74]
2017	3GPP 3D channel model for the sub-100 GHz band [197]

Figure 16. Timeline of mmWave channel models.

Scenario	Channel Model	LOS/NLOS
Residential	CM1	LOS
	CM2	NLOS
Office	CM3	LOS
	CM4	NLOS
Library	CM5	LOS
	CM6	NLOS
Desktop	CM7	LOS
	CM8	NLOS
Kiosk	CM9	LOS

Table IV

THE NINE DIFFERENT CHANNEL MODELS PROPOSED BY THE TG3C GROUP BASED ON DIFFERENT SCENARIO SETTINGS.

- *METIS*: The Mobile and wireless communications Enablers for the Twenty-twenty Information Society (METIS) project [149] developed a mmWave channel model for the 60 GHz frequency band, for specific situations, which cannot be adequately represented by the existing channel models. The METIS channel model is based on the existing channel models, such as the WINNER II [187] and WINNER+ [188] models, whose inadequacies were carefully taken into consideration during the channel modeling process. The METIS project proposed three channel models, namely the stochastic, map-based and hybrid models, where the stochastic model is suitable for frequencies up to the 70 GHz band, while the map-based model is applicable for frequency up to the 100 GHz band. The project covered a range of indoor and outdoor scenarios, such as dense Urban Macro (UMa), Urban Micro (UMi), rural, highway, indoor shopping mall, festival, office, Device-to-Device (D2D) and Vehicular-to-Vehicular (V2V) situations.

- *MiWEBA*: In the Millimeter-Wave Evolution for Backhaul and Access (MiWEBA) project [189], a 3D channel model was proposed for the 60 GHz band, which is capable of supporting beamforming at the transmitter as well as beam-combining at the receiver and additionally exploits antenna polarization. The project covered three specific scenarios, namely back-haul, D2D and mobile access in specific cases, such as a typical university campus, street canyon and hotel lobby. The MiWEBA channel models are hybrid models, which combine measurement-based parameters with existing models in order to characterize both strong and weak MPCs of the channel.

- *3GPP Model*: The SCM channel model [170], as well as its derivatives [144], are based on a 2D plane representation, where all the channel's characteristics, such as AoA, AoD and antenna geometries are viewed in a 2D plane. For example, only the azimuth angle is considered for the spatial characteristics. More recently, a 3D representation of the 3GPP channel model TR 36.873 was proposed in [196] for the sub-6 GHz frequency band with up to 100 MHz channel bandwidth. This 3D model can capture the elevation angle dimension of the channel in addition to the azimuth angle dimension [2]. A newly proposed 3GPP model, namely the 3GPP TR 38.900 3D model [197], extends the TR 36.873 channel to support frequency bands up to 100 GHz over several scenarios, such as UMa, UMi, D2D, indoor, etc.

- QuaDRiGa Model: The Quasi Deterministic Radio Channel Generator (QuaDRiGa) model was first developed by Jaeckel *et al.* in [192] as a 3D extension of the WINNER model [187]. It is an open-source platform available in [200], which was originally proposed for simulating sub-6-GHz systems but was employed later for mmWave systems simulations [201].

- Intensive 5G channel modeling efforts: Based on extensive measurements at the 28 GHz, 38 GHz, 60 GHz and 73 GHz, multiple channel models were proposed by NYU WIRELESS under the title of 5G Channel Model (5GCM), gradually evolving from the narrow band representation of [7] to the latest wideband channel models of [103] and [72], [79], [80], [105], [202]. The mmWave channel model proposed in [99], [180], [55], [77], [78], [98], [59], [72], [76], [79], [80], [105] was termed as the Ultra-Wideband (UWB) mmWave channel following the foundations in [176], due to the huge available bandwidth, as it will be discussed in the following section. Different indoor and outdoor scenarios were considered, with an emphasis on mobile access for mmWave mobile broadband (MMB) services, for backhaul, D2D and V2V

scenarios.

- *Other indoor channel models*: Correspondingly, Haneda *et al.* proposed in [54] a spatio-temporal channel model for large rooms operating in the 60 GHz and 70 GHz bands. This channel model is based on measurements carried out in indoor short-range scenarios, such as train stations, offices, shopping malls etc. Furthermore, Dou *et al.* proposed in [186] a hybrid channel model for the 45 GHz band for indoor scenarios, where the channel parameters were extracted from both measurements and ray-tracing simulations.

Another project known as the COMMINDOR project [114], [203], [204] was carried out in France for the sake of achieving a "very high speed" of 155 Mbit/s, in the early 2000s, for short-range residential scenarios operating at 60 GHz. Zhang *et al.* employed the RT technique in [46] in order to characterize a directional 60 GHz multipath channel based on a 2×2 MIMO system. This work was further refined by Torkildson *et al.* in [45] by employing a six-ray channel model for an outdoor scenario in the 60 GHz band. Furthermore, the measurements conducted in [205] were used for modeling the path-loss for an indoor scenario associated both with LOS and NLOS environments for transmission over a 60 GHz channel using both omni-directional as well as directional transmit and receive antennas. Azzaoui and Clavier introduced in [206] a statistical channel model for a 2 GHz wide channel. Another 60 GHz channel model based on the shooting and bouncing [161][4] RT technique was reported by Kazemi *et al.* in [167], where the parameters were extracted from extensive simulations of existing measurements, such as those in [142].

Furthermore, in early 2015 the European Telecommunications Standards Institute (ETSI) held the first meeting of its Industry Specification Group (ISG) on mmWave transmission, where the main objective was to investigate the 60 GHz and the 71 to 86 GHz bands for mobile back-hauling and mobile access [193]–[195]. In the same year, the mmMAGIC project was launched as part of the European Commission's initiative on 5G partnership with many major industrial contributors [73], [74]. The mmMAGIC project is investigating the employment of mmWaves for 5G to tackle the main challenges of the current mobile systems, including the support of dense networks having a high grade of flexibility and performance [74]. The main efforts were invested during the 2010s into acquiring knowledge about the sub-100 GHz band of mmWaves as hallmarked by the COST2100 [207] initiative. Moreover, another COST initiative characterizing the mmWave channel is the IC1004 Action [208], which aims for identifying the main characteristics of the frequencies spanning between 24 GHz and 86 GHz for 5G systems operating both in indoor and outdoor scenarios.

Another group known as the National Institute of Standards and Technology (NIST) 5G mmWave Channel Model Alliance was first established in mid-2015 and it aims, likewise, for characterizing the mmWave channel. Specifically, this alliance

---

[4]'shooting and bouncing' is one of two main techniques used for 3D-channel tracing. The other method is referred to as image based ray tracing [159].

is divided into six sub-groups that collaboratively participate in characterizing the mmWave propagation channels of indoor, outdoor and other scenarios [209].

On the other hand, the modeling efforts dedicated to the 28 GHz channel started much earlier with the objective of using this band for mobile broadband networks [37], where the measurements carried out by Papazian *et al.* in [97] in the 28 GHz band were targeting the Local Multipoint Distribution Service (LMDS) before it failed during the spectrum auction. The authors used a simple tapped delay line model for mimicking the multipath 28 GHz channel. Similarly, another channel model was proposed by Xu *et al.* in [63] for a point-to-point scenario operating at the 38 GHz frequency band. The same scenario was revisited later by Rappaport *et al.* in [98] in a peer-to-peer scenario.

B. Modeling Challenges

Numerous channel models exist in the literature, such as the WINNER II [187], WINNER+ [188], 3GPP [170] and COST [207], [210] models. However, these models cannot adequately reflect all features of mmWaves, as it will be shown in this section. The key challenge recognized by the MiWEBA project is the ability to produce a single channel model for mimicking the entire mmWave spectrum, where the parameters would be modified based on the operating frequency, depending on the nature of the scenario (indoor, outdoor, etc.) and on the environment (LOS/NLOS) [189]. However, the METIS project [149] claimed that this cannot be achieved at mmWaves, hence it proposed three different channel models: the map-based, the stochastic and the hybrid mmWave models, where the latter is a combination of the former two types. The main limitations of the existing channel models are shown in Figure 17, which can be briefly described as follows:

- **Lack of Measurements**: The propagation characteristics of mmWaves presented in Section II suggest that mmWave signals suffer from high attenuation and sparse multipath scattering. Despite the extensive measurement campaigns conducted in the 28 GHz, 38 GHz, 60 GHz and 72 GHz bands, the propagation characteristics of a wide mmWave range remain unknown.
- **3-D Models**: mmWave systems are expected to apply 3D beamforming [76], [100], where instead of limiting the beamforming to the azimuth dimension, the system additionally exploits the 3D spatial dimension of the MIMO system by additionally utilizing the elevation dimension for the sake of achieving both transmit beamforming and receive combining gains.
- **Bandwidth**: the huge contiguous bandwidths available at the mmWave frequency band imposes some restrictions on the channel model employed. As discussed in Section III-A, the original 3D 3GPP TR 36.873 model was designed for supporting the sub-6 GHz band with a maximum of 100 MHz bandwidth [2]. Due to the relatively narrow bandwidth of this model, it is not directly applicable for mmWaves due to their higher operating frequencies and wider bandwidths. Hence, the 3GPP TR
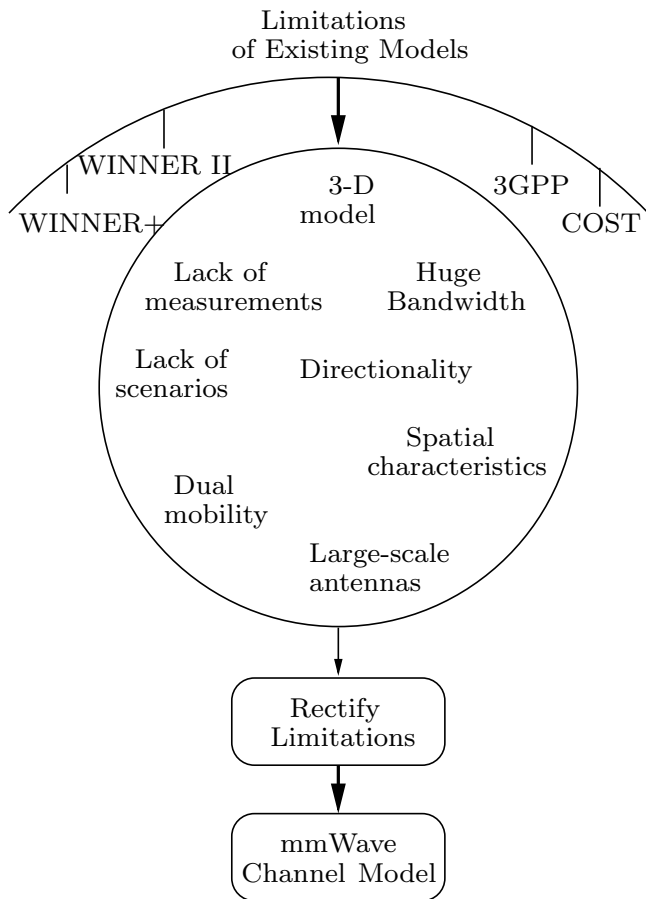
[149] and [189].

- **Directional Antennas**: The Doppler spread effect may be reduced by employing directional antennas, as argued by Pi and Khan in [15], where the directionality of antennas is essential for mitigating the high signal attenuation experienced at mmWaves. Hence, the effect of directional antennas should be taken into consideration for mmWaves channel modeling, in particular for the path-loss model, because most channel soundings were carried out using directional transmit and/or receive antennas [28], [57], [213].

- **Large-scale antennas (Massive MIMO)**: At mmWave frequencies, high number of AEs could be packed into a compact area, which enables the employment of Massive MIMOs [81]. Then narrow pencil beams could be created [37], which require a high angular resolution for capturing the related channel characteristics. Furthermore, mmWave systems with large-scale antenna settings require utilizing spherical wave models, rather than a planar wavefront [191], especially for short-range communications [214].

C. General Structure of The mmWave Channel

The mmWave radio channel is predominantly dispersive in the light of the short symbol interval of Gigabit transmissions [6], [37], [82], [179], where the impulse response of the channel between the Tx and Rx is formed by the aggregation of individual MPCs received within all clusters. A cluster can be simply defined as a group of MPCs, or rays, sharing the same spatial[5] and/or temporal[6] characteristics. In a MIMO system associated with N_t and N_r transmit and receive antennas, respectively, the aggregated channel matrix of clusters and rays can be modeled as:

$$H\left(t\right) = \sum_{n_{cl}}^{N_{cl}} \sum_{p}^{N_p} H_{n_{cl},p}\left(t\right) , \qquad (11)$$

where N_{cl} represents the total number of aggregated clusters with N_p rays within each cluster, while $H_{n_{cl},p}\left(t\right)$ is a single channel contribution of the p-th ray in the n_{cl}-th cluster at time instant t.

A multipath cluster has a number of somewhat different definitions in the literature [7], [69], [170], [215], but all agree that a single cluster is defined as a group of rays sharing the same general characteristics that can be distinguished from one group to another, such as the time-and spatial-domain characteristics. Hence, it is essential to differentiate the parameters of each cluster in order to characterize the channel impulse response.

In that sense, the early work on the SCM identified a cluster by its spatial characteristics [6], [7], [82]. These studies followed the channel model of the IMT-Advanced 3GPP initiative [170], where the clusters are defined by their central angles and their delay, the angular-and time-spreads and power

Figure 17. Current channel models exhibit many limitation that have to be rectified to be applicable for modeling mmWave channels.

38.900 channel model is rather employed. Furthermore, the 3-D channel models proposed by Samimi *et al.* in [202], [211] are considered to be 3GPP-like stochastic channel models that are capable of producing its temporal and spatial 3-D characteristics.

- Owing to the fact that mmWaves are likely to be used in future communications systems [103], [178], additional scenarios are needed, such as sport halls and crowded festivals [149]. Furthermore, the propagation characteristics of a huge portion of mmWaves remains unknown for many evolutionary network concepts, including the popular Heterogeneous Networks (HetNets) concept [144], which has to be studied.

- **Spatial Characteristics**: The mmWave channel is a sparse multipath channel, where users located close to each other would receive the same signal via the same reflected paths [178], which means that these users would experience the same Angle-of-Arrival (AoA) and Angle-of-Departure (AoD) that should be accounted for in the mmWave channel model.

- **Dual Mobility**: The 'dual mobility' scenario of a pair of moving nodes is mainly encountered in Device-to-Device (D2D) communications [212], where a higher Doppler spread is expected compared to the centralized base station scenario. This issue was mainly addressed in

---

[5]The spatial characteristics represents the angular aspects of the arriving and departing MPCs.

[6]The temporal characteristics are based on the time distribution of different MPCs.

distribution. Furthermore, the clusters' specific identification was further discussed in the 60 GHz band in [14], [27], [69], [125], [142], [216], where each cluster is defined by its angular and temporal characteristics.

Channel Model	
Large-Scale Fading	**Small-Scale Fading**
Cluster Power Path loss (PL) Shadow fading (S_σ) Angular Spread (σ_{AS}) Delay Spread (σ_{DS}) Clusters count (N_{cl})	Instantaneous multipath gain $\alpha(t)$ $AoD \sim PDF(\bar{\phi}_{AoD}, \sigma_{AS}^{AoD})$ $AoA \sim PDF(\bar{\phi}_{AoA}, \sigma_{AS}^{AoD})$ Delay $\sim \tau$

Table V
LARGE-SCALE AND SMALL-SCALE FADING OF THE MMWAVE STOCHASTIC CHANNEL MODEL. $AoD \sim PDF(\bar{\phi}_{AoA}, \sigma_{AS}^{AoD})$ AND $AoA \sim PDF(\bar{\phi}_{AoD}, \sigma_{AS}^{AoD})$ NOTATIONS REFER TO THE CORRESPONDING PDF OF RANDOM VARIABLES AOD AND AOA AND WITH MEAN ANGLES $\bar{\phi}_{AoD}$ AND $\bar{\phi}_{AoA}$ AND STANDARD DEVIATIONS σ_{AS}^{AoD} AND σ_{AS}^{AoD}. THESE ANGLES CAN THE AZIMUTHAL OR ELEVATION ANGLES.

A more precise channel model describes both the large-scale fading and small-scale fading characteristics shown in Table V. The large-scale fading is caused by the slow variations caused by the surrounding terrain features. In a clustered channel the large-scale fading is constituted by a combination of the AoA spread, AoD spread and delay spread, in addition to the path-loss and shadowing effects. The AoA and AoD spreads represent the variance of the arriving and departing MPCs, respectively, while the delay spread describes the variance of their time delays. On the other hand, small-scale fading is represented by the instantaneous rapid fluctuations of the power level of each MPC and its spatio-temporal characteristics described by the PDFs of the large-scale effects as expressed in Table V.

The path-loss measurements are mainly portrayed in the literature under two scenarios, namely the LOS and NLOS scenarios [77], [103], [110], [182]. In LOS scenarios, the transmitter faces the receiver in an optical line of sight situation, while in NLOS scenarios the optical line of sight between the transmitter and receiver is obstructed. Furthermore, in order to understand the LOS and NLOS scenarios, many papers considered LOS-best and NLOS-best scenarios, where only the highest-power paths are considered.

D. Path Loss and Shadowing

The FSL of Section II describes the LOS propagation of mmWave communications. However, the propagating wave experiences higher attenuations caused by several factors combined, such as the atmospheric attenuation and diffuse reflections. This phenomena is shown in Figure 18, where the difference between the transmitted signal power and the
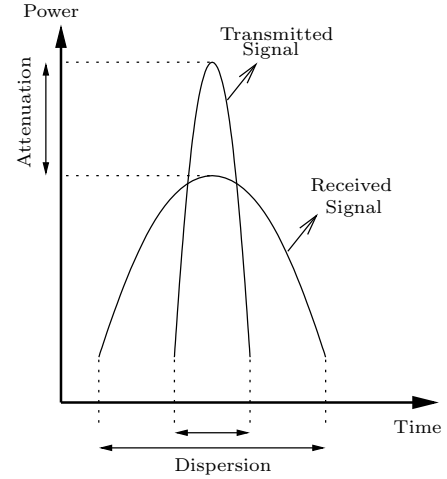

Figure 18. Power attenuation and time dispersion representation of the transmitting signal. The power attenuation is due to path loss and shadowing, while the time dispersion is due to the delay.
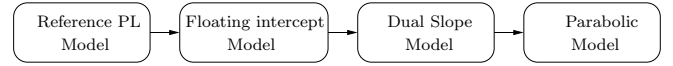

Figure 19. Path loss models considered for mmWaves.

received signal power is caused by the path-loss (PL) and shadowing effects. The transmitted power is often dispensed over a specific time duration owing to the time dispersion. The overall path-loss and shadowing is encapsulated in the large-scale fading model.

Based on the extensive measurements carried out for the 28 GHz, 38 GHz, 60 GHz and 73 GHz frequency bands, many of the path-loss models shown in Figure 19 have been employed in the literature [103]. At the early stages of channel measurements, the main path-loss modeling efforts considered the so-called reference path-loss model [57], [77], [104], [125], [217], [218]. Then, for the sake of better matching the measurements, the modified alpha-beta intercept model used in the 3GPP and WINNER II standards [170], [187] was introduced in [98], [110], [181], [217]. Thereafter, the PL model was extended from a single-slope model to a dual slope model in [77], [103] in order to model the path-loss at distances exceeding the 200 m range. Furthermore, another path-loss model was proposed by Haneda *et al.* in [219] for characterizing the path-loss in outdoor-to-indoor (O2i) scenarios only, where none of the aforementioned models applies. Each of the PL models of Figure 19 were independently used in the projects presented in Table III, which has been detailed in [190].

1) Reference Path Loss Model: The simplest path loss model in Figure 19 used for describing the path-loss and shadowing effects at mmWaves is the reference path-loss model, where the path-loss between the transmit array and the receive array over a distance d (m) and at a given carrier frequency f is given by [57], [104], [125], [217]:

$$PL_{[dB]} = \left[PL_0 + 10 n_p \log\left(\frac{d}{d_0}\right) \right] + S_{\sigma_s}, \quad (12)$$

#	Frequency		LOS		NLOS	
			n_p	σ_s [dB]	n_p	σ_s [dB]
1	28 GHz (Cellular) [57]		2.55	8.66	5.76	9.02
2	28 GHz [104]	V-V	1.1	1.7	2.7	9.6
	Omni.	V-H	4.1	8.0	5.1	10.9
3	38 GHz [39]	$G_{Rx} = 25\,dBi$	2.2	10.3	3.88	14.6
	(Cellular)	$G_{Rx} = 13.3\,dBi$	2.21	9.4	3.18	11
4	60 GHz (Hall) [125]		2.17	0.88	3.01	1.55
5	60 GHz [28]	*Vehicle*	2.66	-	7.17	-
		PTP	2.23	-	4.19	-
6	60 GHz (PTP) [29]		2.25	2	4.22	10.12
7	MiWEBA [189] ($d_0 = 5\,m$)	PL_0 =82.02 dB	-	-	2.36	-
8	60 GHz [220]	*Linear Polarization*	1.92	1.72	-	-
	(Room)	*Circular Polarization*	1.61	1.52	-	-
9	73 GHz [104]	Directional	4.17	9.0	6.4	15.8
	(cross polarization)	Omni.	3.5	6.3	4.6	9.7

Table VI

PATH LOSS EXPONENT FOR 28 GHz, 38 GHz AND 60 GHz, WHERE THE TERM PTP DENOTES PEER-TO-PEER CHANNEL AND G_{Rx} IS THE RECEIVE ANTENNA GAIN.

where d_0 (m) is the free-space reference distance and S_{σ_s} denotes the log-normal shadowing associated with a standard deviation of σ_s. Furthermore, PL_0 indicates the reference free-space loss at distance d_0 and n_p is the path-loss exponent (PLE). This model was also used for the TG3c [14], TGad [216] and MiWEBA [189] models.

Regardless of the shadowing parameter S_{σ_s}, (12) describes the power attenuation of the transmitted signal at distance d with respect to d_0. The path-loss equation of (12) has many extensions. For example, Piersanti *et al.* considered in [205] the associated frequency dependencies, while [217], [220] characterized the small-scale fading effects. On the other hand, the shadowing S_{σ_s} characterizes the power fluctuations around the simple linear representation of the PL imposed by large obstructing objects, such as buildings. The PLE describes the gradient of the path-loss as a fraction of the distance d, and it depends on the specific scenario considered, including the LOS and NLOS scenarios. A LOS link has a lower path-loss in the absence of multipath reflections, which leads to low PLE values. By contrast, the path-loss in an NLOS scenario is significantly higher than in the LOS scenario, since the LOS path between the communicating nodes is obstructed and the received signals are mainly formed by the reflected or scattered MPCs. The value of n_p is empirically obtained from measurements in the different frequency bands and its values in the different mmWave bands are summarized in Table VI. Furthermore, the added gains G_{Tx} and G_{Rx} of the Tx and Rx antennas can be considered in the overall path-loss expression by incorporating these parameters in 12) [221], so it becomes:

$$PL_{[dB]} = \left[PL_0 + 10 n_p \log\left(\frac{d}{d_0} \right) \right] + S_{\sigma_s} + G_{Tx} + G_{Rx}. \quad (13)$$

Alternatively, they can also be added to the small-scale fading model as in [59]. Nonetheless, in order to exploit the directionality of mmWave systems, Maccartney *et al.* introduced in [78] an additional parameter known as the Distance Extension Exponent (DEE), which was used for determining the PL after applying receiver beamforming. The DEE is expressed as

$$DEE = \frac{n_{p_1}}{n_{p_2}}, \quad (14)$$

where n_{p_1} and n_{p_2} are the PLEs of the single-best beam and the combined multi-beam, respectively, given that $n_{p_1} \geq n_{p_2}$. This parameter determines the additional reliable transmit distance by employing beamforming at which a user would experience the lowest PL value. The extra distance covered is defined as

$$d_2 = d_1^{\left(\frac{n_{p_1}}{n_{p_2}} \right)}. \quad (15)$$

For example, by employing multi-beam combining, the maximum transmitter-receiver distance could be extended from 200 m to 448 m. The same technique was applied by Jamsa in [149], where a breaking point scaling factor and a PL offset were used for modifying the PL model.

Furthermore, the depolarization effect of the channel is more hostile at mmWaves [104], since the sparse multipath channel would result in only a few MPCs being detected at the receiver, where polarization mismatch is more likely to occur at mmWaves, which is in contrast to the rich scattering sub 6-GHz bands [222]. The antenna polarization is described by four polarization types, V-V, H-H, V-H and H-V, where H and V refers to the horizontal and vertical polarizations [223]. A mismatch between the antenna polarization configuration and the channel polarization would result in attenuating the re-

ceived power, where the degradation is described by the cross-polarization discrimination (XPD) ratio defining the relationship between both polarization components. For example, it is shown in [104] that the value of the PLE and the shadowing are directly affected by the antenna polarization configurations due to the depolarization effect of the channel [113], where the cross-polarization to co-polarization scenario's XPD ratio ranges between 14 dB and 23 dB. Hence, as recommended in [222], co-polarization configurations should be employed for LOS environments [104], [224].

Detailed values of the best case PLE and best NLOS PLE at the 28 GHz, 38 GHz and 60 GHz frequency bands can be found in [6], [29], [57], [77], [103], [104], [109], [125]. Further values of the path-loss parameters, including their frequency dependency, are discussed in detail in [205] for transmission over multiple channels within the 60 GHz band, such as the 54.78 GHz, 58.38 GHz and 65.38 GHz sub-bands.

The PLE measured in many LOS environments was found to be 2 in numerous studies [7], [28], [37], [57], [75], [217]. Likewise, Rappaport *et al.* recorded in [109] a PLE value of $n_p = 1.89$, which is even lower than that of free space propagation. Hence, the path-loss at short distances can be expressed by the FSL of (1). However, in NLOS communications, where the LOS path is totally blocked by large objects, the PLE has significantly higher values than in the LOS scenarios associated with a minimum of $n_p \geq 3$.

2) Modified Path Loss Model: Another approach for modeling the PL shown in Figure 19 was considered in [110], [217]. Explicitly, these contributions suggested a modification to the reference path-loss equation in order to adapt to the NLOS path-loss measurements acquired. A linear approach is used with a slight modification of (12), which is expressed as:

$$PL_{[dB]} = \alpha_p + 10\beta_p \log(d) + S_{\sigma_s} , \qquad (16)$$

where α_p and β_p accounts for the floating intercept and the linear slope, respectively. In [205], a similar approach to (16) was used by Piersanti *et al.*, where the path-loss model of (12) was employed, but in conjunction with an additional calibration parameter c_p. Moreover, Akdeniz *et al.* reported in [7] LOS values for α_p and β_p at 28 GHz and 73 GHz for cellular communications, where $\beta_p = 2$ and $\sigma_s = 5.8$ are fixed for both cases and $\alpha_p = 61.4$ and $\alpha_p = 59.8$ at 28 GHz and 73 GHz frequency bands, respectively. The main difference of (16) when compared to (12) lies in its ability of manipulating two parameters at a time (α_p and β_p) instead of only one (n_p), which results in higher degrees of freedom in calibrating the model to fit the measured PL values.

Table VII summarizes several measurements recorded for NLOS scenarios. The values of α_p and β_p in Table VII are comparable to the values of n_p and σ_s in Table VI. In fact, they reflect the same path-loss measurements. For example, the values of n_p and σ_s for the 28 GHz frequency band given as 5.76 and 9.02 in row 1 of Table VI, are translated at a specific reference distance d_0 to α_p, β_p and σ_s with values 59.89, 4.51 and 8.52, respectively, shown in row 2 of Table VII. It is also clear that the linear approach reduces the deviation of shadowing by 0.5 dB. Moreover, more values are compared in
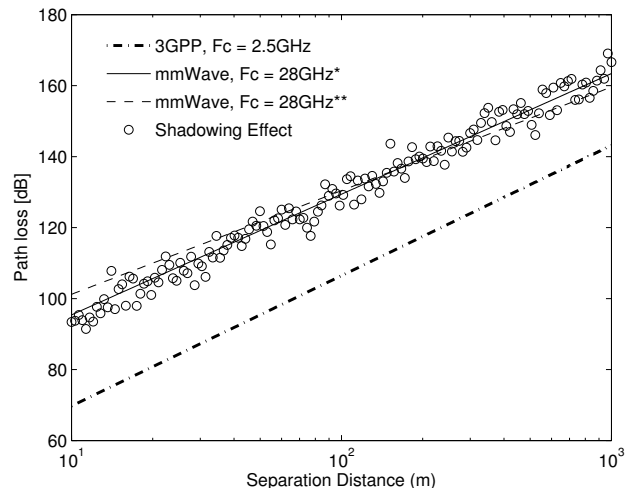

Figure 20. Path loss at the 28 GHz frequency band compared to the 3GPP path loss model at 2.5 GHz carrier frequency. The * symbol refers to the path loss at the 28 GHz band based on (17), with $d_0 = 1\,m$. This curve is surrounded by the path loss values with the lognormal shadowing effects. Furthermore, the ** symbols denote the path loss curve based on (16) with $\beta_p = 2.92$ and $\sigma_s = 72$ as in Table VII.

[217] and it is shown that the shadowing standard deviation can be reduced by up to 6 dB. These values are practical for up to a 200m range, since the regression coefficients are fixed to that distance.

The work in [76], [211] considered the reference PL model, where (12) was slightly modified in order to fit the wideband channel measurements carried out in the 28 GHz band. The path-loss model is then given by [76]:

$$PL_{[dB]} = [61.4 + 34\log_{10}(d)] + S_{\sigma_s} , \qquad (17)$$

where the reference distance is $d_0 = 1\,m$, the PLE is $n_p = 3.4$ and the lognormal shadowing with zero mean has a standard deviation of $\sigma_s = 9.6$ dB.

To realize the effect of the carrier frequency on the path-loss, Figure 20 shows the PL model of the 28 GHz band using (17) denoted by * and (16) denoted by **. Both models are then compared to the 3GPP urban micro (UMi) path-loss model at 2.5 GHz [7], [170]. The figure shows a significant increase in the path-loss when moving up from the 2.5 GHz to the 28 GHz frequency band, with approximately 30 dB to 35 dB difference for distances below 1 km.

3) Dual Slope Path Loss Model: The aforementioned models were used for estimating the PL based on measurements at a transmitter-receiver separation distance of less than or equal to 200 m. However, due to the transmit beamforming and receive beam-combining along with directional antenna deployment, the cell radius is expected to increase from 200 m to 400 m [103]. The PL loss model of the increased-range scenario is determined by extrapolating the measurements taken previously at distances of <200 m using RT. This PL model is referred to as the Dual Slope Path Loss model and

#	Frequency		NLOS		
			α_p	β_p	$\sigma_s\ [dB]$
1	28 GHz [7]		72	2.92	8.7
2	28 GHz [217]	$H_{T_x} = 17m$	59.89	4.51	8.52
	$G_{Rx} = 24.5\,dBi$	$H_{T_x} = 7m$	75.85	3.37	8.36
3	38 GHz [217]	25 dBi, $H_{T_x} = 36m$	127.79	0.45	6.67
		13.3 dBi, $H_{T_x} = 23m$	118.77	0.12	5.78
4	73 GHz [7]		86.6	2.45	8

Table VII
PARAMETERS OF THE PATH LOSS MODEL OF (16), WHERE H_{T_x} DENOTES THE HEIGHT OF THE TRANSMITTER ANTENNA.

Model	Formula	Description
Reference PL	$PL_{[dB]} = \left[PL_0 + 10n_p \log\left(\frac{d}{d_0}\right) \right]$	Calculating the path loss at a specific distance d relies on the reference distance d_0. This model was extensively used in the literature, for example by TG3c [14], TGad [216], MiWEBA [189], NYU [57], [104], [217]and others [125].
Modified Intercept	$PL_{[dB]} = \alpha_p + 10\beta_p \log(d) + S_{\sigma_s}$,	The modified version of the reference modified, which provide two paramters (α_p and β_p) rather than one parameter (n_p). This model was used in the 3GPP and WINNER II standards [170], [187] and was extensively exploited by [98], [110], [181], [217]
Dual-Slope	$PL'_{Dual}(d) = \alpha_p + 10\beta_{p_1} \log(d) + S_{\sigma_s}$ $PL''_{Dual}(d) = PL'_{Dual}(d_{th}) + 10\beta_{p_2} \log(d)$	An extension of the modified intercept model, where the model is extended to include path-loss values at 400 m rather than 200 m by relying on the extrapolation operation [103].
Parabolic	$PL_{[dB]} = \left[10 \cdot \log_{10}\left(A + B \cdot f_c^2\right) \right] + S_{\sigma_s}$,	The parabolic model is specifically exploited for O2i scenarios, where the PL is predominantly determined by the material penetration and propagation mechanisms characteristics of signals in the sub-100 GHz band.

Table VIII
A SUMMARY OF DIFFERENT PL MODELS PRESENTED IN THE LITERATURE.

it is given by [103]:

$$PL'_{Dual}(d) = \alpha_p + 10\beta_{p_1} \log(d) + S_{\sigma_s}, \quad (18)$$
$$PL''_{Dual}(d) = PL'_{Dual}(d_{th}) + 10\beta_{p_2} \log(d), \quad (19)$$

where (18) and (19) are applied for $d \leq d_{th}$ and $d > d_{th}$, respectively, d_{th} is a predefined threshold distance and β_{p_1} as well as β_{p_1} represent the dual slopes. More details on the dual path-loss model may be found in [13].

4) The Parabolic Path Loss Model: A different approach was followed by Haneda *et al.* in [219] in characterizing the path loss of mmWave signals in the sub-100 GHz band in an O2i scenario, where an O2i scenario represents the link between an outdoor base station transmitting to an indoor user. To expound further, the authors argued that the path loss of Figure 4 in Section II, which is predominantly determined by the material penetration and propagation mechanisms characteristics of signals in the sub-100 GHz band, increases quadratically with frequency. Hence, a pair of parameters, A

and B, are used for indicating the parabolic behavior of the PL, which can be expressed as [219]
$$PL_{[dB]} = \underbrace{\left[10 \cdot \log_{10}\left(A + B \cdot f_c^2\right) \right]}_{Parabolic\,form} + S_{\sigma_s}, \quad (20)$$

where the specific values of A and B are shown in Table IX, with the acronyms HLB and LLB representing high loss buildings and low loss buildings, respectively. A summary of the PL models presented in this section is presented in Table VIII

E. Narrow-Band Channel Model

In the early stages of mmWave channel modeling of the 28 , 38 and 72 GHz frequency bands, the narrow-band channel model was considered [7], [82]. This was either due to the lack of wideband measurements owing to the lack of wideband channel sounders, or simply because the wideband parameters were not extracted from theG measurement recorded. In the

Parameter	HLB	LLB
f_c	$< 100\,GHz$	
A	10	5
B	5	0.03

Table IX

narrow-band mmWave channel model, all clusters and MPCs are assumed to arrive simultaneously and all their frequency components over the channel bandwidth are received with the same level of attenuation. In the following we describe the narrow-band mmWave channel model and the effect of the antenna array geometry imposed on it.

1) The Narrow-Band mmWave Channel Model: The multipath channel model is used for characterizing the mmWave channel for both indoor [8], [66], [118], [179] and outdoor [6], [7] environments. The differences between the channel models of these two environments manifest themselves in terms of the specific channel parameters acquired from the measurements. These parameters are encapsulated in the narrow-band channel impulse response portrayed in Figure 21. The corresponding channel matrix $H(t)$ of size $\mathbb{C}^{N_r \times N_t}$ at instant t is given by [7], [8], [63], [69]:

$$H(t) = \frac{1}{\sqrt{N_p}} \sum_{n_{cl}=1}^{N_{cl}} \sum_{p=1}^{N_p(n_{cl})} \rho_{n_{cl}} \alpha_{n_{cl},p}(t)$$
$$\cdot \Omega_{n_{cl},p}^{R_x}\left(\varphi_{n_{cl},p}^{R_x}, \theta_{n_{cl},p}^{R_x}\right)$$
$$\cdot \Omega_{n_{cl},p}^{T_x}\left(\varphi_{n_{cl},p}^{T_x}, \theta_{n_{cl},p}^{T_x}\right)^H, \quad (21)$$

where N_c and $N_p(n_{cl})$ denotes the number of clusters and rays-per-cluster, respectively, which are shown in Figure 21 as *Cluster 1* and *Cluster N_{cl}*. The portion of power represented by each cluster is denoted by $\rho_{n_{cl}}$, while $\alpha_{n_{cl},p}(t)$ represents the instantaneous gain of a MPC. The parameters $\varphi_{n_{cl},p}$ and $\theta_{n_{cl},p}$ are p-th MPC of the n-th cluster's azimuth and elevation angles, respectively, and they characterize the AoD and AoA at the transmitter and receiver. As shown in Figure 21, the AoD and AoA of each cluster are described by their angular spreads (AS) denoted by $\sigma_{\varphi_{n_{cl}}}^{AoA}$ and $\sigma_{\theta_{n_{cl}}}^{AoA}$ for the AoA and by $\sigma_{\varphi_{n_{cl}}}^{AoD}$ and $\sigma_{\theta_{n_{cl}}}^{AoD}$ for the AoD azimuth and elevation angles, respectively. The angular spreads represent the angular distribution of the cluster MPCs around the cluster's central angles $\bar{\theta}_{n_{cl}}^{Tx}$ and $\bar{\varphi}_{n_{cl}}^{Tx}$ at the transmitter and $\bar{\theta}_{n_{cl}}^{Rx}$ and $\bar{\varphi}_{n_{cl}}^{Rx}$ at the receiver. Moreover, $\Omega_{n_{cl},p}$ represents the $(N_t \times 1)$ array factor (AF) of the transmitter antenna array, when superscripted by Tx and it represents an $(N_r \times 1)$ array factor of the receiver antenna array, when superscripted by Rx. The AF vector sizes of the Tx and Rx equals to the number of transmit and receive antennas N_t and N_r, respectively, at each antenna array. The vector $\Omega_{n_{cl},p}$ depends directly on the geometry of the antenna array. The notation $(.)^\dagger$ refers to the Hermitian transpose.

In the narrowband channel model, the channel coefficient at time t is $h_{i,j}(t)$, where i and j are the receive and transmit antenna indices, and it is expressed as:

$$H(t) = \begin{pmatrix} h_{1,1}(t) & h_{1,2}(t) & \cdots & h_{1,N_t}(t) \\ h_{2,1}(t) & h_{2,2}(t) & \ldots & h_{2,N_t}(t) \\ \vdots & \vdots & \ddots & \vdots \\ h_{N_r,1}(t) & h_{N_r,2}(t) & \cdots & h_{N_r,N_t}(t) \end{pmatrix}. \quad (22)$$

The narrow-band channel is considered to be a geometry-dependent model, where the spatial correlation of the rays is affected by the specific geometry of the transmit and receive antenna arrays.

F. The Wideband Channel Model

The aforementioned narrow-band channel model does not reflect an accurate model of the real mmWave scenarios for the following reasons. Firstly, the narrow-band channel is not applicable for large-bandwidth channels, which is the case for all mmWave frequency bands. For example, the measurement campaigns conducted for the 28 GHz and 38 GHz bands in [29], [58], [59], [98], [109] used a null-to-null bandwidth of 800 MHz, while a 1.5 GHz first-RF-stage null-to-null bandwidth was used for the 60 GHz band in [98]. Secondly, the narrow-band channel model cannot fully represent the temporal characteristics of the channel, where the time characteristics of different clusters and MPCs are not distinguishable without representing the delay and the delay-spread in the model. Furthermore, the extensive measurements carried out for the 28 , 38 and 73 GHz bands exhibited multiple time-clusters at the receiver in multiple spatial lobes, which cannot be modeled by a narrow-band channel. They require wideband channel modeling for the accurate representation of their effects, where both the "Spatial" and the "Temporal" avenues of the "Characteristics" roundabout of Figure 2 can be utilized.

To begin with, the temporal characteristics are extracted from the measured power-delay profile (PDP), while the spatial characteristics are produced from the power angle-profile (PAP) measurements [142]. To elaborate further, the temporal characteristics of the channel represent its time-domain parameters, such as the delay spread and the time-of-arrival (ToA), which determine its impulse response, while its spatial characteristics describe the angular characteristics of the channel, such as the angular spread, AoA and AoD.

Generally, the wideband physical channel between the transmitter and receiver is modeled by a tapped-delay lines, which is also known as the double-directional impulse response of the channel [14], [27], [72], [76], [149], [189], [211] characterized by the time and angular characteristics of the channel extracted from channel measurements. In contrast to the narrow-band channel models, in wideband channel modeling the channel can no longer be simply characterized by the steering vectors of the transmit and receive antenna array shapes. In wideband channel modeling, the effect of the transmit and receive AEs is amalgamated with the channel effects in order to form the wideband channel model.

Inspired by the graphical representation of the 60 GHz channel's impulse response (CIR) in [14], the spatio-temporal
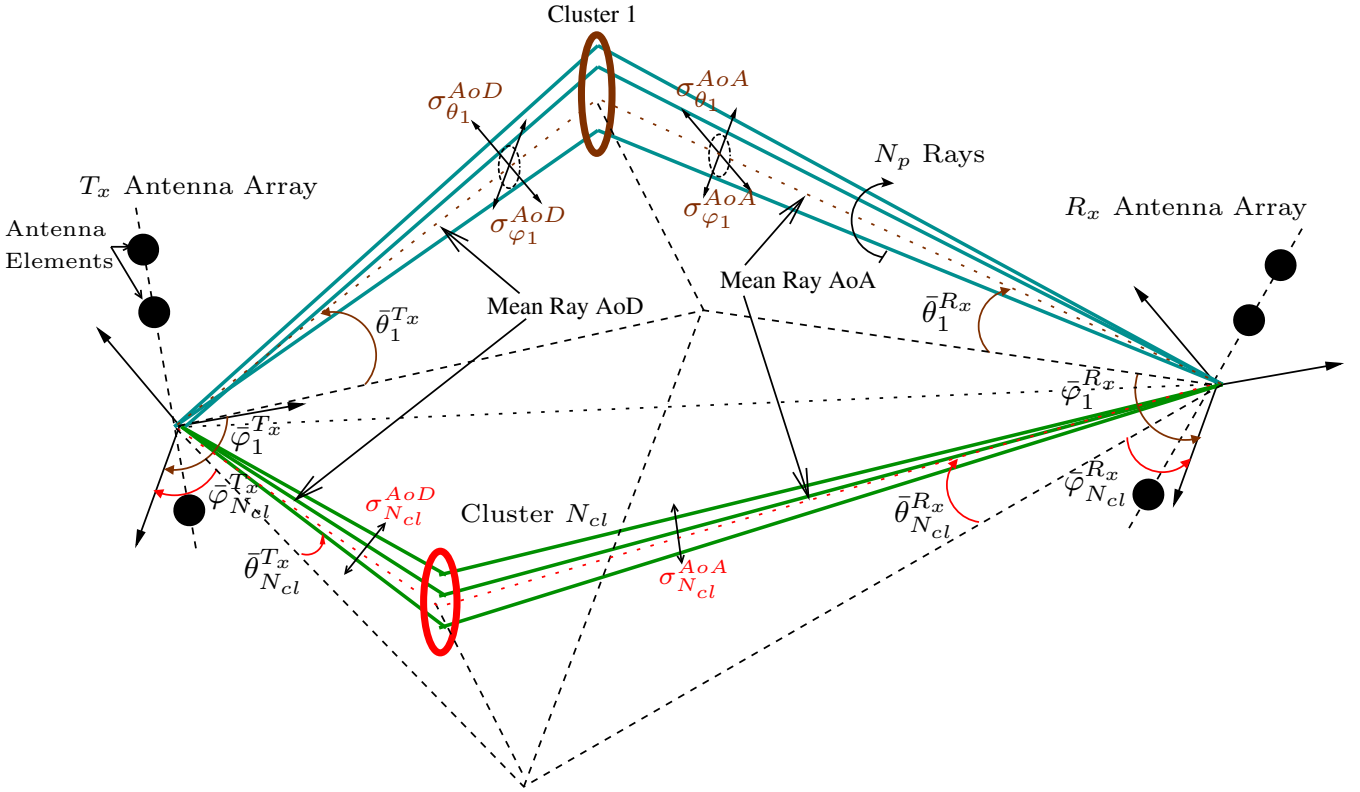
Figure 21. Spatial representation of N_{cl} clustered channel between the Tx and Rx antenna arrays with N_p rays per cluster. This figure shows two clusters, cluster I and cluster N_{cl}. The mean AoA and AoD azimuth angles (φ) and elevation angles (θ) of each cluster, where all other MPCs are distributed around, are defined as $\bar{\varphi}_{n_{cl}}$ and $\bar{\theta}_{n_{cl}}$, respectively. Each cluster has an angular spread of $\sigma_{n_{cl}}^{AoA}$ and $\sigma_{n_{cl}}^{AoD}$ where $n_{cl} = 1, ..., N_{cl}$. This parameter describes how wide a cluster is in term of the angular distribution of MPCs around the mean angle. Here the angle reference is considered to be a fixed Cartesian space with three dimensions. This schematic is based on the 3GPP multipath model in [170]
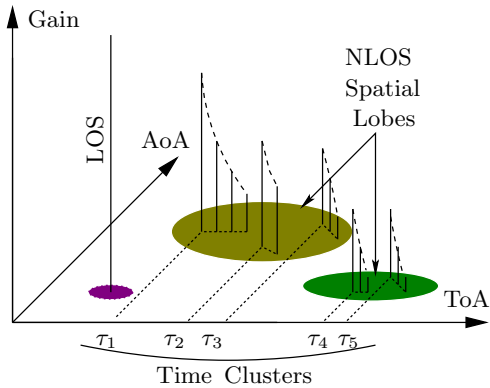

Figure 22. The spatio-temporal representation of the mmWave wideband channel [14].

characteristics of the mmWave channel are represented in Figure 22, where the different MPCs arrive at different time instants. Figure 22 shows three CIR main components, namely a high gain path representing the LOS component and two other low gain NLOS spatial-clusters, where each spatial-cluster has multiple time-clusters, since the different MPCs have different Time-of-Arrivals (ToA), as described by the n-th cluster delay $\tau_{n_{cl}}$ and the AoA characteristics. On the same note, the different measurements conducted at multiple mmWave frequency bands reported that the received PDPs

and PAPs were detected in spatial-clusters and time-clusters [14], [44], [54], [69], [121], [225]. The concept of time-clusters and spatial-clusters was further extended in [72], [76], [79], [80], [105], [211], where multiple received components of a specific time-cluster were observed throughout multiple spatial-clusters, which are also referred to as spatial lobes. More insights on both cluster types will be provided later in what follows.

Samimi and Rappaport distinguished in [76] between a spatial lobe and a time-cluster, where a spatial lobe is defined as a concentration of energy in a specific direction consisting of multiple time-clusters, while a time-cluster is defined as a group of MPCs having diverse spatial. Both the spatial lobe and the time-cluster are shown in Figure 22. Nonetheless, ignoring the lobe definition proposed by Samimi and Rappaport in [76] does not affect the accuracy of the channel model produced, since the power of the spatial lobe is given by the sum of that of its intrinsic time-clusters [6], [7], [226].

1) Indoor Channel Models: Early contributions on wideband channel models conceived for mmWave systems were limited to the 60 GHz channel model of the WPAN [14] and WLAN [27] indoor systems. An accurate wideband channel model requires numerous parameters for characterizing the channel, whilst the channel model described in (21) is a narrow-band one, which only describes the spatial characteristics of the mmWave channel. In order to extend this

channel model to a wideband model, its delay-profile also has to be characterized [7], [45], [125], [176], [206]. For instance, instead of being exclusively specified in terms of θ, φ, t and the angular spread shown in Figure 23, the channel impulse response should be extended to include the temporal characteristics of the channel represented by the delay τ.
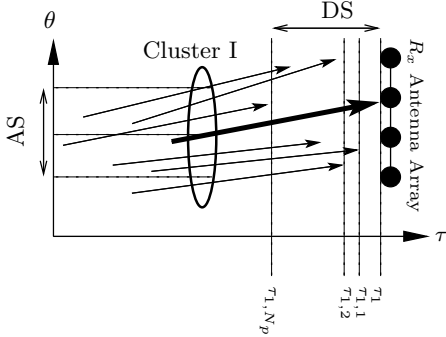

Figure 23. Spatio-temporal cluster representation with both AS and DS. The cluster's time delay is τ_1 and each ray p has a delay of $\tau_{1,p}$ with $1 \leq p \leq N_p$.

As shown in Figures 22 and 23, cluster I has a cluster delay of τ_1, while its p-th ray arrives with a delay of $\tau_{1,p}$ within a cluster's delay spread (DS). The cluster delay can be considered as the delay of the first arriving MPC and the other MPCs' delay succeeding it, where each channel tap delay can be expressed as $\delta\left(t - \tau_{n_{cl}} - \tau_{n_{cl},p}\right)$ [14], [44], [69].

Furthermore, the 60 GHz channel model in [69] presented a double-directional channel model reflecting both the spatial and temporal characteristics, which was also compared to the IEEE802.11ad and 802.153c models. The spatio-temporal characteristics of the 60 GHz channel were also studied in [14], [28], [66], [69], [120], [121], [125], [142], [166], [175], [206], where the model of the indoor 60 GHz channel is based on the TSV [67] and on the extended-SV [171], [172] channel models. The general double-directional wideband CIR is given by:

$$
\begin{aligned}
h\left(t, \theta, \varphi\right) = {} & \beta_{LOS}\delta\left(t, \theta, \varphi\right) + \sum_{n_{cl}=1}^{N_{cl}} \sum_{p=1}^{N_p} \alpha_{n_{cl},p} \\
& .\delta\left(\phi_{Rx} - \Theta_{n_{cl}}^{Rx} - \omega_{n_{cl},p}^{Rx}\right) \\
& .\delta\left(\phi_{Tx} - \Theta_{n_{cl}}^{Tx} - \omega_{n_{cl},p}^{Tx}\right) \\
& .\delta\left(t - \tau_{n_{cl}} - \tau_{n_{cl},p}\right),
\end{aligned} \tag{23}
$$

where β_{LOS} denotes the LOS component weight, $\delta(.)$ stands for the Dirac delta function and the parameters ϕ, $\Theta_{n_{cl}}$ and $\omega_{n_{cl},p}$ are the AoA or AoD (subscripted with Rx or Tx), the n_{cl}-th cluster central angle and the angle of the p-th ray in the n_{cl}-th cluster, respectively.

To elaborate further, the IEEE 802.15.3c WPAN channel model of [14] includes the LOS component and considers only the spatio-temporal characteristics of the arriving clusters, captured in terms of the AOA, while the IEEE 802.11ad WLAN channel model of [27] did not consider the LOS component ($\beta_{LOS} = 0$), but extended the model to include

both the AoA and AoD at both ends of the link over both the azimuthal and elevation angles. Moreover, the WLAN channel model features non-stationary scenarios of pedestrian speeds and it also included the polarization effect of both the transmit an receive antennas. The channel model TGad [27] is expressed as:

$$
h\left(t, \theta, \varphi\right) = \sum_{n_{cl}=0}^{N_{cl}} \sum_{p=-M_b}^{N_p} \alpha_{n_{cl}}\beta_p\delta\left(t - \tau_{n_{cl}} - \tau_{n_{cl},p}\right), \tag{24}
$$

where M_b and N_p represent the total number of MPCs[7].

The TG3c WPAN channel model was specifically based on the extended-SV, where clusters are defined in both the time and angular domain. Furthermore, it assumes all independent uniform distribution of the clusters' AoA combined with a Gaussian distribution of its specific MPCs' AoA within each cluster, where the clusters delay and MPCs delays are represented by Poissonian processes.

For the indoor WPAN and WLAN systems [14], [27], [69], [216], the modulus of the complex gain of the p-th ray in the n-th cluster is described by the cluster arrival time $T_{n_{cl}}$, $\Gamma_{n_{cl}}$, $\tau_{n_{cl},p}$ as well as by the ray decay Γ_r and it is typically expressed as $\left|\alpha_{n_{cl},p}\right|^2 = \xi_0 e^{\frac{-T_{n_{cl}}}{\Gamma_{n_{cl}}}} e^{\frac{-\tau_{n_{cl},p}}{\Gamma_r}}$ with its argument obeying $\arg\left(\alpha_{n_{cl},p}\right) \sim U\left[0, 2\pi\right]$, where ξ_0 is the average power of the first ray in the first cluster. The main difference between the WPAN and WLAN complex gain values is that the latter uses a two-sided cluster decay model instead of using a single-decay cluster model and separately takes into account the ray decay Γ_r for both post-cursor and pre-cursor rays, where the ray parameter $\left|\alpha_{n_{cl},p}\right|^2$ of both ray types is modified to $e^{\frac{-\tau_{n_{cl},p}}{\Gamma_r}}$ and $e^{\frac{\tau_{n_{cl},p}}{\Gamma_r}}$, respectively. Additionally, more insights concerning the LOS component β_{LOS} are reported in [14], [67] for WPAN networks, where it is only affected by the direct LOS path attenuation and it is expressed in terms of the Tx and Rx antenna gains, the separation distance and height, the PL and the angle of incidence at the receiver.

Owing to the fact that all channel measurement campaigns depend on the antenna setup and its radiation pattern [66], [165], considering directional antennas for mmWaves communications implies that the channel between the communicating nodes is dominated by the specific paths that fall within the antennas beamwidths. For example, the outdoor measurements carried out for mobile broadband at 28 GHz and 38 GHz in [59], [63] used a 24.5 dBi-gain directional antenna with a 10° narrow beamwidth. Similarly, Geng *et al.* used in [125] two types of antennas, namely a directional horn and and omnidirectional biconical antenna associated with 22.7 dB and 5 dB gains, respectively. Hence, the parameters extracted for a wideband channel already include the effect of antennas.

More recently, Haneda *et al.* extended in [54] the channel model of an indoor scenario associated with a maximum range of 11 m by including multiple indoor scenarios based on their

[7]In the TGad channel model [216], each cluster is modeled by a two-sided exponential decay rather than the single-sided decay used by TG3c [14]. Hence, MPCs at both sides of the cluster are represented by M_b and N_p.

own measurement campaigns for transmission over the 60 GHz and 70 GHz bands. The channel transfer function $H(f)$ of [54] is expressed as:

$$
\begin{aligned}
H(f) = {} & G_{Tot}e^{-j2\pi f\tau_0} \\
& + \sum_p \alpha_p G_P\left(\phi_p^{Rx}\right) e^{-j2\pi f\tau_p} \\
& + \sum_{p'} \alpha_{p'} e^{-j2\pi f\tau_{p'}}, \qquad (25)
\end{aligned}
$$

where G_{Tot} encapsulates the effect of antenna gain, τ_0 is the LOS delay, α_p denotes the multipath tap gain, with τ_p being the associated delay. Similarly, the NLOS multipath tap gains and delays are indicated by the index p'.

2) Improved Wideband mmWave Channel Models: Based on wideband measurements over the 28, 38, 60 GHz and 73 Ghz frequency bands, wideband channel model were developed in [72], [76], [98], [211] for NLOS dense outdoor urban scenarios. The proposed channel was referred to as the ultra-wide band (UWB) mmWave channel model. A channel is considered to be an UWB channel either when its -10 dB-down bandwidth exceeds 500 MHz or when the bandwidth to carrier frequency ratio, which is known as the fractional bandwidth, is above the 0.2 threshold [227]. Due to the substantial bandwidth available at mmWave frequencies, where at least a minimum of 1 GHz of bandwidth can be identified, the UWB concept was introduced also to the mmWave technology.

The wideband channel model proposed in [59], [72], [76], [79], [80], [105] can be described by a double-directional CIR of the amalgamated MPCs based on the 3GPP model and it is given by:

$$
\begin{aligned}
h(t,\tau,\theta,\varphi) = {} & \sum_{n_{cl}=1}^{N_{cl}} \sum_{n_p=1}^{N_p(n_{cl})} \alpha_{n_{cl},n_p} \\
& \delta\left(\varphi - \bar{\varphi}_{n_{cl}}^{Rx} - \varphi_{n_{cl},n_p}^{Rx}\right) \\
& \delta\left(\theta - \bar{\theta}_{n_{cl}}^{Rx} - \theta_{n_{cl},n_p}^{Rx}\right) \\
& \delta\left(\varphi - \bar{\varphi}_{n_{cl}}^{Tx} - \varphi_{n_{cl},n_p}^{Tx}\right) \\
& \delta\left(\theta - \bar{\theta}_{n_{cl}}^{Tx} - \theta_{n_{cl},n_p}^{Tx}\right) \\
& \delta\left(t - \tau_{n_{cl}} - \tau_{n_{cl},n_p}\right), \qquad (26)
\end{aligned}
$$

where α_{n_{cl},n_p} is the complex gain of the n_p-*th* MPC in the n_{cl}-*th* cluster. Both $(\varphi_{n_{cl},n_p}^{Tx}, \theta_{n_{cl},n_p}^{Tx})$ and $(\varphi_{n_{cl},n_p}^{Rx}, \theta_{n_{cl},n_p}^{Rx})$ characterize the (azimuth, elevation) AoD and AoA at the transmitter and receiver, respectively, and $(\bar{\varphi}_{n_{cl}}^{Tx}, \bar{\theta}_{n_{cl}}^{Tx})$ and $(\bar{\varphi}_{n_{cl}}^{Rx}, \bar{\theta}_{n_{cl}}^{Rx})$ are the mean cluster angles of the above AoD and AoA. The parameter τ_{n_{cl},n_p} denotes the delay of the n_p-*th* mutlipath in the n_{cl}-*th* cluster and $\tau_{n_{cl}}$ is the n_{cl}-*th* cluster delay. The elevation dimension was not considered in [76], but it was later included in the 3D channel models in [79], [98], [105], [211]. The AoD and AoA of each MPC are described by the mean cluster angles $(\bar{\varphi}_{n_{cl}}, \bar{\theta}_{n_{cl}})$ and by the angular spreads (AS) of the clusters denoted by $\sigma_{n_{cl}}^{AoA}$ and $\sigma_{n_{cl}}^{AoD}$ [57]. This channel model was also adopted by the MiWEBA project of Table III and its parameters can be found in [189].

Samimi and Rappaport considered in [76], [211] the effect of directional antennas in the path-loss model, while in [80], [105] the effect of the directional Tx and Rx antennas was also incorporated in the CIR. Moreover, the effect of antenna polarization on both LOS and NLOS scenarios was studied in [72], [79], [80], [98], [105]. In these works, the measured instantaneous MPC gain was reported to have a Rician distribution with a K-factor ranging from 3 to 15 in LOS environments and 3 to 8 in NLOS environments, given a specific Tx-Rx polarization. Hence, the channel model was appropriately modified to fit their measured data [105]. Furthermore, in order to characterize the spatial correlation amongst the closely packed AEs (e.g. $<\lambda$) at the Tx and Rx, a correlation-based channel model was advocated in [79], [80], [105], where the correlation parameters were based on channel measurements. Each MPC in (11) can now be expressed as [79]:

$$
H_{n_{cl},p} = R_r^{1/2} H_G R_t^{1/2}, \qquad (27)
$$

where $R_r^{1/2} \in \mathbb{C}^{N_r \times N_r}$ and $R_t^{1/2} \in \mathbb{C}^{N_t \times N_t}$ are the measurement-based receive and transmit spatial-correlation matrices, while H_G represents the Rayleigh/Rician distribution.

In a nutshell, all channel characteristics are divided into two parts, the spatial-clusters and the time-clusters, which are jointly referred to as the spatio-temporal characteristics of the channel.

G. Spatio-Temporal Characteristics

Here we summarise the main spatio-temporal characteristics of the mmWave channel. A cluster can be defined as a group of similar-delay MPCs, or rays, sharing similar characteristics, provided that they can be differentiated from one cluster to another. The clusters are distinguished by their spatial and temporal characteristics [7], [170], [171]. These characteristics include the mean AoA and AoD angles, angular spreads, delay, root mean square (RMS) delay spread, the number of sub-rays associated with each cluster and the total power of rays in each cluster [59]. The cluster-characteristics can be further sub-divided into two groups: inter-cluster and intra-cluster characteristics. The former includes the general cluster characteristics, such as the cluster's decay rate, arrival rate, angular spread and shadowing features, while the latter includes the rays' characteristics, such as the ray's AoA/AoD and arrival time [59], [69], [216].

The cluster characteristics rely on the measurements recorded for the different bands within the mmWave spectrum. As shown in Table I several studies covered the clusters' statistical characteristics in the different frequency bands [6], [46], [63], [67], [69], [125], [176], [205], [216]. The most rich measurements in the literature are those related to the 60 GHz band [69], [125], [142], [205]. The spatio-temporal characteristics recorded at 60 GHz are discussed in detail in [142] for diverse scenarios, such as hallways, room to room communications etc. The inter-cluster and intra-cluster parameters recorded for a living room were presented in [216]. In the following, we will discuss the cluster characteristics, including the number

Frequency		N_{cl}
28 GHz (Narrow-band) [7]		$N_{cl} = max\left\{Pois\left(\lambda_p\right), 1\right\}, \lambda_P = 1.8$
28 GHz (LMDS) [61]		3 maximum PDPs
38 GHz [63]		$N_{cl} = 2$
60 GHz [125] ($N_{cl} = 1$)	Corridor	$N_p = Exp\left(\lambda_{Exp}\right) + Pois\left(\lambda_p\right)$ $\lambda_{Exp} = 1.5$, $\lambda_P = 2.2$, and $N_p \leq 13$
	LOS Hall	$N_p = Pois\left(\lambda_p\right), \lambda_P = 10$ and $N_p = \leq 17$
60 GHz [69] (indoor)	LOS	$N_{cl} = 6 \rightarrow 12$ or $Pois\left(\lambda_p\right), \lambda_P = 10$
	NLOS	$N_{cl} = 8 \rightarrow 12$ or $Pois\left(\lambda_p\right), \lambda_P = 10$
60 GHz (WPAN) [14]		$N_{cl} = Pois\left(\lambda_p\right), \lambda_P = 9$
60 GHz (WLAN) [27]		$N_{cl} = Pois\left(\lambda_p\right), \lambda_P = 18$
60 GHz (Library) [120]		$N_{cl} = 1$
73 GHz (Cellular) [7] Narrow-band		$N_{cl} = max\left\{Pois\left(\lambda_p\right), 1\right\}$ $\lambda_P = 1.9$

Table X
NUMBER OF CLUSTERS AT 28 GHz, 38 GHz, 60 GHz AND 73 GHz. THE NOTATION $Pois\left(\lambda_p\right)$ REFERS TO THE POISSON DISTRIBUTION OF THE NUMBER OF CLUSTER WITH VARIANCE λ_p. THE *max* OPERATION IS ADDED TO INSURE THAT THE SYSTEM WILL HAVE AT LEAST *1* CLUSTER AT A TIME. THE NOTATION $Exp\left(\lambda_{Exp}\right)$ REFERS TO THE EXPONENTIAL DISTRIBUTION WITH MEAN λ_{Exp}.

of clusters and rays, the angular and temporal characteristics as well as the power per cluster.

- *Number of Clusters and Rays:* The number of clusters represents the number of PDP peaks. The number of clusters in mmWaves is typically modeled by a Poisson distribution with variance λ_P and it is expressed as $N_{cl} \sim Pois(\lambda_p)$, where λ_P varies according to the scenario and operating frequency [7], [14], [27], [69], [109], [125]. Moreover, the authors of [45], [46] used the six-ray channel model for LOS communications, where in addition to the direct LOS link, five reflected rays were considered. Different measurement results on the number of clusters are shown in Table X, where the number of rays in each cluster varies according to the specific scenario used. For example, Akdeniz *et al.* followed in [7] the 3GPP standard and conceived 30 rays-per-cluster, while Geng *et al.* reported in [125] only the number of MPCs, which suggests that only one cluster is considered, where the number of MPCs N_p is realized, as mentioned in Table X. Moreover, the authors of [14] considered the arrival rate of rays in each cluster, which was exponentially distributed with mean of $\lambda_R^{-1} = 0.820$ instead of assuming a fixed number of rays. However, the authors of [27], [69] used $M_b = 8$ and $N_p = 6$ in their approach for the TGad channel model.
- *Angular Characteristics*: The AoA and AoD of multi-path clusters and rays are characterized by their angular spreads $\sigma_{n_{cl}}^{AOA}$ and $\sigma_{n_{cl}}^{AOD}$ with $n_{cl} = 1, ..., N_{cl}$ at the receive and transmit antenna arrays, respectively. The angular spreads found for different mmWave frequency

bands are shown in Table XI. The central angles of all clusters are generated uniformly between 0 and 2π. Then, the rays of each cluster are generated according to the distribution of the AoA or AoD and their angular spread. For example, at 28 GHz featured in the first row of Table XI, one can uniformly generate the mean AoD, $\bar{\varphi}^{AoD} \sim U\left[0, 2\pi\right]$, while the specific rays within the same cluster can be exponentially distributed (*Exp*) with a mean of $\bar{\varphi}^{AoD}$ and standard deviation of $\sigma_\varphi^{AoD} \sim Exp(10.2°)$. Similarly, observe for 60 GHz in row 2 that after generating a uniform distribution (U) with a mean AoD obeying $\bar{\varphi}^{AoD} \sim U\left[0, 2\pi\right]$, the rays within this cluster will be distributed around that mean angle by obeying a Laplacian distribution of $\sigma_\varphi^{AoA} = 22.2$ spread in NLOS office scenario. More recently, Samimi and Rappaport generated in [72], [211] the mean AoD and AoA spatial lobes based on a uniform distribution for the azimuth angles and with a normal distribution for the elevation angles. In both of these contributions the MPCs have a normally distributed AoD and a a Laplacian AoA distribution.

- *Temporal Characteristics*: The root mean square RMS delay spread σ_τ, which is also referred to here simply as delay spread (DS), is based on the delay of all rays within each cluster. It is the most salient statistical parameter used for characterizing the time dispersion, as illustrated in Figures 18 and 23. It also indicates the time difference between the first and last MPCs. The delay spread of the 60 GHz frequency band was studied in [14], [27],

Frequency		Azimuthal AS	Elevation AS	Generate Angles
28 GHz [7] σ is Exponentially distributed with mean λ_{Exp}^{-1}		σ_{φ}^{AoD}, $\lambda_{Exp}^{-1} = 10.2°$	σ_{θ}^{AoD}, $\lambda_{Exp}^{-1} = 0°$	$\varphi^{AoD} \sim \mathcal{N}(\bar{\varphi}^{AoD}, \sigma_{\varphi}^{AoD})$, $\theta^{AoD} \sim \mathcal{N}(\bar{\theta}^{AoD}, \sigma_{\theta}^{AoD})$
		σ_{φ}^{AoA}, $\lambda_{Exp}^{-1} = 15.5°$	σ_{θ}^{AoA}, $\lambda_{Exp}^{-1} = 6°$	$\varphi^{AoA} \sim \mathcal{N}(\bar{\varphi}^{AoA}, \sigma_{\varphi}^{AoA})$, $\theta^{AoD} \sim \mathcal{N}(\bar{\theta}^{AoD}, \sigma_{\theta}^{AoD})$
60 GHz [14] Only AoA horizontal is considered	CM1.4	$\sigma_{\varphi}^{AoA} = 107°$	-	$\varphi \sim Lap(\bar{\varphi}^{AoA}, \sigma_{\varphi}^{AoA})$
	CM4.2	$\sigma_{\varphi}^{AoA} = 22.2°$	-	//
	CM7.2	$\sigma_{\varphi}^{AoA} = 38.1°$	-	//
	CM9	$\sigma_{\varphi}^{AoA} = 45.8°$	-	//
60 GHz [66]		$\sigma_{\varphi}^{AoA} = 14.5°$	-	//
73 GHz [7] σ is Exponentially distributed with mean λ_{Exp}^{-1}		σ_{φ}^{AoD}, $\lambda_{Exp}^{-1} = 10.5°$	σ_{θ}^{AoD}, $\lambda_{Exp}^{-1} = 0°$	$\varphi^{AoD} \sim \mathcal{N}(\bar{\varphi}^{AoD}, \sigma_{\varphi}^{AoD})$, $\theta^{AoD} \sim \mathcal{N}(\bar{\theta}^{AoD}, \sigma_{\theta}^{AoD})$
		σ_{φ}^{AoA}, $\lambda_{Exp}^{-1} = 15.4°$	σ_{θ}^{AoA}, $\lambda_{Exp}^{-1} = 3.5°$	$\varphi^{AoA} \sim \mathcal{N}(\bar{\varphi}^{AoA}, \sigma_{\varphi}^{AoA})$, $\theta^{AoD} \sim \mathcal{N}(\bar{\theta}^{AoD}, \sigma_{\theta}^{AoD})$

Table XI

THE CLUSTER'S AoA AND AoD ANGULAR SPREADS IN THE 28, 60 AND 73 GHZ BANDS. THE NOTATIONS $\mathcal{N}(\bar{\theta}, \sigma)$ AND $Lap(\bar{\varphi}, \sigma)$ REFERS TO THE NORMAL DISTRIBUTION AND AND LAPLACIAN DISTRIBUTION WITH MEAN $\bar{\theta}$ AND STANDARD DEVIATION σ, RESPECTIVELY. THE ACRONYMS CM1.4, CM4.2, CM7.2 AND CM9 REFERS TO THE IEEE802.15.3C SCENARIOS [14]. THE // NOTATION IS USED TO AVOID REDUNDANCY OF THE PREVIOUS ROW VALUE.

[44], [66], [67], [125], [142], [179], [216], demonstrating that the delay spread is on the order of a few nanoseconds, as shown in Table XII. In [66], Choi *et al.* assumed to have a negative-exponential distribution of $\frac{1}{\sigma_{\tau}} e^{-\lambda_{\tau} \frac{\tau}{\sigma_{\tau}}}$, with a fitting parameter of $\lambda_{\tau} = 3$ used for accurately matching the negative-exponential distribution to the corresponding measurements. In [61] Soma *et al.* classified the channel into three categories shown in Table XII: hostile, moderate and benign, according to the environment's blockage. It is then shown that at the LMDS band sites associated with more hostile blockage have longer delay spreads. Furthermore, as expected, the NLOS delay spreads in Table XII are observed to be longer than those of the LOS scenarios, since the LOS components arrive with a reduced delay owing to their shortest paths. At 38 GHz, it was reported by Rappaport *et al.* in [39] that the DS at a fixed location is improved, as the directivity of the antennas increases, which is indeed expected due to excluding the long-delay path arriving from wide angles. Here, the authors added that the DS is less than 20 ns for more than 80% of the NLOS cases. Upon considering the relationship between the PL and σ_{τ}, at 60 GHz it was found by Geng *et al.* in [44] that the DS σ_{τ} is exponentially proportional to the path-loss PL, which is formulated as $\sigma_{\tau} \sim e^{PL}$, whilst at 28 GHz their relation is found to be linear by Soma *et al.* in [61], obeying $\sigma_{\tau[ns]} = c_1 + c_2 PL_{[dB]}$, where c_1 and c_2 are constants that represent their linear relation.

- Cluster Power: The power term $\rho_{n_{cl}}$ in (21) represents the specific portion of the total power P_t assigned to each cluster. The cluster-power generally represents the received power of the n_{cl}-th cluster, which changes

Frequency		σ_{τ}(ns)
28 GHz [61] (LMDS) (Model 2)	Hostile	14.61
	Moderate	50.89
	Benign	75.85
28 GHz [57] (Cellular)	KAU-11	203.1
	COL1-5	163
38 GHz [39] Outdoor Urban Cellular	$G_{R_x} = 13.3$ dBi	*mean max* (10.1,166)
	$G_{R_x} = 25$ dBi	*mean max* (13.5,185)
38 GHz [29] maximums NLOS	peer-to-peer	122
	Cellular	117
60 GHz [14]	Simulated	7.9
	Experimental	10.6
60 GHz [66]		7
60 GHz [44] (Hall)	LOS	16
	NLOS	22

Table XII

RMS DELAY SPREAD VALUES OF 28 GHZ, 38 GHZ AND 60 GHZ FREQUENCY BANDS. THE MEAN AND MAX VALUES OF THE THIRD ENTRY ARE EXPRESSED AS (MEAN σ_{τ}, MAXIMUM NLOS). KAU-11 AND COL1-5 REFERS TO THE MEASUREMENT LOCATIONS REPORTED IN [57] AT KAUFMAN BUSINESS SCHOOL (17M HIGH ABOVE GROUND LEVEL) AND COLES RECREATIONAL CENTER (7M HIGH ABOVE GROUND LEVEL), RESPECTIVELY.

relatively slowly over time. In mmWaves systems, the per-cluster power decays with the cluster delay $\tau_{n_{cl}}$, which was characterized by a certain cluster decay factor Γ_c in [7], [14], [142], [171], [176], [216]. Ayach *et al.* used in [8] equal power distribution for all clusters associated with $\rho_{n_{cl}} = \sqrt{\frac{P_t}{N_{cl}}}$ under having a unity power of $P_t = 1$. On the other hand, at 28 GHz and 73 GHz, Akdeniz *et al.* followed in [7] the power

generation technique of 3GPP [170], where the cluster-power depends on the delay distribution and shadowing effects: characterized by $\rho_{n_{cl}} = \underbrace{e^{-\tau_{n_{cl}} \frac{r_\tau - 1}{r_\tau \sigma_\tau}}}_{1} . \underbrace{10^{\frac{-Z_{n_{cl}}}{10}}}_{2}$, where the first term represents the received power of the cluster at delay $\tau_{n_{cl}}$, σ_τ is the DS and the delay distribution has a proportionality constant of r_τ, while the second multiplicative term represents the shadowing effect, and the path-loss is included in the channel gain.

The parameter $\alpha_{n_{cl},p}(t)$ of the p-th ray in the n_{cl}-th cluster of (21) represents the rapidly-fluctuating small-scale fading in terms of its instantaneous complex gain and its expression reflects both the operating frequency and the propagation environment. For example, Akdeniz *et al.* followed in [7] the 3GPP model, where the value of the large-scale fading parameter $\rho_{n_{cl}}$ is considered in the PL that in turn is used for characterizing the complex gain formulated as $\alpha_{n_{cl},p}(t) = \bar{\alpha}_{n_{cl},p}e^{j2\pi f_d cos(w_{n_{cl},p})t}$. The instantaneous complex gain $\bar{\alpha}_{n_{cl},p}$ is defined as a random variable with a normal distribution $N_{\mathbb{C}} \sim (0, \rho_{n_{cl}}10^{-0.1PL})$, and f_d is the maximum Doppler shift due to the communicating nodes' mobility and $w_{n_{cl},p}$ is the AoA of ray p in cluster n_{cl} with respect to the direction of movement. Furthermore, the general complex gain of the specific cluster n_{cl} of the N_{cl} clusters is reported by Rangan *et al.* in [82] without separately considering each ray's characteristics and the channel response is expressed as $h(t) = \sum_{n_{cl}}^{N_{cl}} \alpha_{n_{cl}}(t)e^{j2\pi f_d cos(\bar{\phi}_{n_{cl}})t}$, where $\alpha_{n_{cl}}(t)$ is the slow gain variation of cluster n_{cl}, while $\bar{\phi}_{n_{cl}}$ is the cluster's mean AoA. The authors of [82] justified the slow varying nature of $\alpha_{n_{cl}}(t)$ by reporting that the angular spread of all the clusters is typically small and varies slowly with time.

In a nutshell, the above spatio-temporal characteristics extracted from channel measurements or from extensive RT simulations depend on the specific mmWave frequency band. In order to rely on these characteristics, multiple factors should be taken into consideration. Furthermore, these mmWave systems exhibit different design requirements from those of classic low-frequency wireless systems owing to their high attenuation and sparse scattering nature. Both of these concerns are discussed in the following section, with a view to assist system designers in their efforts.

IV. Design Guidelines

In this section we present the main requirements to be satisfied for constructing a mmWave channel model, followed by the architecture
of mmWave systems. Then we discuss the associated system architecture and antenna design considerations in mmWave communications, followed by the link budget analysis of a mmWave network.

A. Channel Model Considerations

The channel effects were resembled to the specific symptoms of a disease in [228], where understanding the symptoms, namely the propagation characteristics leads to an effective treatment and a high-integrity communication system. Likewise, at mmWaves understanding the channel characteristics

and recognizing their differences with respect to the lower frequency bands is essential for a successful system design. The propagation characteristics of mmWaves were discussed in Sections II and III, where the key observation was that we experience a sparse CIR and a high attenuation. Hence, any future system should be designed by taking into consideration these limitations.
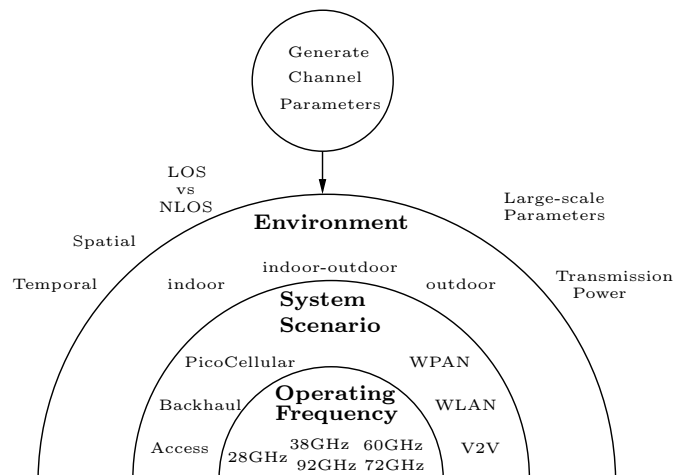
Figure 24. Design considerations for mmWave channel models.

In order to simulate a mmWave system operating in a given frequency band, rigorous measurements of the different channel characteristics should be taken into account by the channel model. As shown in Figure 24, creating the mmWave simulation channel depends on three key points:

- *Identify the system* environment: The building blocks of a mmWave system commences with identifying the system's nature, such as an indoor system (e.g. WPAN, WLAN), outdoor system (e.g. cellular, D2D) and indoor-outdoor system (e.g. WLAN-cellular interface), etc.
- *Distinguish the simulated scenario*: For example, an indoor scenario could be a WLAN, WPAN or indoor festival, while an outdoor system could be a UMi, UMa or backhaul.
- *The operating frequency*: This is the most important parameter, since the propagation characteristics differ from one frequency band to another even within the mmWave spectrum.

The availability of channel parameters extracted from extensive measurement campaigns is essential in order to carefully characterize a specific system. Based on these system settings, the channel model may be constructed according to the chosen scenario. The spatial and temporal characteristics that represent the large-scale and small-scale fading attributes for both LOS and NLOS environments are widely available for diverse frequency bands, such as the 28 GHz, 38 GHz, 60 GHz and 72 GHz bands.

To elaborate a little further, the steps towards constructing the mmWave channel model used in this thesis are presented in Figure 25, which is based on the 3GPP channel model generation detailed in [7], [170], [211]. Each of the
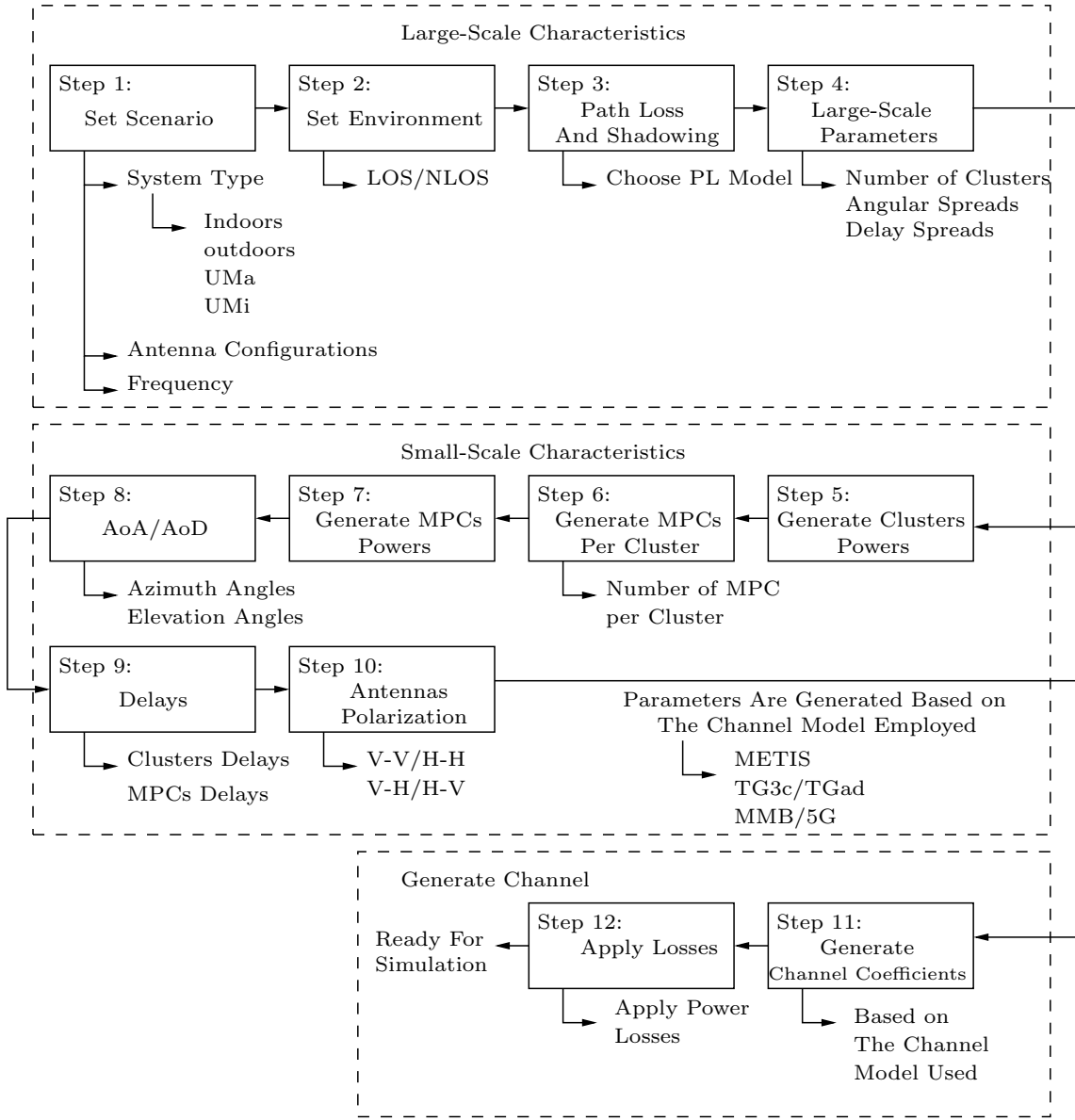
Figure 25. Steps needed to generate the mmWave channel model. The acronyms used in this figure are defined as follows. Urban Macro (UMa); Urban Micro (UMi); Line-of-Sight (LOS); Non-Line-of-Sight (NLOS); Path Loss (PL); MPCs; Angle-of-Arrival (AoA); Angle-of-Departure (AoD); Vertical (V) and Horizontal (H) Polarization; Mobile and wireless communications Enablers for the Twenty-twenty Information Society (METIS) project; Task Group 3c (TG3c); TASK Group ad (TGad); Mobile Broadband (MMB).

channel models proposed in Section III-A have their unique construction steps. As shown in Table V, the propagation characteristics are described by two key parameter sets, the large-scale fading and the small-scale fading. The steps to be followed for generating the mmWave channel model based on both fading types are presented in Figure 25. The first building block of generating any channel model is represented in Step 1, where it is essential to identify the indoor or outdoor scenario type, the operating frequency (e.g. 28 GHz, 38 GHz, 60 GHz and 72 GHz) as well as the transmitter and receiver antenna's configurations (e.g. directionality and polarization). Next, in Step 2 the LOS or NLOS environment is decided, bearing in mind that the channel parameters of Table I differ substantially. Next, in Steps 3 and 4, the large-scale

parameters are taken into consideration, namely the received power, the total number of clusters, the angular spread and the delay spread, based on the PL model employed and the model's angular as well as temporal characteristics. Having acquired the large-scale parameters of the channel, the small-scale fading parameters can be generated. In Steps 5, 6 and 7, the per-cluster features are determined, more specifically the per-cluster power, the number of MPCs in each cluster and the power associated with each MPC, respectively. Afterward, the angular and temporal attributes of all MPCs, namely the AoD, AoA as well as the MPCs' delays are obtained in Steps 8 and 9. In Step 10, the transmitter and receiver antenna polarization characteristics are extracted. By now, all parameters required for generating the mmWave channel are ready, hence the CIR

coefficients can be generated in Step 11, based on, for instance, the IEEE 802.15.3c channel model of (23), IEEE 802.11ad of (24) or that of the general clustered multi-path representation in (26), followed by applying the losses imposed on each MPC.

B. System Design Considerations

The challenge of mmWave system design is to construct a system capable of successfully communicating over the mmWave channel, despite its high PL and sparse scattering. Wireless communications at mmWaves is constrained by many limitations, such as its propagation characteristics discussed in Section II. However, diverse techniques can be employed for mitigating the effects of these limitations, such as applying beamforming and reducing the cell size. In Figure 26, we show the main techniques, their limitations and performance improvements, application scenarios and future work on mmWaves. Any design should take these different aspects into consideration. In what follows, we present the main considerations and potentials of mmWaves.

- *Beamforming*: To overcome the high path loss, and thereby to enable wireless link establishment at mmWaves, having at least one end equipped with beamforming capability is imperative, employing at least one antenna array associated with a large number of antennas. The beamforming, shown in Figure 26 and Figure 27, is generally applied by focusing the transmitted signal towards the receiver or towards the best arriving MPC, while suppressing other weaker paths, which can be achieved via DBF, ABF, or combined hybrid techniques known as HBF techniques [84]. Further insights on beamforming techniques conceived for mmWaves are provided in the following section.

- *Massive MIMO*: Owing to the ability of stacking a large number of AEs in relatively small areas, even at mobile devices, the concept of massive MIMOs [81] can be flexibly introduced, which is capable of substantially enhancing the spectral efficiency without any extra bandwidth and power consumption [229].

- *Small Cells*: Another essential technique of combating the high attenuation and path loss at mmWaves is to shrink the cell-size, yielding the small cells seen in Figure 26. This can limit the signal attenuation as well as increase the overall capacity. Shorter communication distances are essential for mmWaves systems, such as the mobile broadband [12], [15], [37], [38], [41], [82], [110] as well as indoor WPAN and WLAN networks [11], [14], [27], [83].

- *Wideband Techniques*: Despite the fact that the mmWave channel imposes only low delays on the order of nanoseconds, the huge available bandwidth requires a high sampling frequency, which is at least twice the bandwidth [5]. This requirement imposes a high time dispersion in terms of the number of samples, although many of them are small, hence resulting in the so-called sparse scattering. Furthermore, due to the huge bandwidth available at each of the mmWave bands, their frequency components experience independent fading, which leads to frequency-selective channels. As a solution, employing wideband techniques, such as Orthogonal Frequency-Division Multiplexing (OFDM), Multi-Carrier Code Division Multiple Acess (MC-CDMA) [1], [230], are of high importance, as shown in Figure 27. Shown in Figure 26 multiple modulation techniques used for mmWaves. Indeed, using OFDM at mmWave frequencies has numerous advantages, hence it is already deployed in IEEE802.15.3c [14] for WPAN and also considered for other systems, as detailed in [30], [43], [81], [231]–[233]. However, OFDM suffers from high PAPR and it is sensitive to phase noise, hence leading to less efficient linear class-A power amplifiers, which thereby degrade the overall performance of the system. An alternative technique is to opt for single carrier (SC) modulation [81], [93], [234], [235] combined with frequency domain equalization (FDE) to mitigate the ISI caused by the frequency selective channel, since SC-FDE tolerates power-efficient nonlinear amplifiers and it is also tolerant to phase noise [236].

- *Modulation Techniques*: Nonetheless, less complex modulation techniques may be considered, such as frequency shift keying (FSK), amplitude shift keying (ASK), on-off keying (OOK) and pulse position modulation (PPM), as discussed by Daniels *et al.* in [93]. Another beneficial technique is constituted by constant-envelope OFDM (CE-OFDM) [81] combined with other near-CE techniques, such as the near-CE technique discussed in [234] relying on a null cyclic prefix SC (NCP-SC). In CE techniques the input symbols are phase modulated in order to avoid the high PAPR requirement of OFDM and to relax the linearity requirement of the Power Amplifiers (PAs), especially for systems associated with large antenna arrays. Furthermore, another modulation technique referred to as antenna subset modulation (ASM) was advocated in [237], which is based on generating the phase and amplitude components of the signal by manipulating its far-field pattern with the aid of switches for choosing a group of activated AEs from the full set of the antenna array, which is capable of achieving an improved array gain.

- *Duplexing Technique*s: The relevant duplexing techniques have not been widely discussed in the literature. At this early stage, time division duplexing (TDD) is deemed to be the best option for mmWave [82], [234], which is also compatible with massive MIMOs, since the downlink transmitter can exploit the channel estimate of the co-located receiver for transmit pre-processing [38], [238]. However, lately the huge bandwidth of the mmWave frequency bands has deviated some of the attention towards frequency division duplexing (FDD) [178].

- *Multi-User Grouping*: Many contributions have lately considered user grouping in Multi-User (MU) systems [177], [231], [232], [239], [240], which is particularly beneficial at mmWaves due to their high attenuation that restricts the coverage area and to counteract the sparse multipath scattering. In this case, some of the users receiving a cluster from the same reflecting objects would
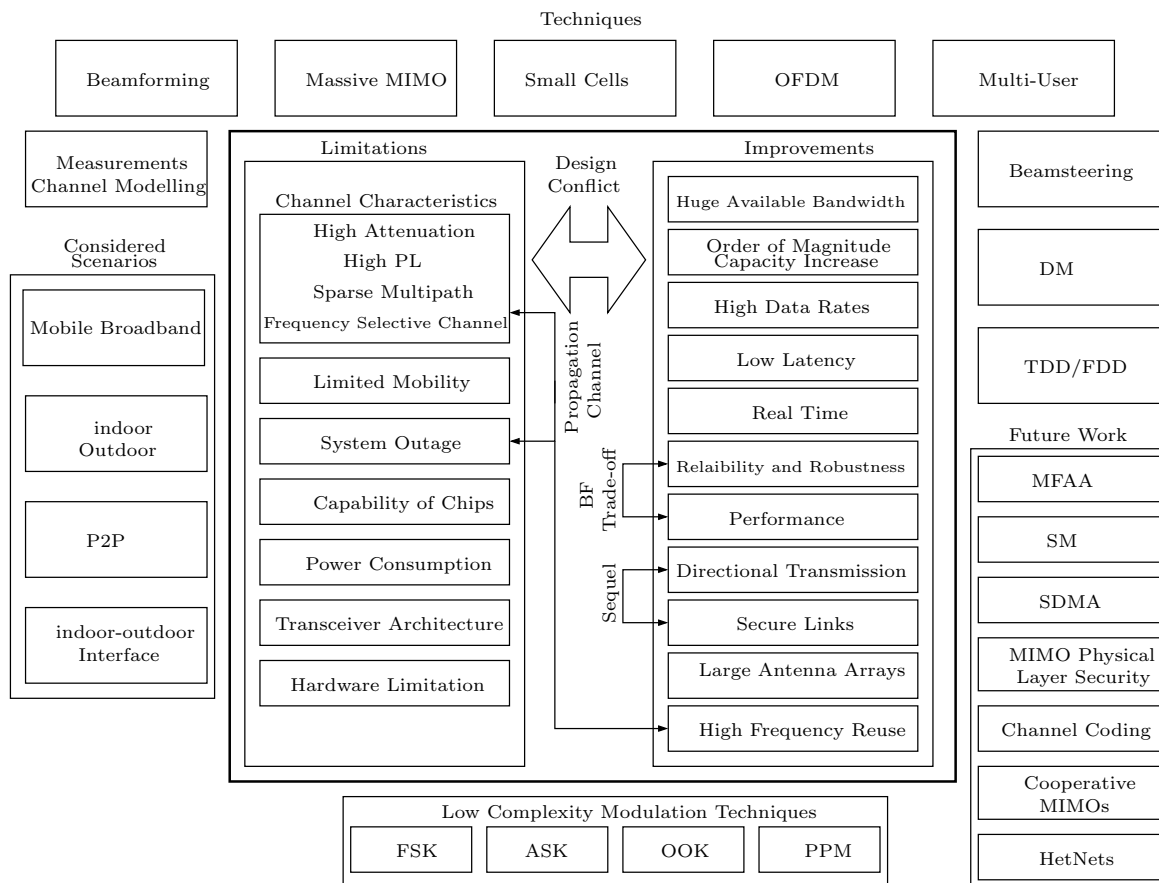
Figure 26. mmWave Technology available techniques, pros and cons, scenarios and future work.

share the same second-order spatial characteristics and hence maybe considered as one group [178].

- *MIMO techniques*: There is no constraint on using any of the existing MIMO techniques for mmWaves. However, the unfavorable propagation characteristics of the mmWaves should be taken into account. For instance, beamforming relying on directional antenna configurations is a key enabling technique for mmWave systems employing any MIMO technique for the sake of achieving performance enhancements. This facilitates the concept of multifunctional antenna arrays (MFAA), which are capable of simultaneously achieving different MIMO gains, such as diversity, multiplexing and beamforming gains [231]–[233], [241]–[245].
- *HetNets*: Due to their limitations, mmWave systems will only be employed for small cells combined with other existing wireless technologies in the form of heterogeneous networks [82], [182].

To expound a little further on the aforementioned MIMO techniques, MIMO systems have different requirements at the mmWave band from those in the sub-6 GHz band, as presented in Table XIII. For instance, the Space-Time Coding (STC) MIMO class can provide the system with diversity gains, which can enhance its integrity, especially in NLOS scenarios. By contrast, the achievable capacity of a MIMO system can be enhanced by employing Space-Division Multiplexing (SDM).

On the one hand, in the benign sub-6 GHz band, the bandwidth is rather limited and hence expensive. Hence, the employment of sophisticated SDM techniques is beneficial for increasing the transmission rate. On the other hand, in the mmWave band having substantial bandwidth relaxes the importance of SDM.

Explicitly, at mmWaves increasing the diversity gains or the rates is not as important as the BF gain, by virtue of the band's high PL. Hence, BF techniques are beneficial in the sub-6 GHz band, but they are considered as key enabling technologies in the mmWave band. Furthermore, BF can also be utilized at mmWaves for multi-user communications and can be conceived with Space-Division Multiple Access (SDMA) to separate the data streams of different users.

As discussed in Section II-A, employing directional transmissions at mmWave frequencies would indeed provide significant gains and in this section we provided a list of mmWave system design considerations, where beamsteering is an essential aspect, as shown in Figure 26. Therefore, in this section we describe how to achieve these gains using beamforming. Explicitly, directional transmission have to be used at mm-wave frequencies relying on antenna arrays, with the aid of beamforming. Naturally, the directionality of an antenna array depends on the number of array elements [246]. Explicitly, more elements results in the formation of narrower beams with all the signal energy concentrated in a particular direction improving the directionality of the antenna
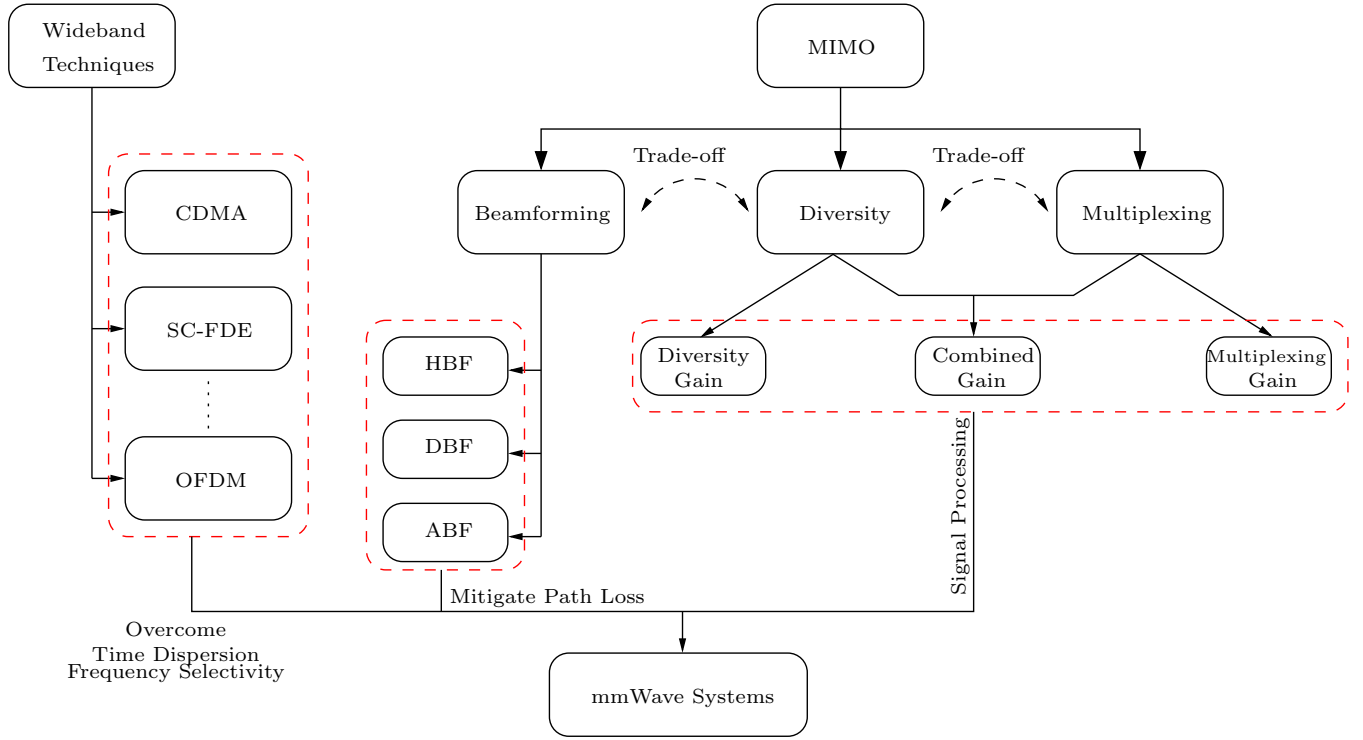
Figure 27. Design considerations for mmWave systems, which characterize the "Signal Processing" entrance to the "mmWave Technology" roundabout of Figure 2.

MIMO Type	<6 GH	mmWaves
STC	Enhanced integrity	Not necessary
SDM	Multiplexing gain	Relaxed by the huge bandwidth
BF	SNR gain	Essential + can be used for MU scenarios
SDMA	Multiuser communications	Optional

Table XIII
THE DIFFERENCE BETWEEN MMWAVE AND SUB-6 GHZ MIMO TYPES CONSIDERATIONS.

array [246]. Thus, the antenna design plays a salient role in achieving the required beamforming gain, and hence in the next section we discuss the antenna design considerations of mmWave communications.

C. Antenna Design Considerations

Again, beamforming gains are derived using an antenna array, constructed several antenna elements (AEs) that can be placed obeying different geometries. The distance between the different antenna elements plays an important role in terms of the gain as well as directionality of the beam. In this section we briefly discuss the associated antenna design guidelines such as the type of antenna arrays, array gain and beamwidth.

1) Antenna Arrays: A typical linear antenna array is shown in Figure 28, which portrays the departing and arriving rays

at the antenna arrays of the Tx and Rx, with ϕ_{Tx} and ϕ_{Rx} being the angle of departure and angle of arrival.
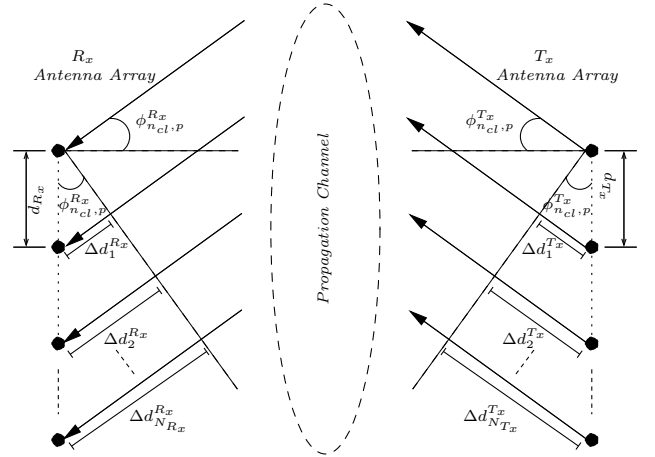

Figure 28. Outgoing and incoming signal rays of the p-th ray in the n_{cl}-th cluster at both T_x and R_x ULA antennas. Both arrays have separation distances d_{T_x} and d_{R_x} and corresponding departing and arriving angles ϕ_{T_x} and ϕ_{R_x}. The distance differences Δd between rays of the same ULA possess a specific progressive phase difference according to the antenna element position.

Electronically steered antenna arrays constitute key enablers of directional communication and at mmWaves can be densely packed in compact spaces compared to the sub-3 GHz band due to their shorter wavelength [38], [46]. Figure 29 shows the uniform linear array (ULA), the uniform planar array (UPA) and the uniform circular array (UCA).

Firstly, the ULA shown in Figure 29(a) has uniformly-spaced antenna elements (AEs) along one dimension with an inter-element separation of d, where the AF of the ULA operating at a carrier frequency of f and wavelength of λ is given by [246]:

$$\Omega_{ULA}(\theta, \varphi) = [1, \ldots, e^{jm\frac{2\pi}{\lambda}d_x \sin(\varphi)}, \ldots]^T, \quad (28)$$

where m_x is the index of an AE and $0 \le m_x \le N_x - 1$. In a ULA, either the elevation or the azimuth perspective is considered, since it is a one-dimensional antenna array. The ULA was used for mmWaves in [8], [38], [46]. Secondly, the UPA is a two-dimensional antenna array associated with AF [246], [247] given by:

$$\Omega_{UPA}(\theta, \varphi) = [1, \ldots, e^{j[m_x \Phi_x + n_y \Phi_y]}, \ldots]^T, \quad (29)$$

where we have:

$$\begin{cases} \Phi_x = & \frac{2\pi}{\lambda} d_x \sin(\theta)\cos(\varphi) \\ \Phi_y = & \frac{2\pi}{\lambda} d_y \sin(\theta)\sin(\varphi) \end{cases}, \quad (30)$$

given that Φ_x and Φ_y indicate the horizontal and vertical components of the antenna array. In the UPA antenna array, shown in Figure 29(b) relying on $N = N_x N_y$ antennas, the AE indices m_x and n_y at the x-axis and y-axis are bounded as $1 \le m_x \le N_x - 1$ and $1 \le n_y \le N_y - 1$, where N_x and N_y are the number of columns and rows of the UPA associated with d_x and d_y inter-element separation distances, respectively. This type of antenna arrays is preferable for mmWaves, since it can accommodate more AEs within small area at both the mobile station (MS) and the base station (BS) [38], [46]. It also facilitates beamforming in an extra dimension, which results in the 3D-beamforming [8]. Finally, a UCA antenna array associated with N_{cr} antennas has its AEs evenly distributed in a circular geometry with a uniform separation angle $\varphi_{n_{cr}}$ as shown in Figure 29(c). The AF of UCA is given by [246], [247]

$$\Omega_{UCA}(\theta, \varphi) = [\ldots, e^{j\frac{2\pi}{\lambda} R \sin(\theta)\cos(\varphi - \varphi_{n_{cr}})}, \ldots]^T, \quad (31)$$

where $\varphi_{n_{cr}} = \frac{2\pi}{N_{cr}}(n_{cr} - 1)$ under the constraint of $1 \le n_{cr} \le N_{cr}$.
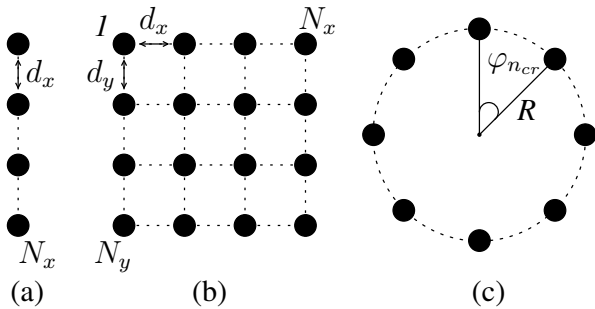

Figure 29. Antenna array geometries (a) ULA (b) UPA and (c) UCA.

There are other important steerable antenna types, like Lens Antennas [248] and Leaky-Wave antennas [249], which are not discussed here. We discuss the ULA in this paper as an example to show how antenna gains can be achieved. With the aid of the aforementioned arrays, it becomes possible to achieve the required beamforming gain by appropriately

placing the antenna elements. Thus, the achieved gain can help mitigate the high propagation losses encountered at mmWave frequencies. In the next subsection, we will discuss how to obtain the required gains for transmission from an antenna array.

2) Antenna Array Gain: In this section, we present the rudimentary concepts of array gain, since it is of salient importance to understand the gains needed for compensation of the losses. However, there are other design aspects such as mutual coupling, directivity, polarization, antenna bandwidth, etc which are not considered here, since they are beyond the scope of this paper. Owing to the high propagation losses incurred at mmWave frequencies, employing large antenna arrays is seen as a promising technique of compensating for the losses. The AEs are placed at a separation of $\lambda/2$ and they are fed with appropriately phased signals to form beams, where the signal energy is concentrated in the desired direction.

In this section, we provide the derivation of the antenna array gains. We also analyze the directionality and beamwidth obtained for different number of antennas. We focus our analysis mainly on linear antenna arrays, since the UPA and UCA constitute extensions to linear arrays.

Consider a wavefront crossing a linear antenna array having N AEs at an angle θ, as shown in Figure 30. The wave arriving at AE 1 travels an extra distance of $(d \cos \theta)$ with respect to the second element (AE 2), thus resulting in a phase difference of $\left(\frac{2\pi}{\lambda} d \cos \theta\right)$ between the two. Similarly, the phase difference between the first and the Nth AE is $\left((N-1)\frac{2\pi}{\lambda} d \cos \theta\right)$.
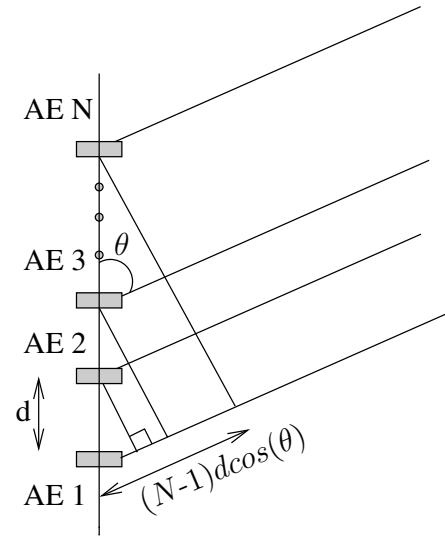

Figure 30. Signal passing through the array with N antenna elements (AE) at an angle θ.

The response vector and the array factor[8] for such an array configuration is given by [246]:

---

[8] In antenna design, array gain is usually expressed in terms of array factor, where AF is a linear scale while array gain is the AF expressed in decibels (dB)

$$\mathbf{a}_r = [1 \ e^{j\psi} \ e^{j2\psi} \dots e^{j(N-1)\psi}], \tag{32}$$

$$AF = a_0 + a_1 e^{j\psi} + \dots + a_{N-1} e^{j(N-1)\psi}, \tag{33}$$

$$\psi = (2\pi/\lambda)d\cos\theta + \beta = kd\cos\theta + \beta, \tag{34}$$

where $a_0, a_1, \dots, a_{N-1}$ are or voltage levels of the array [250], d is the spacing between the antenna elements and β is the excitation phase of the array, which is induced by the source due to the phase changes imposed on the currents passing through the array [250], [246]. Furthermore, k is the wave-number equal to $\frac{2\pi}{\lambda}$, which is a measure of the number of cycles in the wave present in one meter of distance and ψ is often termed as the wave-number variable which depends on the wave-number k.

For ULA, we have $a_0 = a_1 = \dots a_{N-1} = 1$ and the array factor for such an array using (33) is given by [246]:

$$\begin{aligned} AF &= 1 + e^{j\psi} + \dots + e^{j(N-1)\psi} \\ &= e^{j\frac{(N-1)}{2}\psi}\left[\frac{e^{j\frac{N}{2}\psi} - e^{-j\frac{N}{2}\psi}}{e^{j\frac{N}{2}\psi} - e^{-j\frac{N}{2}\psi}} \right] \\ &= e^{j\frac{(N-1)}{2}\psi}\left[\frac{\sin(\frac{N}{2}\psi)}{\sin(\frac{1}{2}\psi)} \right], \end{aligned} \tag{35}$$

assuming that the center of the antenna array is the reference point, when we get $AF = \left[\frac{\sin(\frac{N}{2}\psi)}{\sin(\frac{1}{2}\psi)} \right]$.
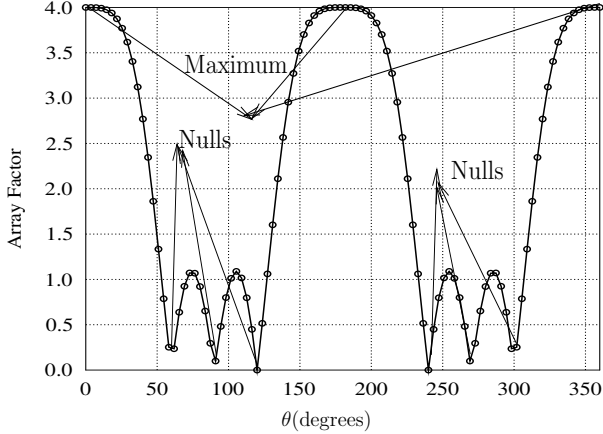

Figure 31. Array gain obtained at different angular directions, the first null (zero gain) is seen at 60° while first maximum is seen at 0°.

The direction, where the radiation or the gain of the antenna array is zero, is referred to as a null. The nulls of the array occur at $\theta_n = \cos^{-1}\left(\frac{\lambda}{2\pi d}(-\beta \pm \frac{2n}{N}\pi) \right)$, where $n = 1, 2, 3, \dots; \forall n \neq N, 2N, \dots$ The maximum gain of the antenna array occurs at $\theta_m = \cos^{-1}\left(\frac{\lambda}{2\pi d}(-\beta \pm 2m\pi) \right)$, where $m = 0, 1, 2, \dots$ The AF for N= 4 antenna elements at $\lambda/2$-spacing with zero excitation phase is shown in Figure 31. The first null in Figure 31 occurs at 60°, while the first maximum occurs at 0°. The directivity of an antenna array is defined as its radiation intensity in the direction of its strongest emission with respect to an isotropic antenna array, which transmits uniformly in all directions.

As the number of antenna elements increases, narrower beams are formed, which increases the directionality of the array. The array gain for different number of AEs at $\lambda/2$ spacing is shown in the Figure 32. It is interesting to see from Figure 32 that the mainbeam lobe of the array having N = 2 antenna elements is wider and spans from 140° to 230° while the mainbeam lobe of the array with N=4 AEs spans from 150° to 205°. Similarly, the mainbeam lobe of an N=10 element array is narrower than that of 2 and 4 element antenna arrays as shown in Figure 32.
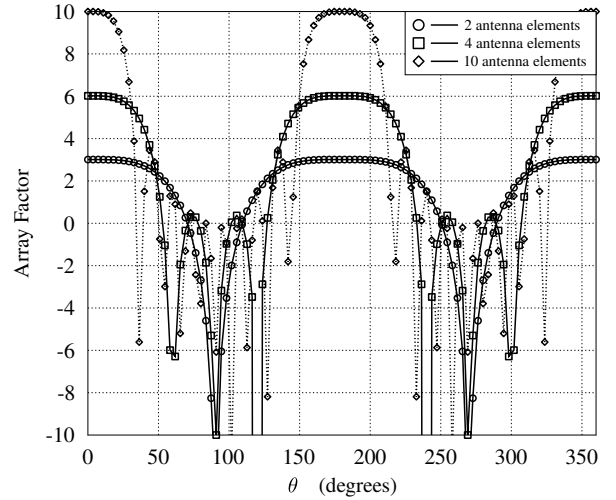

Figure 32. Array gain with N=2, 4, and 10 antenna elements

For better understanding of the beam patterns, polar plots of the radiation pattern are shown in Figure 33. It is clear from Figure 33 that the radiation pattern of the mainbeam lobe becomes narrower as the number of AEs increased from N= 4 to N= 10. Figure 33(a) and Figure 33(b) correspond to the array gains obtained in Figure 32 for N= 4 and N= 10 antenna elements.

Another important factor that affects the mainbeam lobe is the spacing between the antennas. As the spacing between the AEs increases from $\lambda/2$ to λ, side lobes are observed as shown in the Figure 34(c), for AE spacing of λ. To elaborate, grating lobes are the mainbeam lobes in the undesirable directions, which are formed because of the over-sampling and the repetition of the AF values in the region $-kd \leq \psi \leq kd$, when $kd > \pi$ [250]. Grating lobes are unnecessary for beamforming in cellular communications and indeed, they can be avoided by maintaining a reduced space between the antenna, i.e., $d < \lambda/2$. Also seen in Figure 34(a) that, when the spacing between the AEs is decreased from $\lambda/2$ to $\lambda/16$, the beam becomes wider, resulting in a loss of directionality. Figure 34(b) shows that when the spacing between AEs is $\lambda/2$, no side lobes are observed and maintains directionality.
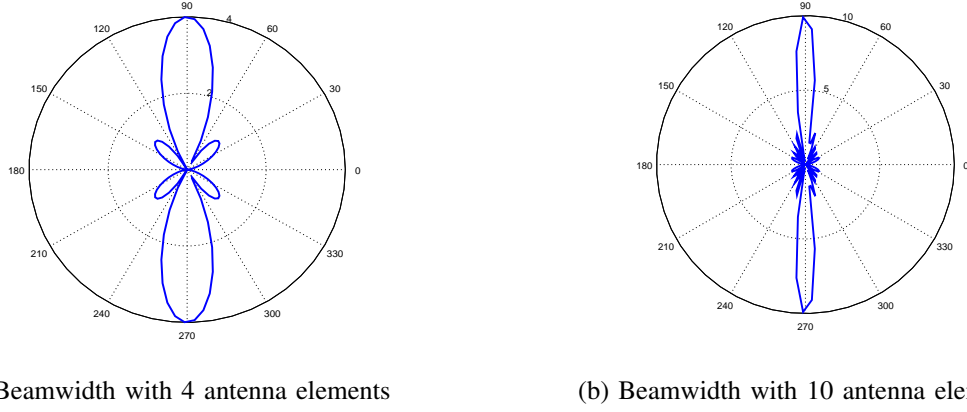
(a) Beamwidth with 4 antenna elements

(b) Beamwidth with 10 antenna elements

Figure 33. Polar plots representing the beamwidth of 4 and 10 antenna elements.

(a) Beamwidth for $\lambda/16$ spacing between antenna elements

(b) Beamwidth for $\lambda/2$ spacing between antenna elements
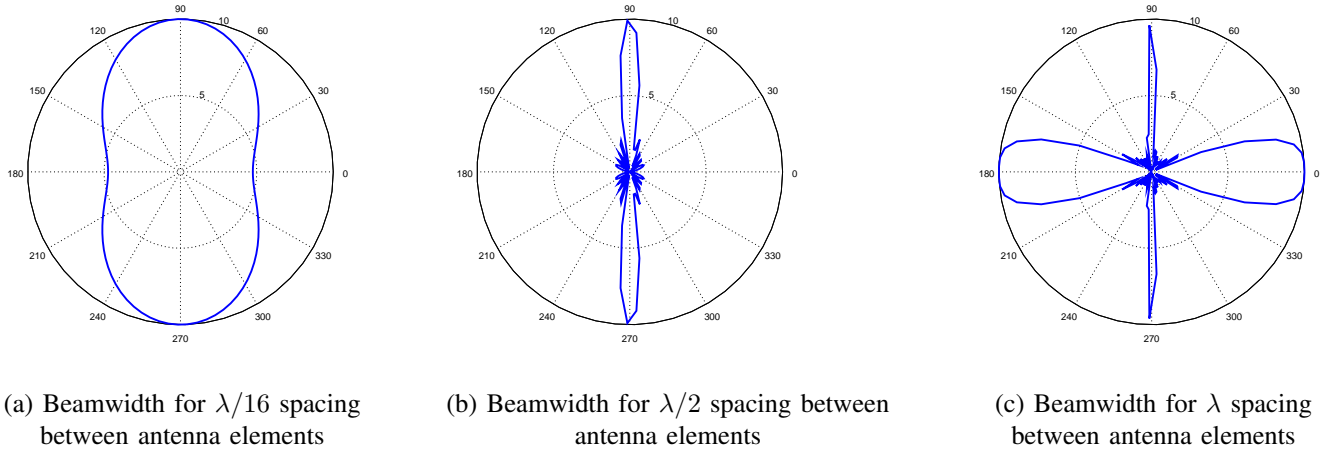
(c) Beamwidth for λ spacing between antenna elements

Figure 34. Polar plots representing the beam patterns at $\lambda/16$, $\lambda/2$, and λ spacing between antenna elements.

Furthermore, it is of seminal importance to understand the beamwidth of the signal with different AEs. The half-power beamwidth is defined as the angular separation of radiation from the main lobe to half the power of the main lobe, i.e -3dB from the main lobe. Twice the half-power beamwidth is referred to as the 3dB beamwidth. beamwidth for a uniformly linear antenna array steered towards the desired direction θ_o is obtained by linearizing the wave-number variable ψ about $\theta = \theta_0$, which is given by [250]:

$$
\begin{aligned}
\triangle\phi_{\text{3dB}} &= \frac{1}{kd\sin\theta_o}\triangle\psi_{\text{3dB}} \text{ for } 0° < \theta < 180° \\
&= 2\sqrt{\frac{\triangle\psi_{\text{3dB}}}{kd}} \text{ for } \theta_0 = 0° \text{and } 180°,
\end{aligned}
\tag{36}
$$

where $\triangle\psi_{\text{3dB}}$ is the beamwidth at broadside, and it is equal to $0.886\frac{2\pi b}{N}$. Furthemore, 'b' is the broadening factor, and it depends on the type of the window and the attenuation of the sidelobe level.

In Figure 35, the beamwidth of different number of AEs steered at different directions is shown. As shown in Figure 35, that as the beam is steered from 0° to 90°, the beamwidth decreases. The beamwidth also depends on the angle at which the signal impinges on the array [246]. Upon increasing in the number of AEs in an array, the beamwidth decreases in the desired direction. In other words, the beamwidth of an array depends both on the number of AEs and on the steering angle.
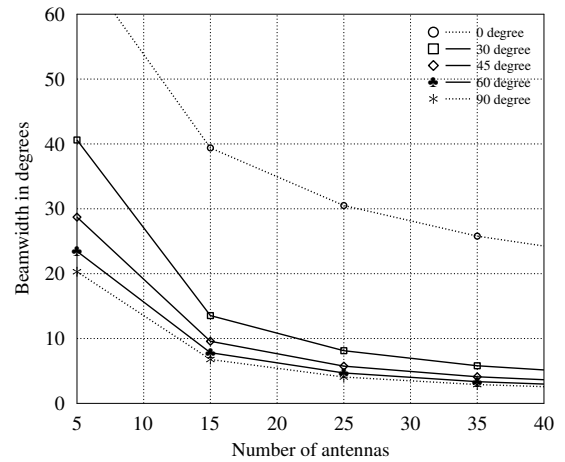

Figure 35. Beamwidth vs number of AEs at different desired angle of departures.

Depending on the space available for the array and on the gain requirements of both the base station and of the mobile

station, it is important to opt for the appropriate type of antennas to be employed. Having considered the beamforming gains, let us now discuss in the next section the number of antennas required for compensating the path-loss with the aid of the link budget.

D. Link Budget Analysis

To establish a communication link between a transmitter and a receiver, it is important to carefully adjust the transmit power and the received power required at the receiver for maintaining the desired data rate for a given channel, given a certain thermal noise level at the receiver. This power analysis is required for establishing a link which relies on the link budget. The link budget of a communication system depends mainly on the base station's and the mobile station's specifications, such as the transmit power, antenna gain, signal-to-noise ratio (SNR) and the required throughput of the link.

Link Budget	Downlink	Uplink
Transmit power (dBm)	40.00	20.00
Transmit antenna gain (dBi)	25.00	17.00
Carrier frequency (GHz)	28.00	28.00
Distance (km)	0.5	0.5
Free space propagation loss (dB)	115.32	115.32
Other losses (shadowing, fading)	20.00	20.00
Receive antenna gain (dBi)	12.00	25.00
Received power (dBm)	-58.32	-73.12
Bandwidth (GHz)	0.50	0.5
Thermal noise (PSD) (dBm/Hz)	-174.00	-174.00
Noise figure	7	7
Thermal noise (dBm)	-80.01	-80.01
SNR (dB)	21.69	6.89
Implementation loss (dB)	6.00	6.00
Spectral efficiency	6.20	1.2
Data rate (Gbps)	3.1	0.6

Table XIV
LINK BUDGET FOR A TYPICAL MMWAVE COMMUNICATION SYSTEM [41].

A link budget for a typical uplink and downlink in mmWave communications is shown in the Table XIV [41]. For the downlink scenario of Table XIV, a 28 GHz carrier is chosen with a base station transmit power of 40 dBm [41]. Using the path loss model in (17), which best fits for the 28 GHz communication system as described in Section III-D the propagation loss for over 0.5 km distance using (17) in a LOS environment ($n_p = 2$) with an average shadowing loss of 20 dB is 115.32 dB. Our aim is to achieve a data rate of 3.1 Gbps in a 0.5 GHz bandwidth. In this scenario, authors of [251] has demonstrated using system level simulations that a data rate as high as 7.5 Gbps can also be achieved. For successful establishment of the link at a 3.1 Gbps throughput, using Shannon's channel capacity [252], it requires 15.69 dB of SNR. However, the gain times bandwidth product of the RF components at such high frequencies is still low at the time of writing [82]. Hence owing to the other system losses such as the power dissipation of the circuitry, ADC/DAC, impedance mismatch, etc an additional 6 dB loss is considered. Hence

a total of 21.69 dB SNR is required to establish this link. Hypothetically, we assume a noise figure of 7dB [253], and a thermal noise[9] of -174 dBm/Hz. We also assume 12 dBi of receive antenna gain. Assuming 12 dBi gain at the mobile station is realistic, since it can be achieved by a four element array with 6dBi gain for each individual element using patch antennas.

With these values in Table XIV and using (17) in $P_t = G_t + G_r + PL$, the base station has to have an antenna gain of around 25 dBi. We assume the gain of an antenna element at the base station to be 10dBi [41] since a low gain antenna would provide higher steering capability and minimal power leakage to side lobes [254] . Accordingly, we would need around 15 dBi additional gain to achieve a rate of 3.1 Gbps. The total gain of the antenna array having $d = \lambda/2$ spacing is $G_{\text{antenna}} = (\eta G_{\text{element}} N)$, where η characterizes the capability of the antenna array to steer the beam only in the desired direction. On a dBi scale, we can view the gain of G_{antenna} as the sum of the gains obtained by the array and the element as:

$$G_{\text{antenna}}(\text{dBi}) = 10 \log \eta + G_{\text{element}}(\text{dBi}) + \text{Array Gain(dB)}. \quad (37)$$

Therefore, an additional 15dBi gain is derived from the array. To obtain 15dBi gain from the array with $\eta = 1$, we would need $10^{15/10} \approx 32$ antenna elements. However, in practice $\eta \neq 1$, since there would be a non-negligible power (radiation) in other directions, particularly during steering. In other words, it is impractical to have narrow pencil beam so as to achieve the maximum attainable gain from antenna arrays. For a high-integrity, more than 32 antenna elements are required, depending on the directivity of the array. Figure 36 shows the array gain at three different efficiencies. For $\eta = 0.75$, around 40 antenna elements are required to obtain an array gain of 15dBi and for $\eta = 0.5$, as many as 60 antenna elements are required.

Similarly, the receive antenna gain of 12 dBi in Table XIV at the mobile station can be derived using a four antenna element array with an element gain of 6dBi.

As we go increase the frequency from the microwave frequencies to the millimeter wave frequencies, the availability of bandwidth to meet the data requirements of the mobile users increases significantly. However, the price to pay is that, there is a significant propagation loss associated with the frequencies as shown in Figure 37. Upon doubling the frequency, there is a 6dB loss in the link budget, for a given antenna gain. The dip at 60 GHz is because of the oxygen absorption. Therefore, 60 GHz frequency is not suitable for outdoor environments.

One way to overcome the propagation loss is by using beamforming with the aid of antenna arrays as discussed in the above section. Owing to the fact that at millimeter wave frequencies the spacing between the antennas becomes small, a large number of antenna elements can be employed at the base station to achieve high gains using beamforming.

---

[9]Thermal noise is $10 \log(1000 \, KT)$dBm, where $K = 1.38064852 \times 10^{-23}$ is the Boltzmann constant and T is the room temperature in kelvin = 300.
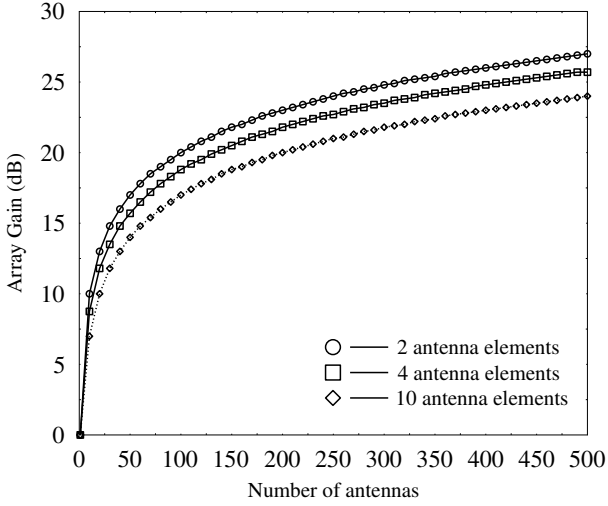
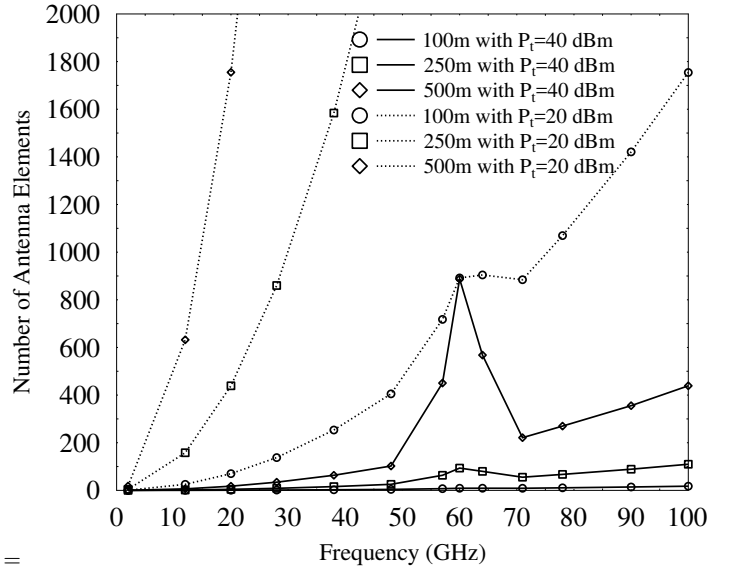Figure 36. Array gain for different number of antenna elements at $\eta = 1, 0.75,$ and, 0.5.

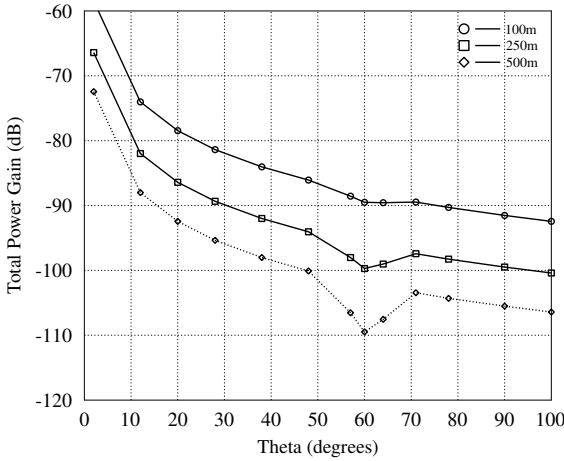Figure 38. Number of antenna elements required to compensate for the path loss versus the carrier frequency .

fer from other losses, such as oxygen absorption, foliage attenuation, and rain-induced fading, and other factors as discussed in Section II.
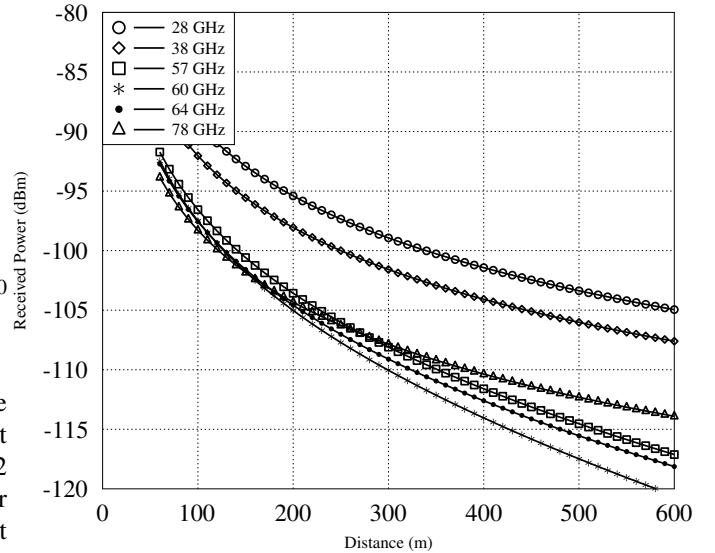

Figure 37. Received power at different frequencies at a transmit power =40 dBm.

Figure 39. Downlink received power verses cell radius at frequencies of 28, 38, 57, 60, 64 and 78 GHz at the transmit power of 40dBm. XIV

To have a better understanding of how many antennas are required at the base station, we consider again the link budget summarized in Table XIV, for a spectral efficiency of 6.2 bps/Hz at different frequencies. Figure 38 shows the number of antenna elements required for compensating the path loss at different frequencies. These values at different frequencies are obtained using similar analysis to that discussed for 28 GHz. Because of the high propagation losses at high frequencies, there is an exponential growth in the number of antenna elements required. For example, at 78 GHz, for a 500 meter cell radius, a few hundred antennas are needed to compensate for the path loss.

Apart from shadowing, mmWave communications also suf-

The power received at the MS at different distances for various frequencies is shown in Figure 39. It is interesting to investigate the path loss associated with the distance so as

to determine the coverage area and the number of antenna elements required for beamforming in order to increase the cell area. Observing from Figure 39, that 57, 60, and 64 GHz have relatively high attenuation due to the oxygen absorption and they are not suitable for outdoor environments. Similarly, 78GHz has relatively high propagation loss than 28, and 38GHz. However, the deployment of a carrier frequency also depends on the beamforming gain required for compensating the path loss. Figure 40 shows the number of AEs required for achieving a spectral efficiency of 6bps/Hz at various frequencies for different cell radii.
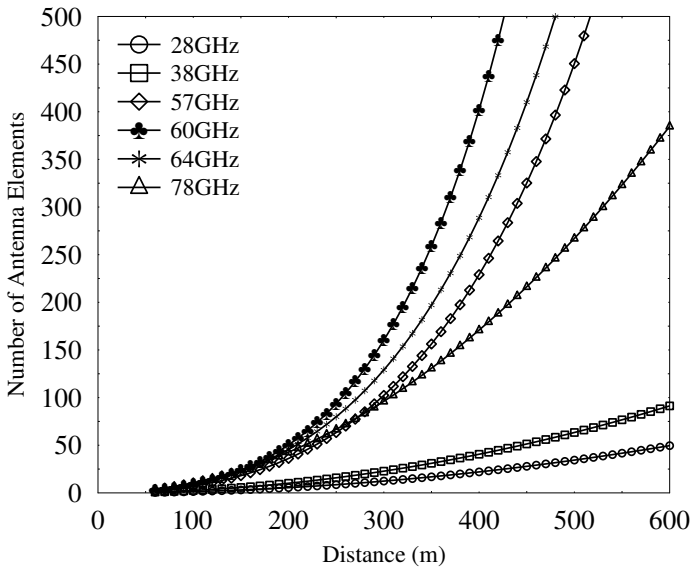

Figure 40. Number of antenna elements required for different cell radii to achieve spectral efficiency of 6bps/Hz at 28, 38, 57, 60, 64 and 78GHz.

It is evident from Figure 40 that for 60GHz hundreds of antennas are required to compensate for the losses due to attenuation using BF. The carriers of 57 GHz, 60 GHz and 64 GHz, are more suitable for indoor environments, as employed in IEEE802.11ad, whereas for 28 GHz, and 38 GHz using less than hundred antennas, a cell radius of 600 meters can be achieved. Although 78 GHz necessitates few hundreds of antennas to cover the cell radius of 600 meters, given the flexibility and the size of the antennas, this may still be feasible.

V. CONCLUSIONS

In this paper, we reviewed the salient mmWave propagation characteristics, including the free-space path loss, atmospheric attenuation, rain and foliage attenuation, material penetration and other propagation factors. We then reviewed the mmWave channel models and discussed the mmWave communication systems' requirements, and challenges. Finally, we provided an overview on the relevant design guidelines, such as system antenna design considerations followed by the rudimentary link budget analysis of mmWave communications, where we explored the minimum required number of antennas in order to achieve a specific data rate, such as for example 3Gbps.

REFERENCES

[1] L. Hanzo, H. Haas, S. Imre, D. O'brien, M. Rupp, and L. Gyongyosi, "Wireless Myths, Realities, and Futures: From 3G/4G to Optical and Quantum Wireless," *Proceedings of the IEEE*, vol. 100, no. Special Centennial Issue, pp. 1853–1888, May 2012.

[2] B. Mondal, T. Thomas, E. Visotsky, F. Vook, A. Ghosh, Y.-H. Nam, Y. Li, J. Zhang, M. Zhang, Q. Luo, Y. Kakishima, and K. Kitao, "3D channel model in 3GPP," *IEEE Communications Magazine*, vol. 53, no. 3, pp. 16–23, March 2015.

[3] Cisco. (2016, February) Cisco Visual Networking Index: Global Mobile Data Traffic Forecast Update, 2015–2020. Cisco. [Online]. Available: http://www.cisco.com/c/en/us/solutions/collateral/service-provider/visual-networking-index-vni/mobile-white-paper-c11-520862.html

[4] Ericsson. (2016, June) Ericsson Mobility Report. Ericsson. [Online]. Available: http://www.ericsson.com/mobility-report

[5] K. Huang and Z. Wang, *Millimeter Wave Communication Systems*, ser. IEEE Series on Digital & Mobile Communication. Wiley, 2011. [Online]. Available: https://books.google.co.uk/books?id=kCmyPdxme1AC

[6] T. Rappaport, S. Sun, R. Mayzus, H. Zhao, Y. Azar, K. Wang, G. Wong, J. Schulz, M. Samimi, and F. Gutierrez, "Millimeter Wave Mobile Communications for 5G Cellular: It Will Work!" *IEEE Access*, vol. 1, pp. 335–349, 2013.

[7] M. Akdeniz, Y. Liu, M. Samimi, S. Sun, S. Rangan, T. Rappaport, and E. Erkip, "Millimeter Wave Channel Modeling and Cellular Capacity Evaluation," *IEEE Journal on Selected Areas in Communications*, vol. 32, no. 6, pp. 1164–1179, June 2014.

[8] O. El Ayach, S. Rajagopal, S. Abu-Surra, Z. Pi, and R. Heath, "Spatially Sparse Precoding in Millimeter Wave MIMO Systems," *IEEE Transactions on Wireless Communications*, vol. 13, no. 3, pp. 1499–1513, March 2014.

[9] E. International. (2010, Dec) Standard ECMA-387: High Rate 60 GHz PHY, MAC and HDMI PALs . [Online]. Available: www.ecma-international.org/publications/standards/Ecma-387.htm

[10] WiGig. (2010, July) WiGig White Paper: Defining the Future of Multi-Gigabit Wireless Communications. [Online]. Available: http://wirelessgigabitalliance.org/specifications/

[11] WirelessHD. (2010, 2010) WiHD: 60 GHz WirelessHD Specification Version 1.1 Overview. [Online]. Available: http://www.wirelesshd.org/about/specification-summary/

[12] F. Khan and Z. Pi, "mmwave Mobile Broadband (MMB): Unleashing The 3-300GHz Spectrum," in *Sarnoff Symposium, 34th IEEE*, May 2011, pp. 1–6.

[13] S. Hur, T. Kim, D. Love, J. Krogmeier, T. Thomas, and A. Ghosh, "Millimeter Wave Beamforming for Wireless Backhaul and Access in Small Cell Networks," *IEEE Transactions on Communications*, vol. 61, no. 10, pp. 4391–4403, October 2013.

[14] IEEE, "IEEE WPAN 802.15.3c Millimeter-Wave based Alternative Physical Layer Extension," pp. c1–187, Oct 2009. [Online]. Available: http://www.ieee802.org/15/pub/TG3c.html

[15] Z. Pi and F. Khan, "An Introduction to Millimeter-Wave Mobile Broadband Systems," *IEEE Communications Magazine*, vol. 49, no. 6, pp. 101–107, June 2011.

[16] M. Shafi, A. F. Molisch, P. J. Smith, T. Haustein, P. Zhu, P. D. Silva, F. Tufvesson, A. Benjebbour, and G. Wunder, "5G: A Tutorial Overview of Standards, Trials, Challenges, Deployment, and Practice," *IEEE Journal on Selected Areas in Communications*, vol. 35, no. 6, pp. 1201–1221, June 2017.

[17] T. Rappaport, R. Heath, R. Daniels, and J. Murdock, *Millimeter Wave Wireless Communications*, ser. Prentice Hall Communications Engineering and Emerging Technologies Series from Ted Rappaport. Pearson Education, 2014. [Online]. Available: https://books.google.co.uk/books?id=0Jh6BAAAQBAJ

[18] L. A. Hoffman and K. H. Hurlbut, "A 94-GHz RADAR for Space Object Identification," in *Microwave Symposium, 1969 G-MTT International*, May 1969, pp. 475–484.

[19] K. Button, *Infrared and Millimeter Waves V4: Millimeter Systems*, ser. Infrared and Millimeter Waves. Elsevier Science, 2014. [Online]. Available: https://books.google.co.uk/books?id=_D9HvmdlTS4C

[20] W. O. Copeland, J. R. Ashwell, G. P. Kefalas, and J. C. Wiltse, "Millimeter-Wave Systems Applications," in *Microwave Symposium, 1969 G-MTT International*, May 1969, pp. 485–488.

[21] H. H. Meinel, "System Design, Applications And Development Trends In The Millimeter-Wave Range," in *18th European Microwave Conference*, Sept 1988, pp. 1203–1217.

[22] J. W. Dees, R. J. Wangler, and J. C. Wiltse, "System Considerations for Millimeter Wave Satellite Communications," *IEEE Transactions on Aerospace and Electronic Systems*, vol. AES-2, no. 6, pp. 195–213, Nov 1966.

[23] E. Damosso, L. Stola, and G. Brussaard, "Characterisation Of The 50-70 Ghz Band For Space Communications," *ESA Journal*, vol. 7, pp. 25–43, 1983.

[24] F. Giannetti, M. Luise, and R. Reggiannini, "Mobile and Personal Communications in the 60 GHz Band: A Survey," *Wireless Personal Communications*, vol. 10, no. 2, pp. 207–243, 1999. [Online]. Available: http://dx.doi.org/10.1023/A%3A1018308429332

[25] S. K. Yong and C.-C. Chong, "An Overview of Multigigabit Wireless through Millimeter Wave Technology: Potentials and Technical Challenges," *EURASIP J. Wireless Comm. and Networking*, vol. 2007, 2007. [Online]. Available: http://dblp.uni-trier.de/db/journals/ejwcn/ejwcn2007.html#YongC07

[26] A. Natarajan, A. Komijani, X. Guan, A. Babakhani, and A. Hajimiri, "A 77-GHz Phased-Array Transceiver With On-Chip Antennas in Silicon: Transmitter and Local LO-Path Phase Shifting," *IEEE Journal of Solid-State Circuits*, vol. 41, no. 12, pp. 2807–2819, Dec 2006.

[27] A. Maltsev, V. Erceg, E. Perahia, C. Hansen, R. Maslennikov, A. Lomayev, A. Sevastyanov, A. Khoryaev, G. Morozov, M. Jacob, S. Priebe, T. Kurner, S. Kato, H. S. mand Katsuyoshi Sato, and H. Harada, "Channel Models for 60 GHz WLAN Systems," pp. c1–187, May 2010. [Online]. Available: http://www.ieee802.org/11/Reports/tgad_update.htm

[28] E. Ben-Dor, T. Rappaport, Y. Qiao, and S. Lauffenburger, "Millimeter-Wave 60 GHz Outdoor and Vehicle AOA Propagation Measurements Using a Broadband Channel Sounder," in *Global Telecommunications Conference (GLOBECOM 2011), IEEE*, Dec 2011, pp. 1–6.

[29] T. Rappaport, E. Ben-Dor, J. Murdock, and Y. Qiao, "38 GHz And 60 GHz Angle-Dependent Propagation for Cellular Angle-Dependent Propagation for Peer-to-Peer Wireless Communications," in *IEEE International Conference on Communications (ICC)*, June 2012, pp. 4568–4573.

[30] C. Sacchi, T. F. Rahman, I. A. Hemadeh, and M. El-Hajjar, "Millimeter-Wave Transmission for Small-Cell Backhaul in Dense Urban Environment: a Solution Based on MIMO-OFDM and Space-Time Shift Keying (STSK)," *IEEE Access*, vol. 5, pp. 4000–4017, 2017.

[31] V. Venkateswaran and A.-J. van der Veen, "Analog Beamforming in MIMO Communications With Phase Shift Networks and Online Channel Estimation," *IEEE Transactions on Signal Processing*, vol. 58, no. 8, pp. 4131–4143, Aug 2010.

[32] R. Walden, "Analog-to-Digital Converter Survey And Analysis," *IEEE Journal on Selected Areas in Communications*, vol. 17, no. 4, pp. 539–550, Apr 1999.

[33] J. Murdock and T. Rappaport, "Consumption Factor: A Figure of Merit For Power Consumption And Energy Efficiency In Broadband Wireless Communications," in *GLOBECOM Workshops (GC Wkshps), 2011 IEEE*, Dec 2011, pp. 1393–1398.

[34] P. Russer, "Si And SiGe Millimeter-Wave Integrated Circuits," *IEEE Transactions on Microwave Theory and Techniques*, vol. 46, no. 5, pp. 590–603, May 1998.

[35] T. Rappaport, J. Murdock, and F. Gutierrez, "State of the Art in 60-GHz Integrated Circuits and Systems for Wireless Communications," *Proceedings of the IEEE*, vol. 99, no. 8, pp. 1390–1436, Aug 2011.

[36] J. F. Buckwalter, S. Daneshgar, J. Jayamon, and P. Asbeck, "Series Power Combining: Enabling Techniques For Si/SiGe Millimeter-Wwave Power Amplifiers," in *IEEE 16th Topical Meeting on Silicon Monolithic Integrated Circuits in RF Systems (SiRF)*, Jan 2016, pp. 116–119.

[37] Z. Pi and F. Khan, "System Design and Network Architecture for a Millimeter-wave Mobile Broadband (MMB) System," in *Sarnoff Symposium, 34th IEEE*, May 2011, pp. 1–6.

[38] ——, "A Millimeter-Wave Massive MIMO System For Next Generation Mobile Broadband," in *Conference Record of the Forty Sixth Asilomar Conference on Signals, Systems and Computers (ASILOMAR)*, Nov 2012, pp. 693–698.

[39] T. Rappaport, F. Gutierrez, E. Ben-Dor, J. Murdock, Y. Qiao, and J. Tamir, "Broadband Millimeter-Wave Propagation Measurements and Models Using Adaptive-Beam Antennas for Outdoor Urban Cellular

Communications," *IEEE Transactions on Antennas and Propagation*, vol. 61, no. 4, pp. 1850–1859, April 2013.

[40] E. Torkildson, B. Ananthasubramaniam, U. Madhow, and M. Rodwell, "Millimeter-wave MIMO: Wireless Links at Optical Speeds," in *Proc. of 44th Allerton Conference on Communication, Control and Computing, Monticello, Illinois*, Sep. 2006.

[41] S. Rajagopal, S. Abu-Surra, Z. Pi, and F. Khan, "Antenna Array Design for Multi-Gbps mmWave Mobile Broadband Communication," in *Global Telecommunications Conference (GLOBECOM), IEEE*, Dec 2011, pp. 1–6.

[42] F. Mahmouli and S. Walker, "4-Gbps Uncompressed Video Transmission over a 60-GHz Orbital Angular Momentum Wireless Channel," *Wireless Communications Letters, IEEE*, vol. 2, no. 2, pp. 223–226, April 2013.

[43] W. Roh, J.-Y. Seol, J. Park, B. Lee, J. Lee, Y. Kim, J. Cho, K. Cheun, and F. Aryanfar, "Millimeter-Wave Beamforming as an Enabling Technology for 5G Cellular Communications: Theoretical Feasibility and Prototype Results," *Communications Magazine, IEEE*, vol. 52, no. 2, pp. 106–113, February 2014.

[44] S. Geng, J. Kivinen, and P. Vainikainen, "Propagation Characterization of Wideband Indoor Radio Channels at 60 GHz," in *IEEE International Symposium on Microwave, Antenna, Propagation and EMC Technologies for Wireless Communications, MAPE*, vol. 1, Aug 2005, pp. 314–317 Vol. 1.

[45] E. Torkildson, H. Zhang, and U. Madhow, "Channel Modeling for Millimeter Wave MIMO," in *Information Theory and Applications Workshop (ITA)*, Jan 2010, pp. 1–8.

[46] H. Zhang, S. Venkateswaran, and U. Madhow, "Channel Modeling and MIMO Capacity for Outdoor Millimeter Wave Links," in *Wireless Communications and Networking Conference (WCNC) IEEE*, April 2010, pp. 1–6.

[47] O. Andrisano, V. Tralli, and R. Verdone, "Millimeter Waves for Short-Range Multimedia Communication Systems," *Proceedings of the IEEE*, vol. 86, no. 7, pp. 1383–1401, Jul 1998.

[48] A. Alkhateeb, O. El Ayach, G. Leus, and R. Heath, "Hybrid Precoding for Millimeter Wave Cellular Systems With Partial Channel Knowledge," in *Information Theory and Applications Workshop (ITA)*, Feb 2013, pp. 1–5.

[49] R. W. Heath, N. Gonzalez-Prelcic, S. Rangan, W. Roh, and A. M. Sayeed, "An Overview of Signal Processing Techniques for Millimeter Wave MIMO Systems," *IEEE Journal of Selected Topics in Signal Processing*, vol. 10, no. 3, pp. 436–453, April 2016.

[50] E. Violette, R. Espeland, R. DeBolt, and F. Schwering, "Millimeter-wave Propagation At Street Level In An Urban Environment," *IEEE Transactions on Geoscience and Remote Sensing*, vol. 26, no. 3, pp. 368–380, May 1988.

[51] A. Alejos, M. Sanchez, and I. Cuinas, "Measurement and Analysis of Propagation Mechanisms at 40 GHz: Viability of Site Shielding Forced by Obstacles," *IEEE Transactions on Vehicular Technology*, vol. 57, no. 6, pp. 3369–3380, Nov 2008.

[52] G. Van Dooren, M. Klaassen, and M. Herben, "Measurement of Diffracted Electromagnetic Fields Behind A Thin Finite-width Screen," *Electronics Letters*, vol. 28, no. 19, pp. 1845–1847, Sept 1992.

[53] F. Schwering, E. Violette, and R. Espeland, "Millimeter-Wave Propagation In Vegetation: Experiments And Theory," *IEEE Transactions on Geoscience and Remote Sensing*, vol. 26, no. 3, pp. 355–367, May 1988.

[54] K. Haneda, J. Jarvelainen, A. Karttunen, M. Kyro, and J. Putkonen, "A Statistical Spatio-Temporal Radio Channel Model for Large Indoor Environments at 60 and 70 GHz," *IEEE Transactions on Antennas and Propagation*, vol. 63, no. 6, pp. 2694–2704, June 2015.

[55] G. R. Maccartney, T. S. Rappaport, M. K. Samimi, and S. Sun, "Millimeter-Wave Omnidirectional Path Loss Data for Small Cell 5G Channel Modeling," *IEEE Access*, vol. 3, pp. 1573–1580, 2015.

[56] V. Kvicera, M. Grabner, and O. Fiser, "Frequency And Path Length Scaling Of Rain Attenuation From 38 GHz, 58 GHz And 93 GHz Data Obtained On Terrestrial Paths," in *3rd European Conference on Antennas and Propagation (EuCAP)*, March 2009, pp. 2648–2652. [Online]. Available: http://ieeexplore.ieee.org/xpls/abs_all.jsp?arnumber=5068156

[57] Y. Azar, G. Wong, K. Wang, R. Mayzus, J. Schulz, H. Zhao, F. Gutierrez, D. Hwang, and T. Rappaport, "28 GHz Propagation Measurements For Outdoor Cellular Communications Using Steerable Beam Antennas In New York City," in *IEEE International Conference on Communications (ICC)*, June 2013, pp. 5143–5147.

[58] H. Zhao, R. Mayzus, S. Sun, M. Samimi, J. Schulz, Y. Azar, K. Wang, G. Wong, F. Gutierrez, and T. Rappaport, "28 GHz Millimeter Wave

Cellular Communication Measurements For Reflection And Penetration Loss In And Around Buildings In New York City," in *IEEE International Conference on Communications (ICC)*, June 2013, pp. 5163–5167.

[59] M. Samimi, K. Wang, Y. Azar, G. Wong, R. Mayzus, H. Zhao, J. Schulz, S. Sun, F. Gutierrez, and T. Rappaport, "28 GHz Angle of Arrival and Angle of Departure Analysis for Outdoor Cellular Communications Using Steerable Beam Antennas in New York City," in *Vehicular Technology Conference (VTC Spring), IEEE 77th*, June 2013, pp. 1–6.

[60] P. Tenerelli and C. Bostian, "Measurements of 28 GHz Diffraction Loss by Building Corners," in *The Ninth IEEE International Symposium on Personal, Indoor and Mobile Radio Communications*, vol. 3, Sep 1998, pp. 1166–1169 vol.3.

[61] P. Soma, L. C. Ong, S. Sun, and M. Chia, "Propagation measurements and modeling of LMDS radio channel in Singapore," *IEEE Transactions on Vehicular Technology*, vol. 52, no. 3, pp. 595–606, May 2003.

[62] J. Murdock, E. Ben-Dor, Y. Qiao, J. Tamir, and T. Rappaport, "A 38 GHz Cellular Outage Study For An Urban Outdoor Campus Environment," in *Wireless Communications and Networking Conference (WCNC), IEEE*, April 2012, pp. 3085–3090.

[63] H. Xu, T. Rappaport, R. Boyle, and J. Schaffner, "Measurements And Models for 38-GHz Point-to-Multipoint Radiowave Propagation," *IEEE Journal on Selected Areas in Communications*, vol. 18, no. 3, pp. 310–321, March 2000.

[64] S. Nie, G. R. MacCartney, S. Sun, and T. S. Rappaport, "72 GHz Millimeter Wave Indoor Measurements For Wireless And Backhaul Communications," in *International Symposium on Personal Indoor and Mobile Radio Communications (PIMRC), IEEE 24th*, Sept 2013, pp. 2429–2433.

[65] C. L. Cheng, S. Kim, and A. Zajic, "Comparison of Path Loss Models For Indoor 30 GHz, 140 GHz, And 300 GHz Channels," in *11th European Conference on Antennas and Propagation (EUCAP)*, March 2017, pp. 716–720.

[66] M.-S. Choi, G. Grosskopf, and D. Rohde, "Statistical Characteristics of 60 GHz Wideband Indoor Propagation Channel," in *Personal, Indoor and Mobile Radio Communications, 2005. PIMRC 2005. IEEE 16th International Symposium on*, vol. 1, Sept 2005, pp. 599–603.

[67] H. Sawada, Y. Shoji, and C.-S. Choi, "Proposal Of Novel Statistic Channel Model For Millimeter Wave WPAN," in *Microwave Conference, APMC. Asia-Pacific*, Dec 2006, pp. 1855–1858.

[68] Y. Zhang, O. Edfors, P. Hammarberg, T. Hult, X. Chen, S. Zhou, L. Xiao, and J. Wang, "A General Coupling-Based Model Framework for Wideband MIMO Channels," *IEEE Transactions on Antennas and Propagation*, vol. 60, no. 2, pp. 574–586, Feb 2012.

[69] C. Gustafson, K. Haneda, S. Wyne, and F. Tufvesson, "On mm-Wave Multipath Clustering and Channel Modeling," *IEEE Transactions on Antennas and Propagation*, vol. 62, no. 3, pp. 1445–1455, March 2014.

[70] Y. Takimoto, "Recent Activities on Millimeter Wave Indoor LAN System Development in Japan," in *Proceedings of IEEE MTT-S International Microwave Symposium*, May 1995, pp. 405–408 vol.2.

[71] A. Bleicher. (2013, June) Telecom Wireless News Millimeter Waves May Be the Future of 5G Phones. [Online]. Available: http://spectrum.ieee.org/telecom/wireless/millimeter-waves-may-be-the-future-of-5g-phones

[72] M. K. Samimi and T. S. Rappaport, "Local Multipath Model Parameters for Generating 5G Millimeter-Wave 3GPP-Like Channel Impulse Response," in *10th European Conference on Antennas and Propagation (EuCAP)*, April 2016, pp. 1–5.

[73] mmMAGIC. (2015, July) 6-100 GHz Channel Modelling for 5G: Measurement and Modelling Plans in mmMAGIC. European Commission H2020. [Online]. Available: https://5g-mmmagic.eu/results/#deliverables

[74] ——. (2016, April) Architectural Aspects of mm-wave Radio Access Integration With 5G Ecosystem. European Commission H2020. [Online]. Available: https://5g-mmmagic.eu/results/#deliverables

[75] P. Pietraski, D. Britz, A. Roy, R. Pragada, and G. Charlton, "millimeter Wave And Terahertz Communications: Feasibility And Challenges," *ZTE Communications*, vol. 4, no. 4, pp. 3–12, Dec 2012. [Online]. Available: http://wwwen.zte.com.cn/endata/magazine/ztecommunications/2012/4/articles/201301/t20130106_380442.html

[76] M. Samimi and T. Rappaport, "Ultra-Wideband Statistical Channel Model for Non Line of Sight Millimeter-Wave Urban Channels," in *Global Communications Conference (GLOBECOM), IEEE*, Dec 2014, pp. 3483–3489.

[77] G. MacCartney, T. Rappaport, M. Samimi, and S. Sun, "Wideband Millimeter-Wave Propagation Measurements and Channel Models for

[78] G. Maccartney, M. Samimi, and T. Rappaport, "Exploiting Directionality For Millimeter-wave Wireless System Improvement," in *IEEE International Conference on Communications (ICC)*, June 2015, pp. 2416–2422.

[79] M. K. Samimi, S. Sun, and T. S. Rappaport, "MIMO Channel Modeling and Capacity Analysis for 5G Millimeter-Wave Wireless Systems," *CoRR*, vol. abs/1511.06940, 2015. [Online]. Available: http://arxiv.org/abs/1511.06940

[80] M. K. Samimi and T. S. Rappaport, "28 GHz Millimeter-Wave Ultrawideband Small-Scale Fading Models in Wireless Channels," *CoRR*, vol. abs/1511.06938, 2015. [Online]. Available: http://arxiv.org/abs/1511.06938

[81] A. Swindlehurst, E. Ayanoglu, P. Heydari, and F. Capolino, "Millimeter-Wave Massive MIMO: The Next Wireless RevolutMIMO," *Communications Magazine, IEEE*, vol. 52, no. 9, pp. 56–62, September 2014.

[82] S. Rangan, T. Rappaport, and E. Erkip, "Millimeter-Wave Cellular Wireless Networks: Potentials and Challenges," *Proceedings of the IEEE*, vol. 102, no. 3, pp. 366–385, March 2014.

[83] E. Torkildson, U. Madhow, and M. Rodwell, "Indoor Millimeter Wave MIMO: Feasibility and Performance," *IEEE Transactions on Wireless Communications*, vol. 10, no. 12, pp. 4150–4160, December 2011.

[84] J. Blogh and L. Hanzo, *Third-Generation Systems and Intelligent Wireless Networking: Smart Antennas and Adaptive Modulation*. Wiley, 2002. [Online]. Available: http://books.google.co.uk/books?id=CUZNkh4QRtoC

[85] L. Hanzo, M. El-Hajjar, and O. Alamri, "Near-Capacity Wireless Transceivers and Cooperative Communications in the MIMO Era: Evolution of Standards, Waveform Design, and Future Perspectives," *Proceedings of the IEEE*, vol. 99, no. 8, pp. 1343–1385, Aug 2011.

[86] W. bin Abbas, F. Gómez-Cuba, and M. Zorzi, "Bit Allocation for Increased Power Efficiency in 5G Receivers with Variable-Resolution ADCs," *CoRR*, vol. abs/1610.09546, 2016. [Online]. Available: http://arxiv.org/abs/1610.09546

[87] K.-J. Koh, J. May, and G. Rebeiz, "A Millimeter-Wave (40-45 GHz) 16-Element Phased-Array Transmitter in 0.18-μm SiGe BiCMOS Technology," *IEEE Journal of Solid-State Circuits*, vol. 44, no. 5, pp. 1498–1509, May 2009.

[88] B. Razavi, "A 60-GHz CMOS Receiver Front-End," *IEEE Journal of Solid-State Circuits*, vol. 41, no. 1, pp. 17–22, Jan 2006.

[89] H. Hashemi, X. Guan, A. Komijani, and A. Hajimiri, "A 24-GHz SiGe Phased-Array Receiver-LO Phase-Shifting Approach," *IEEE Transactions on Microwave Theory and Techniques*, vol. 53, no. 2, pp. 614–626, Feb 2005.

[90] X. Huang, Y. Guo, and J. Bunton, "A Hybrid Adaptive Antenna Array," *IEEE Transactions on Wireless Communications*, vol. 9, no. 5, pp. 1770–1779, May 2010.

[91] J. Nsenga, A. Bourdoux, and F. Horlin, "Mixed Analog/Digital Beamforming for 60 GHz MIMO Frequency Selective Channels," in *IEEE International Conference on Communications (ICC)*, May 2010, pp. 1–6.

[92] S. Kutty and D. Sen, "Beamforming for Millimeter Wave Communications: An Inclusive Survey," *IEEE Communications Surveys Tutorials*, vol. 18, no. 2, pp. 949–973, Secondquarter 2016.

[93] R. Daniels, J. Murdock, T. Rappaport, and R. Heath, "60 GHz Wireless: Up Close and Personal," *Microwave Magazine, IEEE*, vol. 11, no. 7, pp. 44–50, Dec 2010.

[94] J. S. Lu, D. Steinbach, P. Cabrol, and P. Pietraski, "Modeling Human Blockers in Millimeter Wave Radio Links," *ZTE Communications*, vol. 4, no. 4, pp. 23–28, Dec 2012. [Online]. Available: http://wwwen.zte.com.cn/endata/magazine/ztecommunications/2012/4/articles/201301/t20130106_380446.html

[95] S. Seidel and H. Arnold, "Propagation Measurements At 28 GHz To Investigate The Performance Of Local Multipoint Distribution Service (LMDS)," in *Global Telecommunications Conference, GLOBECOM, IEEE*, vol. 1, Nov 1995, pp. 754–757 vol.1.

[96] A. Elrefaie and M. Shakouri, "Propagation Measurements at 28 GHz for Coverage Evaluation of Local Multipoint Distribution Service," in *Proceedings Wireless Communications Conference*, Aug 1997, pp. 12–17.

[97] P. Papazian, G. A. Hufford, R. Achatz, and R. Hoffman, "Study Of The Local Multipoint Distribution Service Radio Channel," *IEEE Transactions on Broadcasting*, vol. 43, no. 2, pp. 175–184, Jun 1997.

[98] T. Rappaport, G. Maccartney, M. Samimi, and S. Sun, "Wideband Millimeter-Wave Propagation Measurements and Channel Models for

Future Wireless Communication System Design," *IEEE Transactions on Communications*, vol. 63, no. 9, pp. 3029–3056, Sept 2015.

[99] T. Rappaport and S. Deng, "73 GHz Wideband Millimeter-Wave Foliage And Ground Reflection Measurements And Models," in *IEEE International Conference on Communication Workshop (ICCW)*, June 2015, pp. 1238–1243.

[100] S. Sun, T. Rappaport, T. Thomas, and A. Ghosh, "A Preliminary 3D MM-Wave Indoor Office Channel Model," in *2015 International Conference on Computing, Networking and Communications (ICNC)*, Feb 2015, pp. 26–31.

[101] T. Wu, T. Rappaport, and C. Collins, "Safe for Generations to Come: Considerations of Safety for Millimeter Waves in Wireless Communications," *Microwave Magazine, IEEE*, vol. 16, no. 2, pp. 65–84, March 2015.

[102] ——, "The Human Body And Millimeter-Wave Wireless Communication Systems: Interactions And Implications," in *IEEE International Conference on Communications (ICC)*, June 2015, pp. 2423–2429.

[103] S. Hur, S. Baek, B. Kim, Y. Chang, A. F. Molisch, T. S. Rappaport, K. Haneda, and J. Park, "Proposal on Millimeter-Wave Channel Modeling for 5G Cellular System," *IEEE Journal of Selected Topics in Signal Processing*, vol. 10, no. 3, pp. 454–469, April 2016.

[104] S. Deng, M. Samimi, and T. Rappaport, "28 GHz And 73 GHz Millimeter-Wave Indoor Propagation Measurements And Path Loss Models," in *IEEE International Conference on Communication Workshop (ICCW)*, June 2015, pp. 1244–1250.

[105] M. K. Samimi and T. S. Rappaport, "Statistical Channel Model with Multi-Frequency and Arbitrary Antenna Beamwidth for Millimeter-Wave Outdoor Communications," in *2015 IEEE Globecom Workshops (GC Wkshps)*, Dec 2015, pp. 1–7.

[106] G. R. MacCartney and T. S. Rappaport, "A Flexible Millimeter-Wave Channel Sounder with Absolute Timing," *IEEE Journal on Selected Areas in Communications*, vol. PP, no. 99, pp. 1–1, 2017.

[107] A. Nashashibi, K. Sarabandi, S. Oveisgharan, M. Dobson, W. Walker, and E. Burke, "Millimeter-Wave Measurements Of Foliage Attenuation And Ground Reflectivity Of Tree Stands At Nadir Incidence," *IEEE Transactions on Antennas and Propagation*, vol. 52, no. 5, pp. 1211–1222, May 2004.

[108] F. Wang and K. Sarabandi, "An Enhanced Millimeter-Wave Foliage Propagation Model," *IEEE Transactions on Antennas and Propagation*, vol. 53, no. 7, pp. 2138–2145, July 2005.

[109] T. Rappaport, Y. Qiao, J. Tamir, J. Murdock, and E. Ben-Dor, "Cellular Broadband Millimeter Wave Propagation And Angle Of Arrival For Adaptive Beam Steering Systems (Invited Paper)," in *Radio and Wireless Symposium (RWS), 2012 IEEE*, Jan 2012, pp. 151–154.

[110] A. Sulyman, A. Nassar, M. Samimi, G. MacCartney, T. Rappaport, and A. Alsanie, "Radio Propagation Path Loss Models For 5G Cellular Networks In The 28 GHz And 38 GHz Millimeter-Wave Bands," *Communications Magazine, IEEE*, vol. 52, no. 9, pp. 78–86, September 2014.

[111] G. Kalivas, M. El-Tanany, and S. Mahmoud, "Millimeter-wave channel measurements with space diversity for indoor wireless communications," *IEEE Transactions on Vehicular Technology*, vol. 44, no. 3, pp. 494–505, Aug 1995.

[112] R. J. C. Bultitude, R. Hahn, and R. Davies, "Propagation Considerations for The Design of an Indoor Broad-Band Communications System at EHF," *IEEE Transactions on Vehicular Technology*, vol. 47, no. 1, pp. 235–245, Feb 1998.

[113] I. Cuinas, M. Garcia Sanchez, and E. Amoedo, "Modeling and Measuring Depolarization by Building Obstacles in The 41.5 GHz Band," *Microwave and Optical Technology Letters*, vol. 24, no. 1, pp. 34–36, 2000.

[114] S. Collonge, G. Zaharia, and G. E. Zein, "Experimental Investigation of The Spatial And Temporal Characteristics of The 60 GHz Radio Propagation Within Residential Environments," in *International Symposium on Signals, Circuits and Systems*, vol. 2, 2003, pp. 417–420 vol.2.

[115] B. Langen, G. Lober, and W. Herzig, "Reflection And Transmission Behaviour of Building Materials at 60 GHz," in *5th IEEE International Symposium on Personal, Indoor and Mobile Radio Communications. Wireless Networks - Catching the Mobile Future.,*, Sep 1994, pp. 505–509 vol.2.

[116] P. Smulders and A. Wagemans, "Wideband indoor radio propagation measurements at 58 GHz," *Electronics Letters*, vol. 28, no. 13, pp. 1270–1272, June 1992.

[117] H. Droste and G. Kadel, "Measurement And Analysis of Wide Band Indoor Propagation Characteristics at 17 GHz And 60 GHz," in *Ninth*

International Conference on Antennas and Propagation (Conf. Publ. No. 407), vol. 2, Apr 1995, pp. 288–291 vol.2.

[118] P. F. M. Smulders and A. Wagemans, "Frequency-domain measurement of the millimeter wave indoor radio channel," *IEEE Transactions on Instrumentation and Measurement*, vol. 44, no. 6, pp. 1017–1022, Dec 1995.

[119] K. Sato, T. Manabe, T. Ihara, H. Saito, S. Ito, T. Tailaka, K. Sugai, N. Ohmi, Y. Murakami, M. Shibayama, Y. Konishi, and T. Kimura, "Measurements of Reflection And Transmission Characteristics of Interior Structures Of Office Building In The 60 GHz Band," in *Seventh IEEE International Symposium on Personal, Indoor and Mobile Radio Communications (PIMRC)*, vol. 1, Oct 1996, pp. 14–18 vol.1.

[120] J. Kunisch, E. Zollinger, J. Pamp, and A. Winkelmann, "MEDIAN 60 GHz wideband indoor radio channel measurements and model," in *Vehicular Technology Conference (VTC), IEEE VTS 50th*, vol. 4, Fall 1999, pp. 2393–2397 vol.4.

[121] A. Hammoudeh, D. Scammell, and M. Sanchez, "Measurements and analysis of the indoor wideband millimeter wave wireless radio channel and frequency diversity characterization," *IEEE Transactions on Antennas and Propagation*, vol. 51, no. 10, pp. 2974–2986, Oct 2003.

[122] C. Anderson and T. Rappaport, "In-Building Wideband Partition Loss Measurements at 2.5 And 60 GHz," *IEEE Transactions on Wireless Communications*, vol. 3, no. 3, pp. 922–928, May 2004.

[123] S. Ranvier, J. Kivinen, and P. Vainikainen, "Millimeter-Wave MIMO Radio Channel Sounder," *IEEE Transactions on Instrumentation and Measurement*, vol. 56, no. 3, pp. 1018–1024, June 2007.

[124] R. Tahri, S. Collonge, G. Zaharia, and G. E. Zein, "Spatial Characterization of 60 GHz Indoor Channels by Fast Gaussian Beam Tracking Method and Comparison with Measurements," in *Vehicular Technology Conference, VTC Spring. IEEE 63rd*, vol. 6, May 2006, pp. 2722–2726.

[125] S. Geng, J. Kivinen, X. Zhao, and P. Vainikainen, "Millimeter-Wave Propagation Channel Characterization for Short-Range Wireless Communications," *IEEE Transactions on Vehicular Technology*, vol. 58, no. 1, pp. 3–13, Jan 2009.

[126] H. Xu, V. Kukshya, and T. S. Rappaport, "Spatial And Temporal Characterization of 60 GHz Indoor Channels," in *Vehicular Technology Conference, IEEE-VTS Fall VTC . 52nd*, vol. 1, 2000, pp. 6–13 vol.1.

[127] J. Ryan, G. R. MacCartney, and T. S. Rappaport, "Indoor Office Wideband Penetration Loss Measurements at 73 GHz," in *2017 IEEE International Conference on Communications Workshops (ICC Workshops)*, May 2017, pp. 228–233.

[128] J. Hansryd, Y. Li, J. Chen, and P. Ligander, "Long Term Path Attenuation Measurement of the 71-76 GHz Band in a 70/80 GHz Microwave Link," in *Proceedings of the Fourth European Conference on Antennas and Propagation (EuCAP)*, April 2010, pp. 1–4. [Online]. Available: http://ieeexplore.ieee.org/xpl/articleDetails.jsp?tp=&arnumber=5505467&queryText%3DLong+term+path+attenuation+measurement+of+the+71-76+GHz+band+in+%09a+70%2F80+GHz+microwave+link

[129] J. Walfisch and H. L. Bertoni, "A theoretical model of uhf propagation in urban environments," *IEEE Transactions on Antennas and Propagation*, vol. 36, no. 12, pp. 1788–1796, Dec 1988.

[130] M. Marcus and B. Pattan, "Millimeter Wave Propagation; Spectrum Management Implications," *Microwave Magazine, IEEE*, vol. 6, no. 2, pp. 54–62, June 2005.

[131] H. T. Friis, "A Note on a Simple Transmission Formula," in *Proceedings of the IRE*, May 1946, pp. 254–256.

[132] W. Gosling, *Radio Antennas and Propagation*, 1st ed. Newnes, 1998.

[133] ITU-R. (2013, Sep) Attenuation by atmospheric gases, P.676-10. International Telecommunication Union (ITU), Radiocommunication Sector. Geneva, Switzerland. [Online]. Available: http://www.itu.int/rec/R-REC-P.676-10-201309-I/en

[134] ——. (2005, Mar) Specific attenuation model for rain for use in prediction methods, P.838-3. International Telecommunication Union (ITU), Radiocommunication Sector. Geneva, Switzerland. [Online]. Available: http://www.itu.int/rec/R-REC-P.838-3-200503-I/en

[135] ——. (2012, Feb) Characteristics of precipitation for propagation modelling, P.837-6. International Telecommunication Union (ITU), Radiocommunication Sector. Geneva, Switzerland. [Online]. Available: http://www.itu.int/rec/R-REC-P.837/en

[136] J. S. Mandeep, O. W. Hui, M. Abdullah, M. Tariqul, M. Ismail, W. Suparta, B. Yatim, P. Menon, and H. Abdullah, "Modified ITU-R Rain Attenuation Model For Equatorial Climate," in *IEEE International Conference on Space Science and Communication (IconSpace)*, July 2011, pp. 89–92.

[137] M. S. J. Singh, S. I. S. Hassan, M. F. Ain, F. Ghani, K. Igarashi, K. Tanaka, and M. Iida, "Rain Attenuation Model For South East Asia Countries," *Electronics Letters*, vol. 43, no. 2, pp. 75–77, January 2007.

[138] ITU-R. (2013, Sep) Attenuation in vegetation, ITU-R P.833-8. International Telecommunication Union (ITU), Radiocommunication Sector. Geneva, Switzerland. [Online]. Available: http://www.itu.int/rec/R-REC-P.833/en

[139] M. A. Weissberger, "An Initial Critical Summary Of Models For Predicting The Attenuation Of Radio Waves By Foliage," ELECTROMAGNETIC COMPATIBILITY ANALYSIS CENTER (ECAC), ANNAPOLIS, MARYLAND 21402, Tech. Rep., July 1982. [Online]. Available: www.dtic.mil/cgi-bin/GetTRDoc?AD=ADA118343

[140] Y. S. Meng and Y. H. Lee, "Investigations Of Foliage Effect On Modern Wireless Communication Systems: A Review," *Progress In Electromagnetics Research*, vol. 105, pp. 313–332, 2010. [Online]. Available: http://www.jpier.org/pier/pier.php?paper=10042605

[141] J. Laneman, D. Tse, and G. W. Wornell, "Cooperative Diversity In Wireless Networks: Efficient Protocols And Outage Behavior," *IEEE Transactions on Information Theory*, vol. 50, no. 12, pp. 3062–3080, Dec 2004.

[142] H. Xu, V. Kukshya, and T. Rappaport, "Spatial And Temporal Characteristics of 60-GHz Indoor Channels," *IEEE Journal on Selected Areas in Communications*, vol. 20, no. 3, pp. 620–630, Apr 2002.

[143] A. K. M. Isa, A. Nix, and G. Hilton, "Impact of Diffraction And Attenuation for Material Characterisation in Millimetre Wave Bands," in *Loughborough Antennas Propagation Conference (LAPC)*, Nov 2015, pp. 1–4.

[144] A. Damnjanovic, J. Montojo, Y. Wei, T. Ji, T. Luo, M. Vajapeyam, T. Yoo, O. Song, and D. Malladi, "A Survey on 3GPP Heterogeneous Networks," *Wireless Communications, IEEE*, vol. 18, no. 3, pp. 10–21, June 2011.

[145] S. Deng, G. R. MacCartney, and T. S. Rappaport, "Indoor and Outdoor 5G Diffraction Measurements and Models at 10, 20, and 26 GHz," in *IEEE Global Communications Conference (GLOBECOM)*, Dec 2016, pp. 1–7.

[146] J. Senic, C. Gentile, P. B. Papazian, K. A. Remley, and J. K. Choi, "Analysis of E-band Path Loss and Propagation Mechanisms in the Indoor Environment," *IEEE Transactions on Antennas and Propagation*, vol. PP, no. 99, pp. 1–1, 2017.

[147] A. Maltsev, I. Bolotin, A. Pudeyev, G. Morozov, and A. Davydov, "Performance Evaluation of The Isolated mmWave Small Cell," in *26th Annual International Symposium on Personal, Indoor, and Mobile Radio Communications, IEEE*, Aug 2015, pp. 2354–2358.

[148] S. Collonge, G. Zaharia, and G. Zein, "Influence of The Human Activity on Wide-band Characteristics of The 60 GHz Indoor Radio Channel," *IEEE Transactions on Wireless Communications*, vol. 3, no. 6, pp. 2396–2406, Nov 2004.

[149] T. Jamsa, "Deliverable D1.4 METIS Channel Models," METIS, Tech. Rep., Feb 2015. [Online]. Available: https://www.metis2020.com/wp-content/uploads/METIS_D1.4_v3.pdf

[150] G. R. MacCartney, S. Deng, S. Sun, and T. S. Rappaport, "Millimeter-Wave Human Blockage at 73 GHz with a Simple Double Knife-Edge Diffraction Model and Extension for Directional Antennas," in *IEEE 84th Vehicular Technology Conference (VTC-Fall)*, Sept 2016, pp. 1–6.

[151] P. Almers, E. Bonek, A. Burr, N. Czink, M. Debbah, V. Degli Esposti, H. Hofstetter, P. Kyösti, D. Laurenson, G. Matz, A. F. Molisch, C. Oestges, and H. Özcelik, "Survey of Channel and Radio Propagation Models for Wireless MIMO Systems," *EURASIP Journal on Wireless Communications and Networking Volume 2007, Article ID 19070*, 02 2007. [Online]. Available: https://www.eurecom.fr/publication/2162

[152] R. Steele, *Mobile Radio Communications*. Piscataway, NJ, USA: IEEE Press, 1994.

[153] D.-S. Shiu, G. J. Faschini, M. J. Gans, and J. M. Kahn, "Fading Correlation And Its Effect on The Capacity of Multi-Element Antenna Systems," in *International Conference on Universal Personal Communications, (ICUPC)*, vol. 1, Oct 1998, pp. 429–433 vol.1.

[154] C.-N. Chuah, J. M. Kahn, and D. Tse, "Capacity of Multi-Antenna Array Systems in Indoor Wireless Environment," in *IEEE GLOBECOM*, vol. 4, 1998, pp. 1894–1899 vol.4.

[155] W. Weichselberger, M. Herdin, H. Ozcelik, and E. Bonek, "A Stochastic MIMO Channel Model With Joint Correlation of Both Link Ends," *IEEE Transactions on Wireless Communications*, vol. 5, no. 1, pp. 90–100, Jan 2006.

[156] A. G. Burr, "capacity Bounds And Estimates For The Finite Scatterers MIMO Wireless Channel," *IEEE Journal on Selected Areas in Communications*, vol. 21, no. 5, pp. 812–818, June 2003.

[157] M. Debbah and R. R. Muller, "MIMO Channel Modeling And The Principle Of Maximum Entropy," *IEEE Transactions on Information Theory*, vol. 51, no. 5, pp. 1667–1690, May 2005.

[158] A. M. Sayeed, "Deconstructing Multiantenna Fading Channels," *IEEE Transactions on Signal Processing*, vol. 50, no. 10, pp. 2563–2579, Oct 2002.

[159] J. McKown and J. Hamilton, R.L., "ray Tracing As A Design Tool For Radio Networks," *Network, IEEE*, vol. 5, no. 6, pp. 27–30, Nov 1991.

[160] P. Marinier, G. Delisle, and L. Talbi, "A Coverage Prediction Technique For Indoor Wireless Millimeter Waves System," *Wireless Personal Communications*, vol. 3, no. 3, pp. 257–271, 1996. [Online]. Available: http://dx.doi.org/10.1007/BF00354874

[161] V. Mohtashami and A. Shishegar, "efficient Shooting And Bouncing Ray Tracing Using Decomposition f Wavefronts," *Microwaves, Antennas Propagation, IET*, vol. 4, no. 10, pp. 1567–1574, October 2010.

[162] D. Dardari, L. Minelli, V. Tralli, and O. Andrisano, "Fast Ray-Tracing Characterisation of Indoor Propagation Channels at 60 GHz," in *Vehicular Technology Conference, IEEE 47th*, vol. 2, May 1997, pp. 989–993 vol.2.

[163] P. Charriere, K. H. Craig, and A. Seville, "A Ray-Based, Millimetre Wave Urban Propagation Tool," in *Ninth International Conference on Antennas and Propagation (Conf. Publ. No. 407)*, vol. 2, Apr 1995, pp. 258–261 vol.2.

[164] B. Neekzad, K. Sayrafian-Pour, J. Perez, and J. Baras, "Comparison of Ray Tracing Simulations and Millimeter Wave Channel Sounding Measurements," in *IEEE 18th International Symposium on Personal, Indoor and Mobile Radio Communications (PIMRC)*, Sept 2007, pp. 1–5.

[165] H. Yang, M. H. A. J. Herben, and P. F. M. Smulders, "Indoor Radio Channel Fading Analysis via Deterministic Simulations at 60 GHz," in *Wireless Communication Systems, 2006. ISWCS '06. 3rd International Symposium on*, Sept 2006, pp. 144–148.

[166] W. Peter, W. Keusgen, and R. Felbecker, "Measurement And Ray-Tracing Simulation of The 60 GHz Indoor Broadband Channel: Model Accuracy And Parameterization," in *The Second European Conference on Antennas and Propagation (EuCAP)*, Nov 2007, pp. 1–8. [Online]. Available: http://ieeexplore.ieee.org/xpl/articleDetails.jsp?tp=&arnumber=4458680&queryText%3DMeasurement+and+Ray-Tracing+Simulation+of+the+60+GHz+Indoor+Broadband+Channel%3A+Model+Accuracy+and+Parameterization

[167] M. Kazemi, A. Abdipur, and A. Mohammadi, "Indoor Propagation MIMO Channel Modeling in 60 GHz Using SBR Based 3D Ray Tracing Technique," in *Second Conference on Millimeter-Wave and Terahertz Technologies (MMWaTT)*, Dec 2012, pp. 25–28.

[168] R. Hoppe, J. Ramuh, H. Buddendick, O. Stabler, and G. Wolfle, "Comparison of MIMO Channel Characteristics Computed by 3D Ray Tracing and Statistical Models," in *The Second European Conference on Antennas and Propagation (EuCAP)*, Nov 2007, pp. 1–5. [Online]. Available: http://ieeexplore.ieee.org/xpls/abs_all.jsp?arnumber=4458770&tag=1

[169] S. Ali, S. Qu, F. Kohandani, and P. Lusina, "Deterministic and Statistical-Based Channel Models in the MIMO Link Evaluation," *IEEE Antennas and Wireless Propagation Letters*, vol. 8, pp. 927–930, 2009.

[170] 3GPP, "Further Advancements for E-UTRA Physical Layer Aspects," 3rd Generation Partnership Project, Tech. Rep., Mar 2010. [Online]. Available: http://www.3gpp.org/DynaReport/36814.htm

[171] A. A. M. Saleh and R. Valenzuela, "A Statistical Model for Indoor Multipath Propagation," *IEEE Journal on Selected Areas in Communications*, vol. 5, no. 2, pp. 128–137, February 1987.

[172] J. Wallace and M. Jensen, "Modeling The Indoor MIMO Wireless Channel," *IEEE Transactions on Antennas and Propagation*, vol. 50, no. 5, pp. 591–599, May 2002.

[173] T. Zwick, C. Fischer, and W. Wiesbeck, "A Stochastic Multipath Channel Model Including Path Directions For Indoor Environments," *IEEE Journal on Selected Areas in Communications*, vol. 20, no. 6, pp. 1178–1192, Aug 2002.

[174] D. Baum, J. Hansen, and J. Salo, "An Interim Channel Model for Beyond-3G Systems: Extending The 3GPP Spatial Channel Model (SCM)," in *Vehicular Technology Conference, 2005. VTC 2005-Spring. 2005 IEEE 61st*, vol. 5, May 2005, pp. 3132–3136 Vol. 5.

[175] N. Moraitis and P. Constantinou, "Indoor Channel Modeling At 60 GHz For Wireless LAN Applications," in *The 13th IEEE International Symposium on Personal, Indoor and Mobile Radio Communications*, vol. 3, Sept 2002, pp. 1203–1207 vol.3.

[176] D. Cassioli, "UWB Moves up to mmWaves: A channel modeling perspective," in *Ultra-Wideband (ICUWB), 2011 IEEE International Conference on*, Sept 2011, pp. 521–525.

[177] J. Nam, A. Adhikary, J.-Y. Ahn, and G. Caire, "Joint Spatial Division and Multiplexing: Opportunistic Beamforming, User Grouping and Simplified Downlink Scheduling," *IEEE Journal of Selected Topics in Signal Processing*, vol. 8, no. 5, pp. 876–890, Oct 2014.

[178] A. Adhikary, E. Al Safadi, M. Samimi, R. Wang, G. Caire, T. Rappaport, and A. Molisch, "Joint Spatial Division and Multiplexing for mm-Wave Channels," *IEEE Journal on Selected Areas in Communications*, vol. 32, no. 6, pp. 1239–1255, June 2014.

[179] T. Manabe, Y. Miura, and T. Ihara, "Effects Of Antenna Directivity And Polarization On Indoor Multipath Propagation Characteristics At 60 GHz," *IEEE Journal on Selected Areas in Communications*, vol. 14, no. 3, pp. 441–448, Apr 1996.

[180] S. Sun and T. Rappaport, "Wideband mmwave Channels: Implications For Design And Implementation Of Adaptive Beam Antennas," in *Microwave Symposium (IMS), 2014 IEEE MTT-S International*, June 2014, pp. 1–4.

[181] S. Sun, G. MacCartney, M. Samimi, S. Nie, and T. Rappaport, "Millimeter Wave Multi-beam Antenna Combining for 5G Cellular Link Improvement in New York City," in *IEEE International Conference on Communications (ICC)*, June 2014, pp. 5468–5473.

[182] R. J. Weiler, M. Peter, W. Keusgen, H. Shimodaira, K. T. Gia, and K. Sakaguchi, "Outdoor Millimeter-Wave Access For Heterogeneous Networks - 2014; Path Loss And System Performance," in *Annual International Symposium on Personal, Indoor, and Mobile Radio Communication (PIMRC),IEEE 25th*, Sept 2014, pp. 2189–2193.

[183] C. Dehos, J. Gonzalez, A. De Domenico, D. Ktens, and L. Dussopt, "Millimeter-Wave Access And Backhauling: The Solution To The Exponential Data Traffic Increase In 5G Mobile Communications Systems?" *Communications Magazine, IEEE*, vol. 52, no. 9, pp. 88–95, September 2014.

[184] A. Maltsev, R. Maslennikov, A. Sevastyanov, A. Lomayev, and A. Khoryaev, "Statistical Channel Model for 60 GHz WLAN Systems in Conference Room Environment," in *Proceedings of the Fourth European Conference on Antennas and Propagation (EuCAP)*, April 2010, pp. 1–5.

[185] K. Haneda, C. Gustafson, and S. Wyne, "60 GHz Spatial Radio Transmission: Multiplexing or Beamforming?" *IEEE Transactions on Antennas and Propagation*, vol. 61, no. 11, pp. 5735–5743, Nov 2013.

[186] J. Dou, L. Tian, H. Wang, X. Yuan, N. Zhang, and S. Mei, "45GHz Propagation Channel Modeling for an Indoor Conference Scenario," in *IEEE 26th Annual International Symposium on Personal, Indoor, and Mobile Radio Communications (PIMRC)*, Aug 2015, pp. 2225–2228.

[187] WINNER. (2007, Sep) IST-4-027756 WINNER II interim channel models. [Online]. Available: http://www.ist-winner.org/deliverables.html

[188] P. Heino. (2010, Jun) D5.3: WINNER+ Final Channel Models. [Online]. Available: http://projects.celtic-initiative.org/winner+/deliverables_winnerplus.html

[189] MiWEBA, "D5.1: Channel Modeling and Characterization," MiWEBA, Report, Jun 2014. [Online]. Available: http://www.miweba.eu/wp-content/uploads/2014/07/MiWEBA_D5.1_v1.011.pdf

[190] T. S. Rappaport, Y. Xing, G. R. MacCartney, A. F. Molisch, E. Mellios, and J. Zhang, "Overview of Millimeter Wave Communications for Fifth-Generation (5G) Wireless Networks-with a focus on Propagation Models," *IEEE Transactions on Antennas and Propagation*, vol. PP, no. 99, pp. 1–1, 2017.

[191] J. Medbo, K. Borner, K. Haneda, V. Hovinen, T. Imai, J. Jarvelainen, T. Jamsa, A. Karttunen, K. Kusume, J. Kyrolainen, P. Kyosti, J. Meinila, V. Nurmela, L. Raschkowski, A. Roivainen, and J. Ylitalo, "Channel Modelling For The Fifth Generation Mobile Communications," in *The 8th European Conference on Antennas and Propagation (EuCAP 2014)*, April 2014, pp. 219–223.

[192] S. Jaeckel, L. Raschkowski, K. Borner, and L. Thiele, "QuaDRiGa: A 3-D Multi-Cell Channel Model With Time Evolution for Enabling Virtual Field Trials," *IEEE Transactions on Antennas and Propagation*, vol. 62, no. 6, pp. 3242–3256, June 2014.

[193] ETSI. (2015, December) Millimetre Wave Transmission (mwt): Analysis Of Antennas For Millimetre Wave Transmission. European Telecommunications Standards Institute. [Online]. Available: http://www.etsi.org/technologies-clusters/technologies/millimetre-wave-transmission

[194] ——. (2015, August) Millimetre Wave Transmission (mwt): Applications And Use Cases Of Millimetre Wave Transmission. European Telecommunications Standards Institute. [Online].

[195] ——. (2016, June) Millimetre Wave Transmission (mwt): V-band Street Level Interference Analysis. European Telecommunications Standards Institute. [Online]. Available: http://www.etsi.org/technologies-clusters/technologies/millimetre-wave-transmission

[196] 3GPP. (2015, June) Study On 3D Channel Model for LTE. [Online]. Available: http://www.3gpp.org/DynaReport/36873.htm

[197] ——. (2017, May) Study on Channel Model for Frequency Spectrum Above 6 GHz. [Online]. Available: http://www.3gpp.org/DynaReport/38900-CRs.htm

[198] W. D. Rummler, "Time- And Frequency-Domain Representation of Multipath Fading on Line-of-sight Microwave Paths," *The Bell System Technical Journal*, vol. 59, no. 5, pp. 763–796, May 1980.

[199] C. Park and T. Rappaport, "Short-Range Wireless Communications for Next-Generation Networks: UWB, 60 GHz Millimeter-Wave WPAN, And ZigBee," *Wireless Communications, IEEE*, vol. 14, no. 4, pp. 70–78, August 2007.

[200] QuaDRiGa. (2014) QuaDRiGa (QUAsi Deterministic RadIo channel GenerAtor). [Online]. Available: http://www.hhi.fraunhofer.de/quadriga

[201] X. Zhao, S. Li, Q. Wang, M. Wang, S. Sun, and W. Hong, "Channel Measurements, Modeling, Simulation and Validation at 32 GHz in Outdoor Microcells for 5G Radio Systems," *IEEE Access*, vol. 5, pp. 1062–1072, 2017.

[202] M. K. Samimi and T. S. Rappaport, "3-D Millimeter-Wave Statistical Channel Model for 5G Wireless System Design," *IEEE Transactions on Microwave Theory and Techniques*, vol. 64, no. 7, pp. 2207–2225, July 2016.

[203] Y. Lostanlen, Y. Corre, Y. Louet, Y. L. Helloco, S. Collonge, and G. El-Zein, "Comparison of measurements and simulations in indoor environments for wireless local networks at 60 GHz," in *IEEE 55th Vehicular Technology Conference (VTC Spring)*, vol. 1, 2002, pp. 389–393 vol.1.

[204] S. Collogne and G. E. Zein, "Characterization and Modelisation of the 60 GHz Electromagnetic Waves Propagation in Indoor Environment," Theses, INSA de Rennes, Dec. 2003. [Online]. Available: https://tel.archives-ouvertes.fr/tel-00009272

[205] S. Piersanti, L. Annoni, and D. Cassioli, "Millimeter Waves Channel Measurements And Path Loss Models," in *IEEE International Conference on Communications (ICC)*, June 2012, pp. 4552–4556.

[206] N. Azzaoui and L. Clavier, "Statistical Channel Model Based on Alpha-Stable Random Processes and Application to The 60 GHz Ultra Wide Band Channel," *IEEE Transactions on Communications*, vol. 58, no. 5, pp. 1457–1467, May 2010.

[207] L. Liu, C. Oestges, J. Poutanen, K. Haneda, P. Vainikainen, F. Quitin, F. Tufvesson, and P. D. Doncker, "The COST 2100 MIMO Channel Model," *IEEE Wireless Communications*, vol. 19, no. 6, pp. 92–99, December 2012.

[208] COST. (2016, April) COST IC1004 White Paper on Channel Measurements and Modeling for 5G Networks in the Frequency Bands above 6 GHz. Cisco. [Online]. Available: http://www.ic1004.org/

[209] NIST. (2015, July) 5G mmWave Channel Model Alliance. NIST. [Online]. Available: www.nist.gov/ctl/wireless-networks-division

[210] A. F. Molisch, H. Asplund, R. Heddergott, M. Steinbauer, and T. Zwick, "The COST259 Directional Channel Model-Part I: Overview and Methodology," *IEEE Transactions on Wireless Communications*, vol. 5, no. 12, pp. 3421–3433, December 2006.

[211] M. K. Samimi and T. S. Rappaport, "3-D Statistical Channel Model For Millimeter-Wave Outdoor Mobile Broadband Communications," in *International Conference on Communications (ICC), IEEE*, June 2015, pp. 2430–2436.

[212] K. Doppler, M. Rinne, C. Wijting, C. B. Ribeiro, and K. Hugl, "Device-to-Device Communication as an Underlay To LTE-Advanced Networks," *IEEE Communications Magazine*, vol. 47, no. 12, pp. 42–49, Dec 2009.

[213] S. Sun, G. R. MacCartney, M. K. Samimi, and T. S. Rappaport, "Synthesizing Omnidirectional Antenna Patterns, Received Power and Path Loss from Directional Antennas for 5G Millimeter-Wave Communications," in *2015 IEEE Global Communications Conference*, Dec 2014, pp. 1–7.

[214] J.-S. Jiang and M. A. Ingram, "Spherical-Wave Model for Short-Range MIMO," *IEEE Transactions on Communications*, vol. 53, no. 9, pp. 1534–1541, Sept 2005.

[215] M. Toeltsch, J. Laurila, K. Kalliola, A. Molisch, P. Vainikainen, and E. Bonek, "Statistical Characterization of Urban Spatial Radio Channels," *IEEE Journal on Selected Areas in Communications*, vol. 20, no. 3, pp. 539–549, Apr 2002.

[216] H. Sawada, H. Nakase, S. Kato, M. Umehira, K. Sato, and H. Harada, "Impulse Response Model and Parameters for Indoor Channel Modeling at 60GHz," in *Vehicular Technology Conference (VTC 2010-Spring), 2010 IEEE 71st*, May 2010, pp. 1–5.

[217] G. R. MacCartney, J. Zhang, S. Nie, and T. S. Rappaport, "Path Loss Models for 5G Millimeter Wave Propagation Channels in Urban Microcells," in *IEEE Global Communications Conference (GLOBECOM)*, Dec 2013, pp. 3948–3953.

[218] T. S. Rappaport, G. R. MacCartney, M. K. Samimi, and S. Sun, "Wideband Millimeter-Wave Propagation Measurements and Channel Models for Future Wireless Communication System Design," *IEEE Transactions on Communications*, vol. 63, no. 9, pp. 3029–3056, Sept 2015.

[219] K. Haneda, J. Zhang, L. Tan, G. Liu, Y. Zheng, H. Asplund, J. Li, Y. Wang, D. Steer, C. Li, T. Balercia, S. Lee, Y. Kim, A. Ghosh, T. Thomas, T. Nakamura, Y. Kakishima, T. Imai, H. Papadopoulos, T. S. Rappaport, G. R. MacCartney, M. K. Samimi, S. Sun, O. Koymen, S. Hur, J. Park, C. Zhang, E. Mellios, A. F. Molisch, S. S. Ghassamzadeh, and A. Ghosh, "5G 3GPP-Like Channel Models for Outdoor Urban Microcellular and Macrocellular Environments," in *IEEE 83rd Vehicular Technology Conference (VTC Spring)*, May 2016, pp. 1–7.

[220] M. Fryziel, C. Loyez, L. Clavier, N. Rolland, and P. A. Rolland, "Path-Loss Model of The 60-GHz Indoor Radio Channel," *Microwave and Optical Technology Letters*, vol. 34, no. 3, pp. 158–162, 2002. [Online]. Available: http://dx.doi.org/10.1002/mop.10402

[221] P. Smulders, "Statistical Characterization of 60-GHz Indoor Radio Channels," *IEEE Transactions on Antennas and Propagation*, vol. 57, no. 10, pp. 2820–2829, Oct 2009.

[222] A. Maltsev, R. Maslennikov, A. Sevastyanov, A. Lomayev, A. Khoryaev, A. Davydov, and V. Ssorin, "Characteristics of Indoor Millimeter-Wave Channel at 60 GHz in Application to Perspective WLAN System," in *Proceedings of the Fourth European Conference on Antennas and Propagation (EuCAP)*, April 2010, pp. 1–5.

[223] A. J. Blanchard and B. R. Jean, "Antenna Effects in Depolarization Measurements," *IEEE Transactions on Geoscience and Remote Sensing*, vol. GE-21, no. 1, pp. 113–117, Jan 1983.

[224] G. R. MacCartney, T. S. Rappaport, S. Sun, and S. Deng, "Indoor Office Wideband Millimeter-Wave Propagation Measurements and Channel Models at 28 and 73 GHz for Ultra-Dense 5G Wireless Networks," *IEEE Access*, vol. 3, pp. 2388–2424, 2015.

[225] W. Hong, K. Baek, Y. Lee, and Y. G. Kim, "Design And Analysis of a Low-Profile 28 GHz Beam Steering Antenna Solution for Future 5G Cellular Applications," in *IEEE MTT-S International Microwave Symposium (IMS)*, June 2014, pp. 1–4.

[226] T. Bai, V. Desai, and R. Heath, "Millimeter Wave Cellular Channel Models for System Evaluation," in *International Conference on Computing, Networking and Communications (ICNC)*, Feb 2014, pp. 178–182.

[227] L. Yang and G. Giannakis, "Ultra-wideband Communications: An Idea Whose Time Has Come," *Signal Processing Magazine, IEEE*, vol. 21, no. 6, pp. 26–54, Nov 2004.

[228] W. Lee, *Integrated Wireless Propagation Models*. McGraw-Hill Education, 2014. [Online]. Available: http://books.google.co.uk/books?id=spGAMAEACAAJ

[229] J. Hoydis, S. ten Brink, and M. Debbah, "Massive MIMO in the UL/DL of Cellular Networks: How Many Antennas Do We Need?" *IEEE Journal on Selected Areas in Communications*, vol. 31, no. 2, pp. 160–171, February 2013.

[230] L. Hanzo, L. Yang, E. Kuan, and K. Yen, *Single and Multi-Carrier DS-CDMA: Multi-User Detection, Space-Time Spreading, Synchronisation, Networkingand Standards*. Wiley, 2003. [Online]. Available: https://books.google.co.uk/books?id=04QSiM_Mzx8C

[231] I. A. Hemadeh, M. El-Hajjar, S. Won, and L. Hanzo, "Layered Multi-Group Steered Space-Time Shift-Keying for Millimeter-Wave Communications," *IEEE Access*, vol. 4, pp. 3708–3718, 2016.

[232] ——, "Multiuser Steered Multiset Space-Time Shift Keying for Millimeter-Wave Communications," *IEEE Transactions on Vehicular Technology*, vol. 66, no. 6, pp. 5491–5495, June 2017.

[233] ——, "Multi-Set Space-Time Shift Keying and Space- Frequency Space-Time Shift Keying for Millimeter-Wave Communications," *IEEE Access*, vol. 5, pp. 8324–8342, 2017.

[234] A. Ghosh, T. Thomas, M. Cudak, R. Ratasuk, P. Moorut, F. Vook, T. Rappaport, G. MacCartney, S. Sun, and S. Nie, "Millimeter-Wave Enhanced Local Area Systems: A High-Data-Rate Approach for Future Wireless Networks," *IEEE Journal on Selected Areas in Communications*, vol. 32, no. 6, pp. 1152–1163, June 2014.

[235] I. A. Hemadeh, P. Botsinis, M. El-Hajjar, S. Won, and L. Hanzo, "Reduced-RF-Chain Aided Soft-Decision Multi-Set Steered Space-Time Shift-Keying for Millimeter-Wave Communications," *IEEE Access*, vol. 5, pp. 7223–7243, 2017.

[236] D. Falconer, S. L. Ariyavisitakul, A. Benyamin-Seeyar, and B. Eidson, "Frequency Domain Equalization For Single-Carrier Broadband Wireless Systems," *IEEE Communications Magazine*, vol. 40, no. 4, pp. 58–66, Apr 2002.

[237] N. Valliappan, A. Lozano, and R. Heath, "Antenna Subset Modulation for Secure Millimeter-Wave Wireless Communication," *IEEE Transactions on Communications*, vol. 61, no. 8, pp. 3231–3245, August 2013.

[238] E. Larsson, O. Edfors, F. Tufvesson, and T. Marzetta, "Massive MIMO for next generation wireless systems," *Communications Magazine, IEEE*, vol. 52, no. 2, pp. 186–195, February 2014.

[239] X. Wu, Z. Ma, and Y. Wang, "Joint User Grouping and Resource Allocation for Multi-User Dual Layer Beamforming in LTE-A," *Communications Letters, IEEE*, vol. PP, no. 99, pp. 1–1, 2015.

[240] Y. Xu, G. Yue, N. Prasad, S. Rangarajan, and S. Mao, "User Grouping and Scheduling for Large Scale MIMO Systems with Two-Stage Precoding," in *International Conference on Communications (ICC), IEEE*, June 2014, pp. 5197–5202.

[241] M. El-Hajjar and L. Hanzo, "Layered Steered Space-Time Codes And Their Capacity," *Electronics Letters*, vol. 43, no. 12, pp. 680–682, June 2007.

[242] L. Hanzo, O. Alamri, M. El-Haijar, and N. Wu, *Advanced Space-Time Coding: Near-Capacity Sphere-Packing, Multi-Functional MIMOs and Cooperative Space-Time Processing*. IEEE Press-John Wiley, 2008. [Online]. Available: http://eprints.soton.ac.uk/265783/

[243] L. L. Hanzo, O. Alamri, M. El-Hajjar, and N. Wu, *Near-Capacity Multi-Functional MIMO Systems: Sphere-Packing, Iterative Detection and Cooperation*, ser. Wiley - IEEE. Wiley, 2009. [Online]. Available: http://books.google.co.uk/books?id=590-JItOJREC

[244] M. El-Hajjar, O. Alamri, J. Wang, S. Zummo, and L. Hanzo, "Layered Steered Space-Time Codes Using Multi-Dimensional Sphere Packing Modulation," *IEEE Transactions on Wireless Communications*, vol. 8, no. 7, pp. 3335–3340, July 2009.

[245] I. A. Hemadeh, M. El-Hajjar, S. Won, and L. Hanzo, "Multi-Set Space-Time Shift-Keying With Reduced Detection Complexity," *IEEE Access*, vol. 4, pp. 4234–4246, 2016.

[246] C. A. Balanis, *Antenna Theory: Analysis and Design*, 3rd ed. Wiley-Interscience, 2005.

[247] P. Ioannides and C. Balanis, "Uniform Circular And Rectangular Arrays for Adaptive Beamforming Applications," *Antennas and Wireless Propagation Letters, IEEE*, vol. 4, pp. 351–354, 2005.

[248] J. R. Costa, E. B. Lima, and C. A. Fernandes, "Compact Beam-Steerable Lens Antenna for 60-GHz Wireless Communications," *IEEE Transactions on Antennas and Propagation*, vol. 57, no. 10, pp. 2926–2933, Oct 2009.

[249] Y. L. Lyu, F. Y. Meng, G. H. Yang, D. Erni, Q. Wu, and K. Wu, "Periodic SIW Leaky-Wave Antenna with Large Circularly-Polarized Beam Scanning Range," *IEEE Antennas and Wireless Propagation Letters*, vol. PP, no. 99, pp. 1–1, 2017.

[250] S. J. Orfanidis. (2016, June) Electromagnetic Waves and Antennas. [Online]. Available: http://www.ece.rutgers.edu/~orfanidi/ewa/#pod

[251] Samsung. (2015, Aug.) 5G Vision. [Online]. Available: http://www.samsung.com/global/business-images/insights/2015/Samsung-5G-Vision-2.pdf

[252] T. M. Cover and J. A. Thomas, *Elements of Information Theory*, 2nd ed. Wiley, 2006.

[253] Agilent Technologies. Fundamentals of RF and Microwave Noise Figure Measurements. [Online]. Available: http://cp.literature.agilent.com/litweb/pdf/5952-8255E.pdf

[254] K.-C. Huang and D. J. Edwards, *Millimeter Wave Antennas*, 1st ed. Wiley, 2008.

Ibrahim A. Hemadeh received a B.Eng. degree (with first class honours) in Computer and Communications Engineering from the Islamic University of Lebanon, Lebanon, in 2010. He then received an M.Sc. degree in Wireless Communications (with distinction) and a Ph.D. degree in Electronics and Electrical Engineering from the University of Southampton, UK, in 2012 and 2017, respectively. He is currently a postdoctocal researcher at Southampton Wireless (SW) group, University of Southampton, UK. His research interests mainly include millimeter-wave communications, multi-functional MIMO, multi-dimensional (time-space-and frequency) transceiver designs, channel coding as well as multi-user MIMO.

Katla Satyanarayana (http://www.satyanarayana. xyz) received his B. Tech. degree in Electrical Engineering from Indian Institute of Technology Madras, India, in 2014. During Jul'14-Aug'15, he worked as a research assistant at Indian Institute of Science, Bangalore. Currently, Satya is a research scholar in Wireless Communications at the University of Southampton in liaison with InterDigital Europe, London, UK. His research interests include millimeter wave communications, hybrid beamforming, with an emphasis on transceiver algorithms for wireless communication systems and multi-functional MIMO.

Mohammed El-Hajjar is an Associate Professor in the department of Electronics and Computer Science in the University of Southampton. He received his PhD in Wireless Communications from the University of Southampton, UK in 2008. Following the PhD, he joined Imagination Technologies as a design engineer, where he worked on designing and developing Imagination's multi-standard communications platform, which resulted in three patents. He is the recipient of several academic awards and has published a Wiley-IEEE book and in excess of 80 journal and conference papers. Mohammed's research interests include the development of intelligent communications systems, energy-efficient transceiver design, MIMO, millimeter-wave communications and Radio over fiber network design.

Lajos Hanzo (http://www-mobile.ecs.soton.ac.uk) FREng, FIEEE, FIET, Fellow of EURASIP, DSc received his degree in electronics in 1976 and his doctorate in 1983. In 2009 he was awarded the honorary doctorate "Doctor Honoris Causa" by the Technical University of Budapest. During his 40-year career in telecommunications he has held various research and academic posts in Hungary, Germany and the UK. Since 1986 he has been with the School of Electronics and Computer Science, University of Southampton, UK, where he holds the chair in telecommunications. He has successfully supervised about 110+ PhD students, co-authored 20 John Wiley/IEEE Press books on mobile radio communications totalling in excess of 10,000 pages, published 1,600+ research entries at IEEE Xplore, acted both as TPC and General Chair of IEEE conferences, presented keynote lectures and has been awarded a number of distinctions. Currently he is directing a 60-strong academic research team, working on a range of research projects in the field of wireless multimedia communications sponsored by industry, the Engineering and Physical Sciences Research Council (EPSRC) UK, the European Research Council's Advanced Fellow Grant and the Royal Society's Wolfson Research Merit Award. He is an enthusiastic supporter of industrial and academic liaison and he offers a range of industrial courses.